

AFIT/DS/ENP/95-02

COLLISIONAL DYNAMICS OF THE RUBIDIUM 5^2P LEVELS

DISSERTATION

Matthew Don Rotondaro
Captain

AFIT/DS/ENP/95-02

19960327 037

Approved for public release; distribution unlimited

AFIT/DS/ENP/95-02

COLLISIONAL DYNAMICS OF THE RUBIDIUM 5^2P LEVELS

DISSERTATION

Presented to the Faculty of the Graduate School of Engineering
of the Air Force Institute of Technology

Air University

In Partial Fulfillment of the
Requirements for the Degree of
Doctor of Philosophy

Matthew Don Rotondaro, B.S., M.S.

Captain

August, 1995

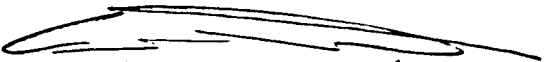
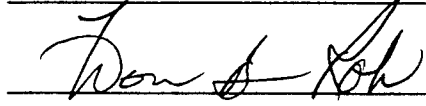
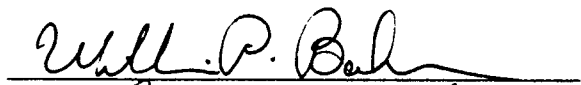
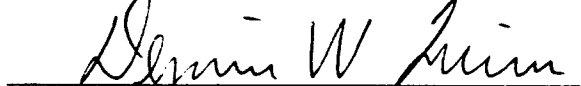

Approved for public release; distribution unlimited

COLLISIONAL DYNAMICS OF THE RUBIDIUM 5^2P LEVELS

Matthew Don Rotondaro, B.S., M.S.

Captain

Approved:

	25 Sep 95
	13 Oct 95
	6 Oct 95
	25 Sep 95
	18 Aug 95



Robert A. Calico, JR.

Dean

Table of Contents

	Page
List of Figures	v
List of Tables	x
Abstract	xii
 I. Introduction	 1
 II. Pressure Broadening and Line Shift in Rubidium	 5
2.1 Pressure broadening and line shift	5
2.2 Previous work which examines the pressure broadening and line shift in rubidium caused by collisions with rare gas atoms and selected molecules	 8
2.3 Absorption spectroscopy	9
2.4 Data analysis	17
2.5 Results of the data reduction	26
2.6 Determination of the interaction potentials	28
2.7 Theoretical determination of the interaction potentials . .	42
2.8 Summary	44
 III. Spin-Orbit and Zeeman Energy Transfer in Rubidium 5^2P Levels . .	 49
3.1 Summary of collisional mixing between the 5^2P fine struc- ture levels induced by rare gas atoms and selected molecules	 49
3.2 Measurement of the fine-structure collisional mixing cross- sections	 50
3.2.1 Collisional mixing process	50
3.2.2 Experimental Procedure	53

	Page
3.2.3 Data analysis	58
3.2.4 Theoretical Discussion of cross-sections	64
3.3 Collisional mixing between the 5^2P Zeeman split levels induced by rare gas atoms and selected molecules	67
3.4 Experimental determination of the Zeeman structure collisional mixing cross-sections	68
3.4.1 Theoretical description of the hyperfine and Zeeman Splitting induced by an applied magnetic field . .	68
3.4.2 Zeeman structure collisional mixing process . . .	79
3.4.3 Experimental procedure	81
3.5 Data analysis	88
3.6 Observations	103
IV. Conclusion	107
Bibliography	110
Vita	117

List of Figures

Figure	Page
1. Hyperfine split ground state of ^{87}Rb utilized by the rubidium atomic clock.	1
2. Rubidium Fine-Structure.	2
3. Illustration of the collisional line shift with the potential curves of the collision pair.	6
4. Line profiles for different wave trains.	7
5. Pressure broadening and line-shift experimental apparatus.	10
6. Absorption spectra of the D_1 line observed at $T=360$ K with the hyperfine splitting and line strengths shown.	13
7. Rubidium 85 and 87 5^2P hyperfine split energy levels.	16
8. Typical absorption spectra near $\lambda = 794.7$ nm at $T=395$ K with argon as the collision partner.	18
9. Typical absorption spectra near $\lambda = 780.0$ nm at $T=395$ K with argon as the collision partner.	19
10. Single peak to illustrate the curve fitting process.	21
11. Curve fit of the D_1 line at 50 Torr of Helium. Displayed with the 95 % confidence limits. The expanded region is provided to illustrate the quality of the curve fits.	24
12. Line shift of the D_1 and D_2 lines in rubidium induced by rare gasses.	27
13. Pressure broadening of the D_1 and D_2 lines in rubidium induced by the rare gasses.	29
14. Line shift of the D_1 and D_2 lines in rubidium induced by H_2 , D_2 and N_2	30
15. Pressure broadening of the D_1 and D_2 lines in rubidium induced by H_2 , D_2 and N_2	31
16. Line shift of the D_1 and D_2 lines in rubidium induced by collisions with CH_4 and CF_4	32

Figure	Page
17. Pressure broadening of the D_1 and D_2 lines in rubidium induced by CH_4 and CF_4	33
18. Solution to the impact approximation to determine the interaction potentials. Also shown are the ratios $\frac{\beta}{\gamma}$, denoted by the horizontal lines, for all of the collision partners.	38
19. Interaction potential differences for the D_1 line. The solid lines depict the unambiguous potentials, the dotted lines depict the ambiguous potentials and the dashed line is for helium using the C_{12} potential.	40
20. Interaction potential differences for the D_2 line. The solid lines depict the unambiguous potentials and the dotted lines depict the ambiguous potentials.	41
21. The interaction probability versus the dipole polarizability for the pressure broadening cross-sections for the D_1 line.	46
22. The interaction probability versus the dipole polarizability for the pressure broadening cross-sections for the D_2 line.	47
23. ^{87}Rb Fine Structure with Mixing and Relaxation Mechanisms.	50
24. Experimental apparatus for measuring the collisional energy transfer cross-sections of the 5P fine structure split levels in ^{87}Rb	54
25. Spin-orbit energy transfer in ^{87}Rb induced by N_2	56
26. Satellite to pump line intensity ratio as a function of rubidium concentration.	57
27. Total fluorescence as a function of laser power.	59
28. Satellite to pump line intensity as a function of laser power.	60
29. Spin-orbit energy transfer pump and satellite lines and the filter leakage and scattered light corrections.	62
30. Satellite to pumped line ratio preparing the $5^2P_{\frac{3}{2}}$ level using N_2 as the collision partner with the filter leakage and scattered light correction.	63
31. ^{87}Rb Zeeman split levels in the high field limit.	69
32. Hyperfine and Zeeman structure energy shifts with respect to zero for the $5^2S_{\frac{1}{2}}$ and the $5^2P_{\frac{1}{2}}$ level.	72

Figure	Page
33. ^{87}Rb hyperfine and Zeeman structure energy shifts with respect to zero for the $5^2P_{\frac{1}{2}}$ level.	73
34. Saturation spectrum of the $5^2P_{\frac{1}{2}}, m_j = \frac{1}{2} \rightarrow 5^2S_{\frac{1}{2}}$ transition at 1 Tesla. The labels represent the Zeeman structure of the ground state. . . .	74
35. A schematic diagram of the saturation spectroscopy experimental apparatus.	75
36. ^{87}Rb hyperfine and Zeeman structure energy shifts with respect to zero for the $5^2P_{\frac{3}{2}}$ level in the low field limit.	77
37. ^{87}Rb hyperfine and Zeeman structure energy shifts with respect to zero for the $5^2P_{\frac{3}{2}}$ level in the high field limit.	78
38. ^{87}Rb Zeeman Structure with Mixing and Relaxation Mechanisms. . .	79
39. Experimental apparatus for measuring the collisional energy transfer cross-sections of the 5P Zeeman split levels in ^{87}Rb	82
40. Intensity ratios versus rubidium concentration using 1 Torr of nitrogen. The circles are for $\frac{I(5^2P_{\frac{3}{2}}, m_j = \frac{1}{2} \rightarrow 5^2S_{\frac{1}{2}}, m_j = \frac{1}{2})}{I(5^2P_{\frac{3}{2}}, m_j = \frac{1}{2} \rightarrow 5^2S_{\frac{1}{2}}, m_j = -\frac{1}{2})}$ and the squares are for $\frac{I(5^2P_{\frac{3}{2}}, m_j = -\frac{1}{2} \rightarrow 5^2S_{\frac{1}{2}}, m_j = -\frac{1}{2})}{I(5^2P_{\frac{3}{2}}, m_j = -\frac{1}{2} \rightarrow 5^2S_{\frac{1}{2}}, m_j = \frac{1}{2})}$	84
41. The figure on the left is for the intensity ratio $\frac{I(5^2P_{\frac{3}{2}}, m_j = \frac{1}{2} \rightarrow 5^2S_{\frac{1}{2}}, m_j = \frac{1}{2})}{I(5^2P_{\frac{3}{2}}, m_j = \frac{1}{2} \rightarrow 5^2S_{\frac{1}{2}}, m_j = -\frac{1}{2})}$ versus laser power, and the figure on the right is the fluorescence intensity of the prepared state versus laser power.	85
42. Typical scatter corrected data for the $(5^2S_{\frac{1}{2}}, m_j = -\frac{1}{2}) \rightarrow (5^2P_{\frac{1}{2}}, m_j = -\frac{1}{2})$ pumped transition at 1.2 Torr of nitrogen scanning the $5^2P_{\frac{1}{2}}$ manifold with the resulting curve fit shown.	86
43. Typical scatter corrected data for the $(5^2S_{\frac{1}{2}}, m_j = -\frac{1}{2}) \rightarrow (5^2P_{\frac{3}{2}}, m_j = -\frac{1}{2})$ pumped transition at 1.2 Torr of nitrogen scanning the $5^2P_{\frac{3}{2}}$ manifold with the resulting curve fit shown.	86
44. Typical scatter corrected data for the $(5^2S_{\frac{1}{2}}, m_j = -\frac{1}{2}) \rightarrow (5^2P_{\frac{3}{2}}, m_j = -\frac{1}{2})$ pumped transition at 1.2 Torr of nitrogen scanning the $5^2P_{\frac{3}{2}}$ manifold with the resulting curve fit shown.	87

45. Typical scatter corrected data for the $(5^2S_{\frac{1}{2}}, m_j = -\frac{1}{2}) \rightarrow (5^2P_{\frac{3}{2}}, m_j = -\frac{1}{2})$ pumped transition at 1.2 Torr of nitrogen scanning the $5^2P_{\frac{1}{2}}$ manifold with the resulting curve fit shown. 87
46. Typical scatter corrected data for the $(5^2S_{\frac{1}{2}}, m_j = -\frac{1}{2}) \rightarrow (5^2P_{\frac{3}{2}}, m_j = -\frac{3}{2})$ pumped transition at 1.0 Torr of nitrogen scanning the $5^2P_{\frac{3}{2}}$ manifold with the resulting curve fit shown. This figure also shows the data before the scatter is removed. 88
47. Zeeman energy transfer to the satellite levels with the $5^2P_{\frac{1}{2}}, m_j = -\frac{1}{2}$ level prepared by pumping the $5^2S_{\frac{1}{2}}, m_j = -\frac{1}{2} \rightarrow 5^2P_{\frac{1}{2}}, m_j = -\frac{1}{2}$ transition. $\diamond \frac{N_S(5^2P_{\frac{1}{2}}, m_j = +\frac{1}{2})}{N_P}$, $\square \frac{N_S(5^2P_{\frac{3}{2}}, m_j = -\frac{1}{2})}{N_P}$, $\nabla \frac{N_S(5^2P_{\frac{3}{2}}, m_j = -\frac{3}{2})}{N_P}$, $\circ \frac{N_S(5^2P_{\frac{3}{2}}, m_j = +\frac{3}{2})}{N_P}$, and $\triangle \frac{N_S(5^2P_{\frac{3}{2}}, m_j = +\frac{1}{2})}{N_P}$ 91
48. Zeeman energy transfer to the satellite levels with the $5^2P_{\frac{3}{2}}, m_j = \frac{3}{2}$ level prepared by pumping the $5^2S_{\frac{1}{2}}, m_j = \frac{1}{2} \rightarrow 5^2P_{\frac{3}{2}}, m_j = \frac{3}{2}$ transition. $\circ \frac{N_S(5^2P_{\frac{3}{2}}, m_j = -\frac{1}{2})}{N_P}$, $\square \frac{N_S(5^2P_{\frac{3}{2}}, m_j = +\frac{1}{2})}{N_P}$, and $\triangle \frac{N_S(5^2P_{\frac{3}{2}}, m_j = -\frac{3}{2})}{N_P}$. 92
49. Zeeman energy transfer to the satellite levels with the $5^2P_{\frac{3}{2}}, m_j = -\frac{1}{2}$ level prepared by pumping the $5^2S_{\frac{1}{2}}, m_j = -\frac{1}{2} \rightarrow 5^2P_{\frac{3}{2}}, m_j = -\frac{1}{2}$ transition. $\nabla \frac{N_S(5^2P_{\frac{3}{2}}, m_j = -\frac{3}{2})}{N_P}$, $\square \frac{N_S(5^2P_{\frac{3}{2}}, m_j = +\frac{3}{2})}{N_P}$, $\triangle \frac{N_S(5^2P_{\frac{3}{2}}, m_j = +\frac{1}{2})}{N_P}$, $\circ \frac{N_S(5^2P_{\frac{1}{2}}, m_j = -\frac{1}{2})}{N_P}$, and $\diamond \frac{N_S(5^2P_{\frac{1}{2}}, m_j = +\frac{1}{2})}{N_P}$ 93
50. Zeeman energy transfer to the satellite levels with the $5^2P_{\frac{3}{2}}, m_j = \frac{1}{2}$ level prepared by pumping the $5^2S_{\frac{1}{2}}, m_j = \frac{1}{2} \rightarrow 5^2P_{\frac{3}{2}}, m_j = \frac{1}{2}$ transition. $\square \frac{N_S(5^2P_{\frac{3}{2}}, m_j = +\frac{3}{2})}{N_P}$, $\nabla \frac{N_S(5^2P_{\frac{3}{2}}, m_j = -\frac{3}{2})}{N_P}$, $\triangle \frac{N_S(5^2P_{\frac{3}{2}}, m_j = -\frac{1}{2})}{N_P}$, $\diamond \frac{N_S(5^2P_{\frac{1}{2}}, m_j = +\frac{1}{2})}{N_P}$ and $\circ \frac{N_S(5^2P_{\frac{1}{2}}, m_j = -\frac{1}{2})}{N_P}$ 94
51. Zeeman energy transfer to the satellite levels with the $5^2P_{\frac{3}{2}}, m_j = -\frac{3}{2}$ level prepared by pumping the $5^2S_{\frac{1}{2}}, m_j = -\frac{1}{2} \rightarrow 5^2P_{\frac{3}{2}}, m_j = -\frac{3}{2}$ transition. $\circ \frac{N_S(5^2P_{\frac{3}{2}}, m_j = -\frac{1}{2})}{N_P}$, $\square \frac{N_S(5^2P_{\frac{3}{2}}, m_j = +\frac{1}{2})}{N_P}$, and $\triangle \frac{N_S(5^2P_{\frac{3}{2}}, m_j = +\frac{3}{2})}{N_P}$. 95
52. Zeeman energy transfer to the satellite levels with the $5^2P_{\frac{1}{2}}, m_j = \frac{1}{2}$ level prepared by pumping the $5^2S_{\frac{1}{2}}, m_j = \frac{1}{2} \rightarrow 5^2P_{\frac{1}{2}}, m_j = \frac{1}{2}$ transition. $\circ \frac{N_S(5^2P_{\frac{1}{2}}, m_j = -\frac{1}{2})}{N_P}$, $\nabla \frac{N_S(5^2P_{\frac{3}{2}}, m_j = +\frac{1}{2})}{N_P}$, $\square \frac{N_S(5^2P_{\frac{3}{2}}, m_j = +\frac{3}{2})}{N_P}$, $\diamond \frac{N_S(5^2P_{\frac{3}{2}}, m_j = -\frac{3}{2})}{N_P}$ and $\triangle \frac{N_S(5^2P_{\frac{3}{2}}, m_j = -\frac{1}{2})}{N_P}$ 96

Figure	Page
53. Reduced set of energy transfer cross-sections.	100
54. A comparison of the Zeeman cross-sections versus magnetic field with ∇ helium, \bigcirc neon, \square argon, \triangle krypton, — $\sigma(J = \frac{1}{2}, m_j = \frac{1}{2} \leftrightarrow$ $J = \frac{1}{2}, m_j = -\frac{1}{2})$, — — — $\sigma(J = \frac{3}{2}, m_j = \frac{1}{2} \leftrightarrow J = \frac{3}{2}, m_j = -\frac{1}{2})$, $\cdots \cdots \sigma(J = \frac{3}{2}, m_j = \frac{1}{2} \leftrightarrow J = \frac{3}{2}, m_j = \frac{3}{2})$, — — — $\sigma(J = \frac{3}{2}, m_j = \frac{1}{2} \leftrightarrow J =$ $\frac{3}{2}, m_j = -\frac{3}{2})$	105

List of Tables

Table	Page
1. Theoretical line strengths.	12
2. A and B coefficients and relative line positions, rp_i	15
3. $\Delta\lambda$ for the ^{87}Rb ($5^2S_{1/2}, F=2$ to $5^2P_{1/2}, F=2$) - ^{85}Rb ($5^2S_{1/2}, F=3$ to $5^2P_{1/2}, F=2$) for the D_2 line and ^{87}Rb ($5^2S_{1/2}, F=2$ to $5^2P_{3/2}, F=3$) - ^{85}Rb ($5^2S_{1/2}, F=3$ to $5^2P_{3/2}, F=2$) for the D_2 line.	26
4. Shifts and broadening of the D_1 resonance line of rubidium accompanying collisions with inert-gas atoms and selected molecules.	34
5. Shifts of the D_2 resonance line of rubidium accompanying collisions with inert-gas atoms and selected molecules. [†] Calculated taking account of the anisotropy of the interaction. ^{††} Calculated without taking account of the anisotropy of the interaction.	35
6. The intercepts for the linear curve fits of the pressure broadening and line shift data.	36
7. Polarizability of the collision partners.	43
8. C_6 and C_{12} constants for the 6,12 potential.	43
9. Radius of the pressure broadening collision partners.	48
10. Definition of terms for the fine structure collisional mixing.	52
11. Excitation transfer cross-sections for Rb induced by molecular collisions. ¹ These values were obtained from a plot of cross-section vs temperature.	65
12. Excitation transfer cross-sections for Rb induced by collisions with rare gas atoms and alkali metals. ¹ Theoretical values.	66
13. Term definitions for the Zeeman energy shifts.	70
14. The isotope shift between ^{87}Rb and ^{85}Rb	71
15. Rubidium constants ¹ Theoretical value.	76
16. Definition of terms for the Zeeman split collisional mixing.	80
17. Coefficients for the Zeeman energy transfer curve fitting.	89

Table	Page
18. Zeeman split lines theoretical line strengths.	90
19. Excitation transfer cross-sections for the 5^2P Zeeman split levels in Rb induced by collisions with nitrogen.	97
20. Comparison of the Zeeman energy transfer cross-sections for nitrogen using detail-balance.	98
21. Comparison of the Zeeman energy transfer cross-sections for nitrogen using the relation $\sigma(J, m \rightarrow J, m') = \sigma(J, -m \rightarrow J, -m')$	99
22. Comparison of the Zeeman energy transfer cross-sections for nitrogen using the relation $\sigma(J, m \rightarrow J', m) = \sigma(J, -m \rightarrow J', -m)$	99
23. Resulting cross-sections after applying the relations.	99
24. Reduced set of cross-sections for each gas.	100
25. Excitation transfer cross-sections for the 5^2P Zeeman split levels in Rb induced by collisions with neutral gases.	101
26. Excitation transfer cross-sections for the 6^2P Zeeman split levels in Rb induced by collisions with rare gas atoms.	102
27. A comparison of the Zeeman energy transfer cross-sections by direct and indirect measurement. The cross-sections are reported using the notation $\sigma(J, m_j \leftrightarrow J', m_{j'})$ for the 5^2P levels in rubidium.	104
28. Theoretical scaling ratios compared with experimental values for nitrogen gas.	106
29. Comparison of the cross-sections obtained from the pressure broadening, spin-orbit and Zeeman energy transfer experiments.	108

Abstract

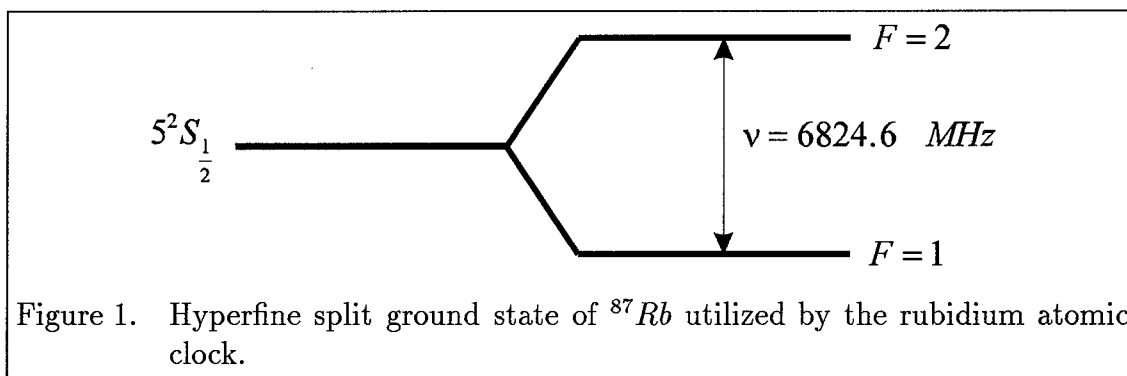
The collisional dynamics of the 5^2P levels in rubidium have been examined using steady-state laser absorption and spectrally-resolved laser induced fluorescence techniques. State-to-state cross-sections for energy transfer between Zeeman split levels ranged from 16-248 \AA^2 for collisions with nitrogen and rare gases. These energy transfer cross-sections exhibit a significant dependence on (J, m_j) state and certain symmetry relationships are demonstrated. A sub-Doppler spectrum of the Zeeman split levels indicating the isotopic shift in the D_1 line of 106 ± 35 was obtained using laser saturation spectroscopy. Cross-sections for spin orbit energy transfer between the $5^2P_{\frac{1}{2}}$ and $5^2P_{\frac{3}{2}}$ levels for collisions with H_2 ($\sigma_{P_{\frac{1}{2}} \rightarrow P_{\frac{3}{2}}} = 10.0 \text{ \AA}^2, \sigma_{P_{\frac{3}{2}} \rightarrow P_{\frac{1}{2}}} = 13.9 \text{ \AA}^2$), D_2 (21.4, 29.8), N_2 (13.2, 18.4), CH_4 (29.5, 41.0) and CF_4 (9.5, 13.2) have been measured. Finally, the pressure broadening and pressure induced line shifts for Rb $5^2P_{\frac{1}{2}} - 5^2S_{\frac{1}{2}}$ and $5^2P_{\frac{3}{2}} - 5^2S_{\frac{1}{2}}$ transitions at low buffer gas pressure were obtained from high resolution laser absorption spectra. The shifts β and broadening γ for H_2 , D_2 , N_2 , CH_4 and CF_4 are in MHz per Torr $\beta(5^2P_{\frac{1}{2}}) = -2.17, -2.22, -7.41, -7.92, -5.41$; $\beta(5^2P_{\frac{3}{2}}) = -3.83, -4.09, -5.79, -7.0, -5.73$; $\gamma(5^2P_{\frac{1}{2}}) = 17.3, 14.1, 16.3, 29.1, 18.7$; $\gamma(5^2P_{\frac{3}{2}}) = 26.4, 20.6, 18.3, 26.2, 17.3$ respectively. These values have been further interpreted using the impact approximation for collisional broadening to obtain the parameters for the Leonard Jones interaction potentials. The rates for pressure broadening are clearly correlated with polarizability of the collision partner.

COLLISIONAL DYNAMICS OF THE RUBIDIUM 5^2P LEVELS

I. Introduction

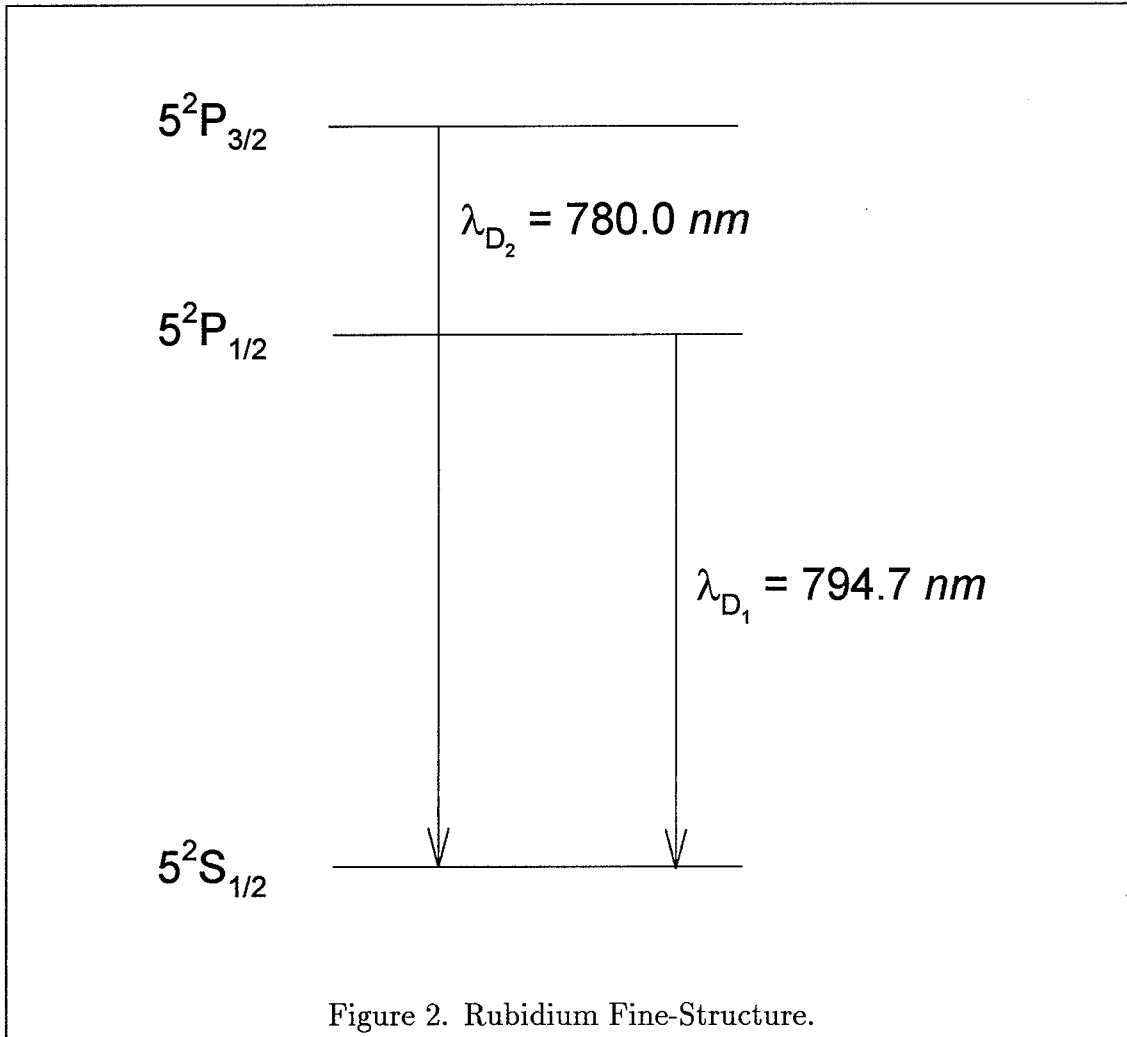
The Air Force has an existing need for very stable clocks for use in global positioning satellites. The two clocks that are used are the rubidium and cesium atomic clocks. The long term frequency stability of the cesium clock is $\approx 10^{-12}$ and the frequency stability for the rubidium clock is $\approx 10^{-11}$. The short term frequency stability (less than 1 s) for the cesium clock is $\approx 10^{-13}$ and the rubidium clock is $\approx 10^{-12}$ (81). Both clocks provide very good short term frequency stability and both are used in global positioning satellites.

The rubidium clock depends on an atomic resonance between the hyperfine split 5^2S levels in ^{87}Rb as shown in Figure 1. The clock is composed essentially of



an optical package acting as a frequency reference, and of a frequency-locked loop for locking the frequency of a crystal oscillator to the optical package reference. The optical package consists of a ^{87}Rb lamp, a ^{85}Rb hyperfine filter, a ^{87}Rb absorption cell, a microwave cavity and a photodetector. Light from the ^{87}Rb lamp, filtered by the ^{85}Rb filter, falls on the absorption cell containing ^{87}Rb and a buffer gas. The

spectrum of the light emitted by the lamp consists mostly of the D_1 and D_2 lines characteristic of alkali-metal atoms as shown in Figure 2.



Each of the lines consists of several components created by the hyperfine structure of either the ground state or the excited state. The hyperfine splitting of the ground state is 6.8 GHz. The emitted light is allowed to pass through the filter cell containing ^{85}Rb and a buffer gas. The spectrum of the ^{85}Rb atom is very similar to that of ^{87}Rb except for the hyperfine splitting of the ground state which is 3.0 GHz. One of the ^{85}Rb lines is almost coincident with one of the ^{87}Rb lines for both the D_1 and D_2 lines. This property is exploited for filtering the ^{87}Rb spectrum. The filter

selectively absorbs lines which transition to the $5^2S_{\frac{1}{2}}, F = 2$ ground state hyperfine split level. When the resulting light is allowed to fall on the absorption cell containing ^{87}Rb , only atoms in the $5^2S_{\frac{1}{2}}, F = 1$ are resonant with the light. These atoms are excited to the P states. The effect is to increase the population of the $F=2$ level at the expense of the $F=1$ level and a population inversion results. By means of this optical pumping the cell becomes transparent to the incident light. However, if transitions are excited between $5^2S_{\frac{1}{2}}$ $F=2$ and $F=1$ levels the absorption cell becomes more opaque and this effect is detected at the photodetector. A minimum of the light intensity is observed at the detector when the microwave radiation frequency is coincident with the resonant frequency of the ground state of ^{87}Rb .

The ^{87}Rb absorption cell is a low pressure cell containing a buffer gas. In an optically pumped passive rubidium frequency standard, the buffer gas is used to prevent wall relaxation but, the hyperfine splitting is affected by the pressure of the buffer gas in the rubidium cell (80). Therefore, the long term stability of this transition and therefore the performance of the rubidium clock is believed to be affected by changes in buffer gas concentration in the cell and it appears as though the cell walls release gases during the clocks operational lifetime producing a frequency shift caused by changes in pressure and gas concentration. Therefore, an accurate characterization of rubidium in a similar environment is needed to accurately predict the clock's performance degradation and to suggest ways of improving the rubidium clock's long term performance. Additionally, the signal on the photodetector is directly affected by the relative populations of the $F=1$ and $F=2$ levels. When collisional energy transfer occurs the populations in these levels are affected resulting in a degradation of the clock's performance.

While a great deal of study of the kinetics of rubidium for atomic clocks has been accomplished over the past few decades (81), there are still several unanswered questions. This research has answered some of these questions by measuring the collisional cross-sections for energy transfer of the spin-orbit and Zeeman split 5^2P

levels of rubidium with selected gases and also by measuring the collision induced line shift and pressure broadening of these levels. The examination of the collisional dynamics of the 5^2P levels improves the understanding of the interaction potentials between these gases and rubidium. The pressure broadening and pressure line shift work has resulted in a determination of the interaction potentials of rubidium with the selected gases. Also the pressure broadening data has revealed a dependence between the size of the pressure broadening cross-sections and the polarizability of the perturbing gas. Also a theory predicting the scaling of the Zeeman energy transfer cross-sections has been compared to the Zeeman energy transfer cross-sections using nitrogen gas. The favorable comparison indicates that a Van der Waals potential is a reasonable model for the interaction. This is in agreement with the correlation of the pressure broadening data with the polarizability of the perturbing gas.

II. Pressure Broadening and Line Shift in Rubidium

2.1 Pressure broadening and line shift

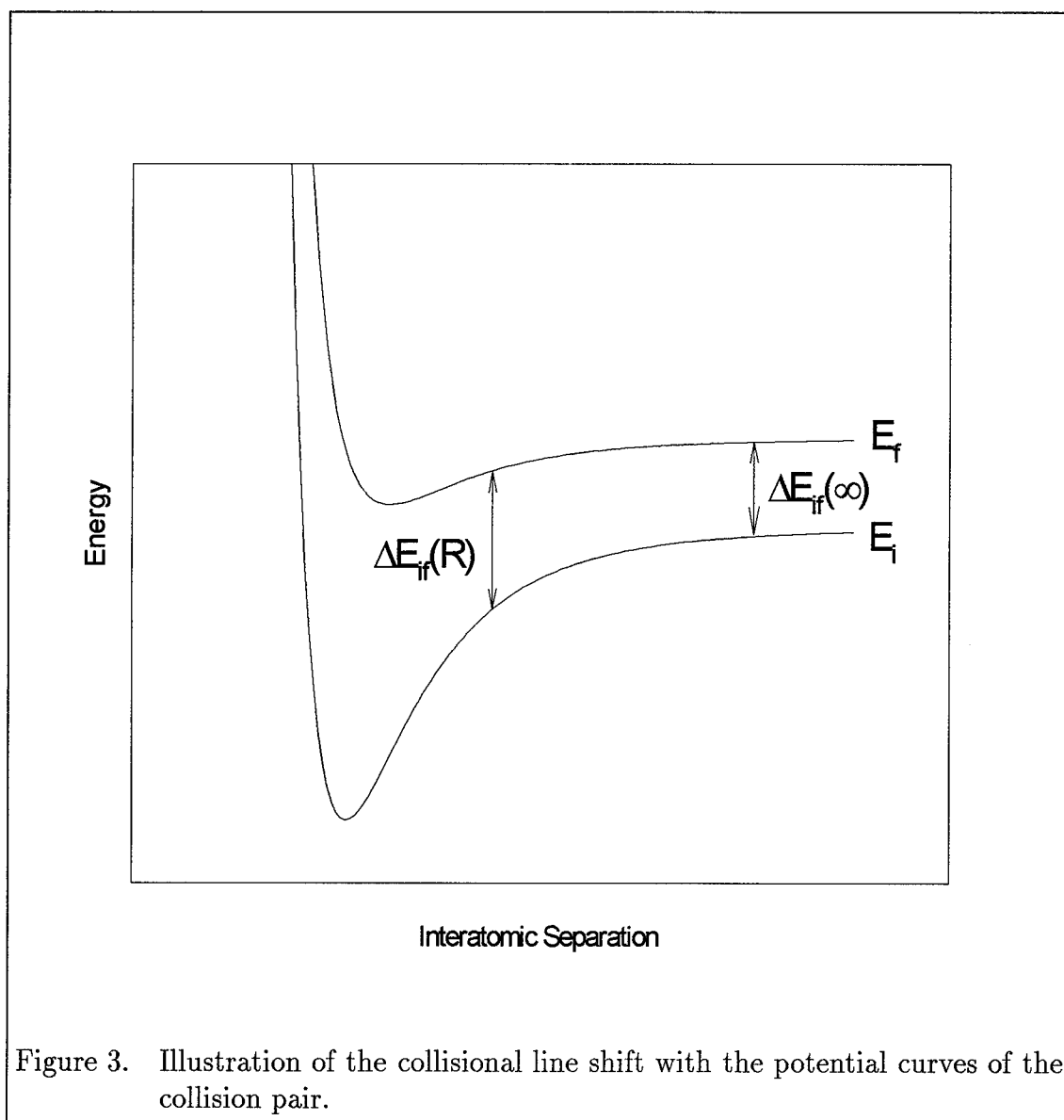
Atomic spectral lines are rarely sharp, symmetric, or centered on the exact energy level difference for the isolated atomic states. The causes for the distribution of radiation in an atomic transition have been a subject of study at least since the turn of the century. Through analysis of spectra from various observations the effects of the resonant interaction of one atom with another dissimilar atom or molecule have been studied.

When an atom X, with energy levels E_i and E_f , approaches another atom or molecule Y, the energy levels of X are shifted because of the interaction between X and Y. This shift depends on the electron configurations of X and Y and on the distance R between the collision partners.

The energy shifts ΔE are in general different for the levels E_i and E_f and they may be positive as well as negative. ΔE is positive if the interaction between X and Y is repulsive and negative if it is attractive. When plotting the energy potentials $E(R)$ for the different energy levels as a function of the interatomic distance R the potential curves of Figure 3 are obtained. Figure 3 graphically represents the interaction potentials and the energy shift (line shift) associated with the interaction.

The monochromatic emission from a two level system would produce a wave train of infinite extent yielding the spectrum 1 in Figure 4. In an environment where collisions can occur, by modeling the atoms as hard spheres and assuming the collisions only occurred when the distance between atoms is less than or equal to the sum of their mean atomic radii, a wave train of finite extent is produced which yields the $\text{sinc}^2(\nu)$ frequency distribution 2 in Figure 4. In a more general case collisions not only affect the length of the wave train but also change the phase of the oscillator which yields the Lorentzian frequency profile 3 in Figure 4. By examining

the spectrum from these transitions and measuring the full width at half maximum and the frequency shift it is possible to characterise the interaction potentials.



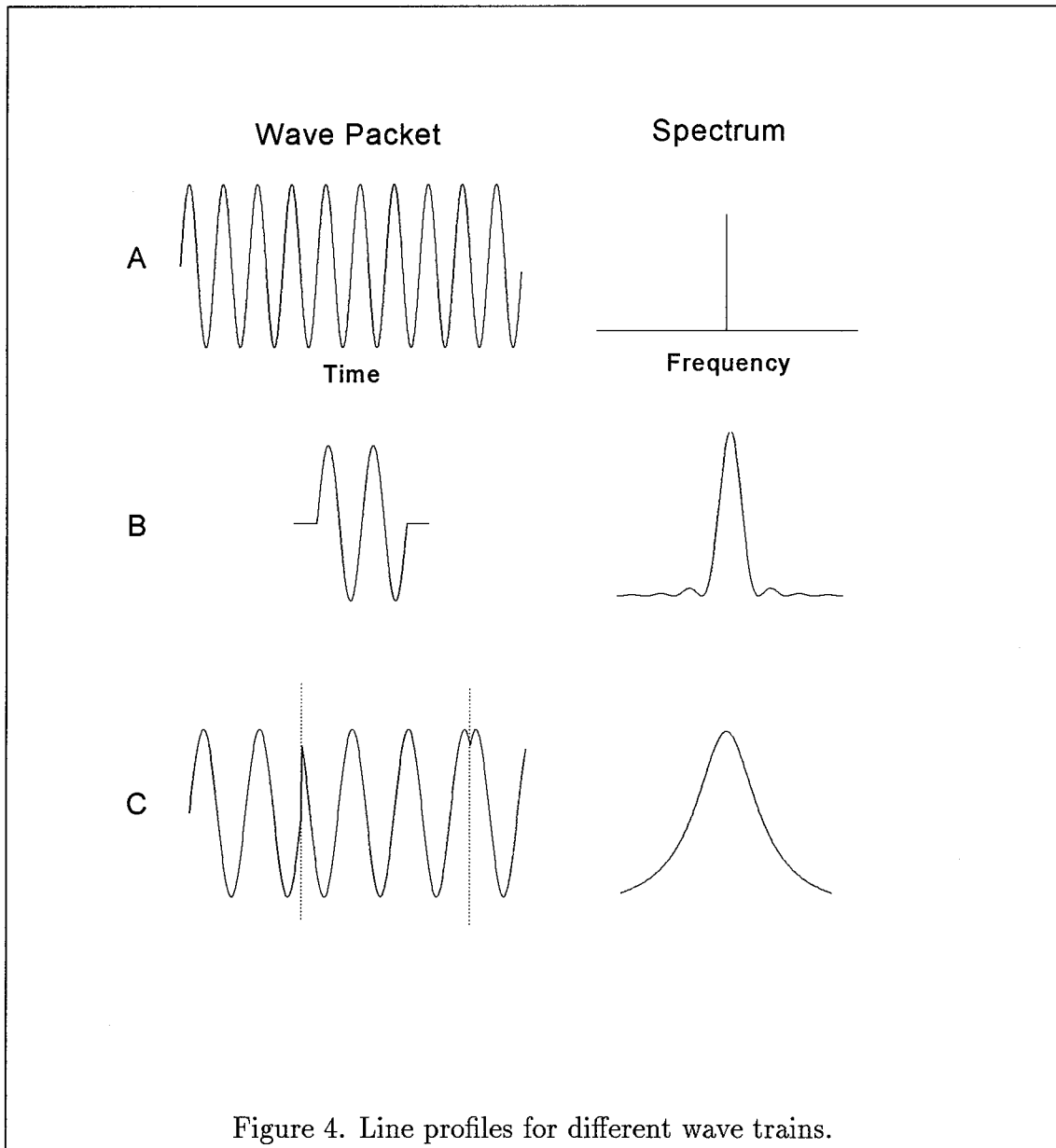


Figure 4. Line profiles for different wave trains.

2.2 Previous work which examines the pressure broadening and line shift in rubidium caused by collisions with rare gas atoms and selected molecules

A comprehensive review of neutral nonresonant collisions of atomic spectral lines has been performed by Allard and Kielkopf (2). The most recent measurement of the broadening and shift of the D_2 (780.0 nm) line of rubidium was performed by Belov (14) and the broadening and shift for the D_1 (794.7 nm) were most recently measured by Kazantsev (44). These measurements used a magnetic scanning technique which represents the highest resolution measurements to date.

The previous measurements of line shift and pressure broadening by Ottinger (62) used dispersive spectroscopy to observe the rubidium spectrum. Because of the resolution limits imposed by these devices it was necessary to conduct the measurements at relatively high pressures (tens of atmospheres). Measurements at these pressures and with such limited resolution make it impossible to observe the hyperfine components of the lines directly. This requires a deconvolution of the hyperfine components and the line function of the dispersive element to determine the broadening coefficient. There are inherent ambiguities whenever such a deconvolution is performed which impose a certain amount of uncertainty in the measured values. The technique employed to measure the broadening and shift in this research used a scanning titanium sapphire ring laser in an absorption spectroscopy experiment which was able to resolve the hyperfine split components. This allowed measurements to be performed at much lower pressures (less than one atmosphere) and didn't suffer from the degradation of the signal due to the convolution of the hyperfine lines and the line function of the dispersive element.

A great deal of theoretical work on pressure broadening and line shift has been accomplished (2). Theories include classical, semiclassical and quantum mechanical treatments. While it was not the intent of this research to improve the existing theories, a comparison of the theoretical and experimental values was made.

2.3 Absorption spectroscopy

Absorption spectroscopy is used in the present experiment to measure the pressure broadening and line shift. The absorption cross-section as a function of wavelength $\sigma(\lambda)$ is determined by using a modified form of Beer's law which is given by equation 1. The A represents the relative detectivities imposed by the detection system between $I_0(\lambda)$ and $I(\lambda)$, l is the path length through the cell and N_{Rb} is the concentration of rubidium.

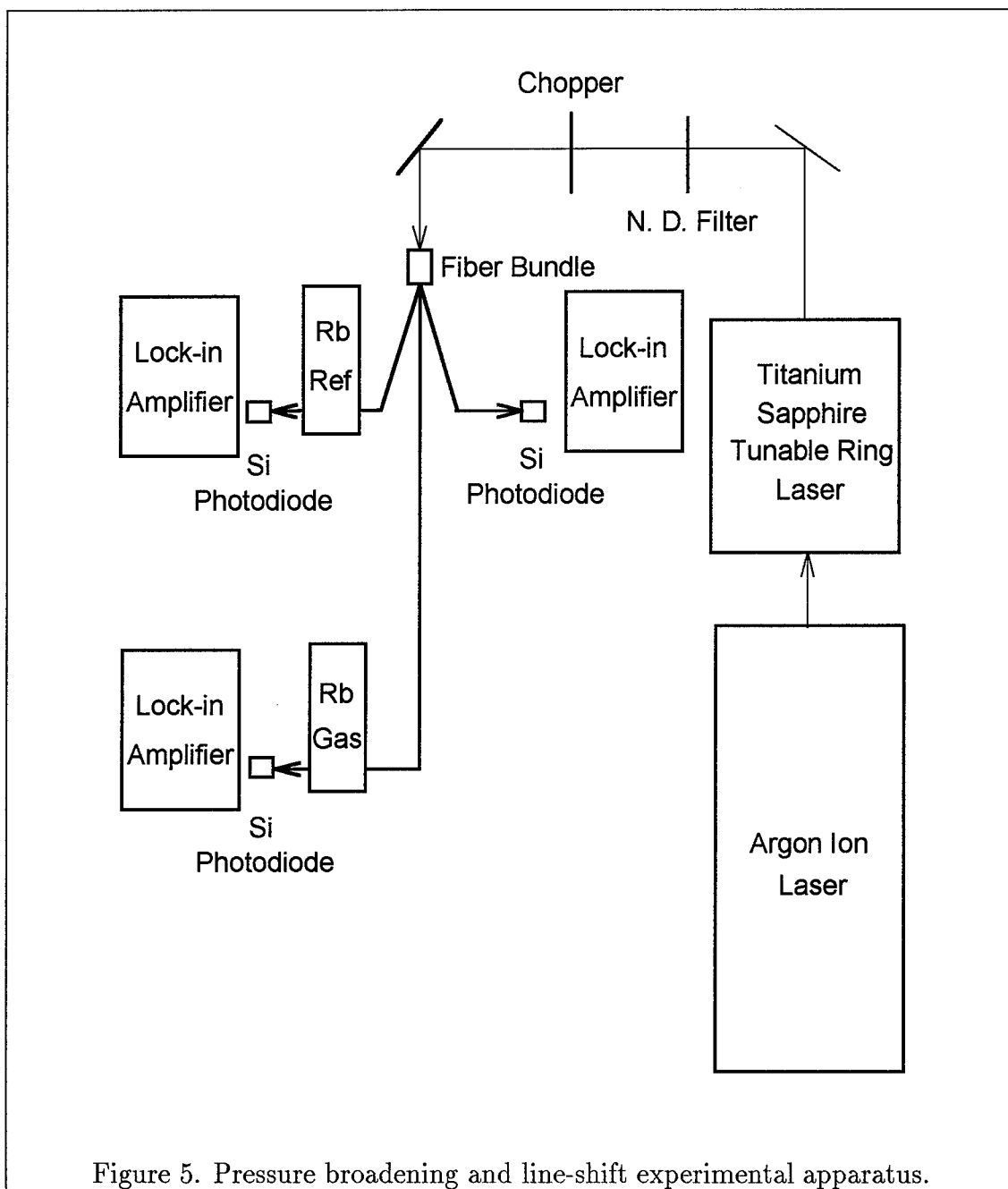
$$I(\lambda) = AI_0(\lambda) \exp^{-l\sigma(\lambda)N_{Rb}} \quad (1)$$

Rearranging this equation yields

$$\ln \left(\frac{I(\lambda)}{I_0(\lambda)} \right) = \alpha - \sigma(\lambda)lN_{Rb}. \quad (2)$$

This allows an experimental characterization of the absorption cross-section $\sigma(\lambda)$ as a function of wavelength where $\alpha = \ln(A)$ represents a non zero base line.

A schematic diagram of the experimental apparatus used is provided in Figure 5. The apparatus consisted of a 15 watt Spectra-Physics argon ion laser used to pump a Coherent 899 tunable titanium sapphire ring laser. The ring laser is capable of producing a single mode which is frequency tunable over the range 720 to 825 nm at up to 1.5 watts continuous wave operation. The ring laser's line width is of the order of $\approx 500kHz$ which is much less than the $600MHz$ Doppler line width of the rubidium. Therefore, Doppler-limited spectroscopy could be performed. The ring laser's beam was coupled into a fiber bundle which served three purposes. The first was to simplify moving the beam to and from the cells. The second was to split the beam into the three components. The last was to randomize the polarization of the laser. This was accomplished by using a scattering center to scatter the light as it was coupled into the fiber bundle. To effectively probe all transitions, both linear and circular polarizations were required. Therefore, a randomization of the laser



light was necessary to probe all of the transitions equally. A thorough randomization is demonstrated by the quality of the curve-fits outlined later in this chapter. The light, using the fiber bundles, was routed to a detector to allow the characterization of the laser's power and through two gas cells as shown in Figure 5. One cell contained only rubidium vapor and was used as an absolute frequency reference. The other cell contained rubidium and the selected gas. The vacuum system could bring the pressure in the cells down to ≈ 1 mTorr. The cells consisted of rectangular glass fluorocells with a 1 cm and a 2 cm path length. These cells were blown onto a glass valve as was the rubidium break-seal ampul. The rubidium was 99.8 % pure with naturally occurring isotopic concentrations. Phase sensitive detection was employed to detect the laser intensities. The detectors used were Hamamatsu photodiodes. The lock-in amplifiers were Stanford Research Systems models SR830 and SR850. The use of phase sensitive detection greatly simplified the experiment by rejecting background noise such as room lights.

The absorption measurements were performed by scanning the laser frequency. The laser's continuous scanning range is 10 GHz which was large enough to probe the full hyperfine structure for pressures up to 50 Torr. Above this pressure three successive 10 GHz scans were required. A comparison of the absorption spectra for several pressures was performed to measure the pressure broadening and line shift. The reproducibility of the initial scan position of the laser was very important. The laser had an initial position reproducibility of ± 25 MHz. This produced a significant error in the characterization of the line shifts. This error was minimized by using the reference cell as an absolute frequency reference.

An additional concern was the temperature control of the cell. The cell was held at a constant temperature throughout the data collection. This was necessary to eliminate the possibility of influencing the measured pressure broadening by changing the Doppler width of the rubidium. Unfortunately, this constant temperature requirement created its own problem. The rubidium concentration dropped as

the buffer gas pressure in the cell was increased. The balance between the diffusion transport and the wall accommodation of the rubidium established the rubidium concentration. Since the absolute rubidium concentration affects the transmitted intensity, a long path length (2 cm) was used for the high pressure measurements (greater than 50 Torr) and a short path length cell (1 cm) was used for all other pressures.

Figure 6 shows a typical absorption spectrum of the D_1 line taken from a reference cell. Note that lines from both rubidium isotopes ^{85}Rb and ^{87}Rb are evident. The figure also displays the transitions associated with the hyperfine splitting of the $5^2S_{1/2}$ level for both isotopes as well as the hyperfine splitting of the $5^2P_{1/2}$ level in ^{87}Rb . Also shown in the figure is the rubidium isotopic abundance weighted theoretical line strengths and the position of each of the allowed transitions. The line strengths are also given in Table 1 which are from reference (48). The line strengths must be corrected to account for the isotopic abundance of ^{85}Rb 72.15% and ^{87}Rb 27.85%. The correction can be made by multiplying the ^{85}Rb line strengths by 2.591.

Table 1. Theoretical line strengths.

Ref(48)	^{87}Rb			^{85}Rb		
	F	1	2	F	2	3
$P_{1/2}$	1	20.0	100	2	28.6	100
	2	100	100	3	100	80.0
$P_{3/2}$	0	14.3	-	1	33.3	-
	1	35.7	7.1	2	43.2	12.3
	2	35.7	35.7	3	34.6	43.2
	3	-	100	4	-	100

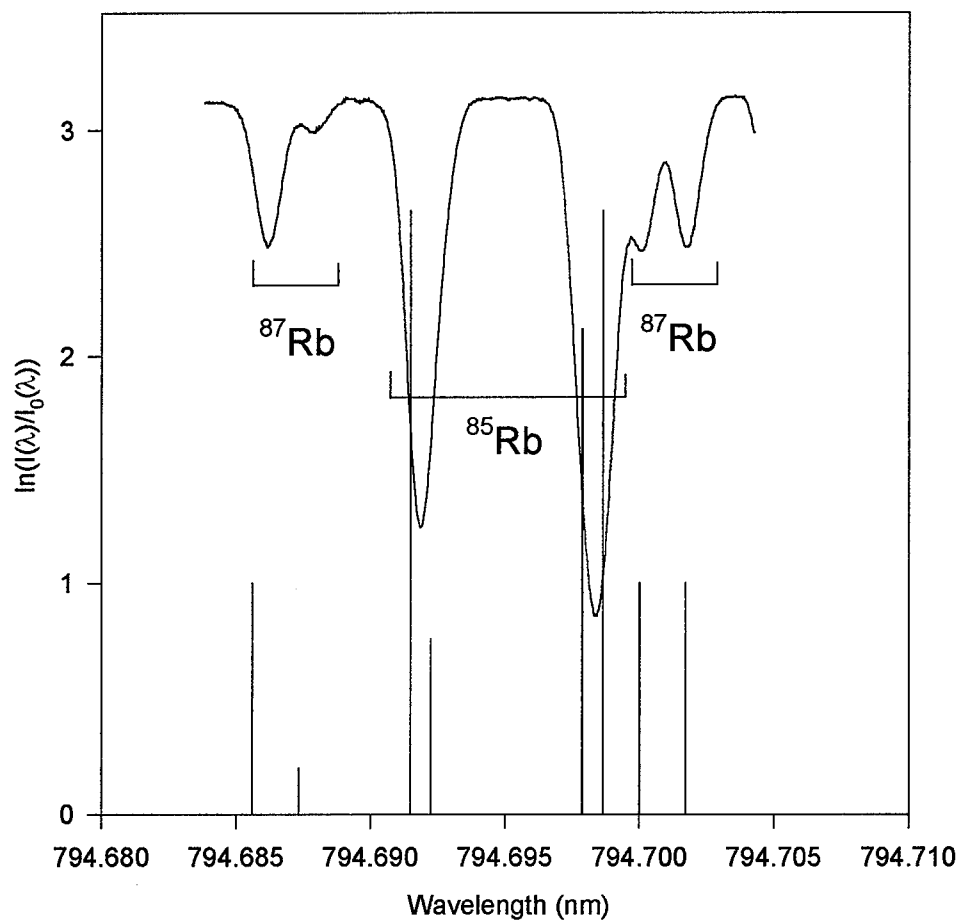


Figure 6. Absorption spectra of the D_1 line observed at $T=360$ K with the hyperfine splitting and line strengths shown.

The total energy of a hyperfine split level with the total angular momentum F is given by equation 3 from reference (48):

$$E_F = E_J + A \frac{C}{2} + B \frac{\frac{3}{4}C(C+1) - I(I+1)J(J+1)}{2I(2I-1)J(2J-1)} \quad (3)$$

where

$$C = F(F+1) - I(I+1) - J(J+1);$$

$$F = I + J, I + J - 1, \dots |I - J|;$$

$$A = \frac{\mu_I \overline{H(0)}}{IJ};$$

$$B = eQ \overline{\phi_{JJ}(0)}.$$

E_J is the fine structure energy, and the hyperfine splitting is given by the last two terms. The term $A \frac{C}{2}$ represents the splitting due to the nuclear magnetic moment which is dependent upon the magnetic moment μ_I , the magnetic field produced by the nucleus $\overline{H(0)}$ and the product of the quantum numbers IJ which represents the coupling of the angular momentum vectors through the magnetic interaction where $I = \frac{3}{2}$ for ^{87}Rb and $I = \frac{5}{2}$ for ^{85}Rb . The last term represents the quadrupole interaction which depends on Q , the quadrupole moment, $\overline{\phi_{JJ}(0)}$, the vector gradient of the electric field of the orbital electrons having cylindrical symmetry about the J axis evaluated at the nucleus, and e is the absolute value of the elementary charge.

The relative line positions are given in Table 2 and are cited from (5). The first half of the table provides the A and B spectroscopic constants which can be used to determine the relative line positions as in Figure 7. The figure accurately represents the relative line positions within each manifold but the spacing between manifolds is not to scale. The relative line positions are computed in the second half

of Table 2 using

$$rp_i = \frac{\lambda_0^2}{c} \left[\left(E_F^{5^2P_J} - E_F^{5^2S_{\frac{1}{2}}} \right) - \left(E_{F'}^{5^2P_J} - E_{F'}^{5^2S_{\frac{1}{2}}} \right) \right] \quad (4)$$

where the subscript i is an arbitrary integer assignment for each of the energy differences. All line positions are reported relative to the $S_{\frac{1}{2}}(F=2)$ to $P_{\frac{1}{2}}(F=2)$ transition in ^{87}Rb for the D_1 line and to the $S_{\frac{1}{2}}(F=2)$ to $P_{\frac{3}{2}}(F=3)$ transition in ^{87}Rb for the D_2 line. The ^{85}Rb shifts are relative to the $S_{\frac{1}{2}}(F=3)$ to $P_{\frac{1}{2}}(F=2)$ transition for the D_1 line and to the $S_{\frac{1}{2}}(F=3)$ to $P_{\frac{3}{2}}(F=2)$ transition for the D_2 line. This requires an additional parameter, the spacing between the ^{87}Rb and the ^{85}Rb lines. This spacing has been measured (10) for the D_1 line as $-0.001483(2)$ nm and for the D_2 line as $-0.001902(6)$ nm. Though this parameter is known it was allowed to float during the data reduction to determine if this spacing was affected by the pressure line shift and thus determine if the line shift is different for each of the isotopes.

Table 2. A and B coefficients and relative line positions, rp_i .

Ref(5)	^{87}Rb		^{85}Rb	
MHz	A	B	A	B
$5^2S_{\frac{1}{2}}$	3417.34130642(15)	-	1011.910813(2)	-
$5^2P_{\frac{1}{2}}$	406.2(8)	-	120.72(25)	-
$5^2P_{\frac{3}{2}}$	84.845(55)	12.52(9)	25.009(22)	25.88(3)

rp_i	^{87}Rb			^{85}Rb		
nm	F	1	2	F	2	3
$P_{\frac{1}{2}}$	1	-0.01268	0.00171	2	-0.00639	0
	2	-0.01439	0	3	-0.00715	-0.00076
$P_{\frac{3}{2}}$	0	-0.01286	-	1	-0.00610	-
	1	-0.01301	0.00086	2	-0.00616	0
	2	-0.01332	0.00054	3	-0.00628	-0.00012
	3	-	0	4	-	-0.00037

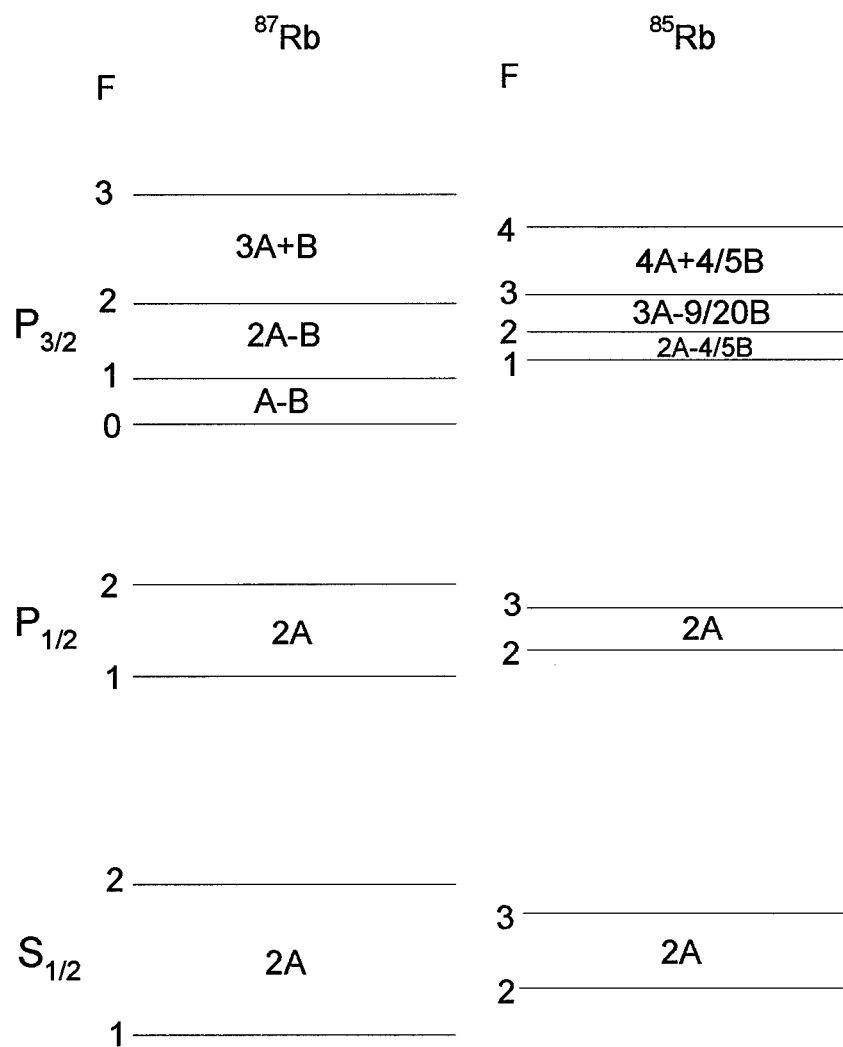


Figure 7. Rubidium 85 and 87 5^2P hyperfine split energy levels.

Figures 8 and 9 represent typical absorption spectra for the D_1 and the D_2 lines respectively with argon as the collision partner. These figures display the pressures 0, 50, 100 and 200 Torr which clearly shows the broadening and line shift which occurs as the gas pressure is increased. It almost appears as though the line shifts and broadening can be directly determined from the figures. Unfortunately, each of the observed peaks is a convolution of several transitions leading to inaccurate values for the pressure broadening. Therefore, to extract the line shift and pressure broadening coefficients a least squares curve fit which takes into account each of the individual transitions must be employed.

2.4 Data analysis

As discussed above, spectra were recorded simultaneously from both a reference cell and from the cell with the selected gas. The data from each cell must be analyzed in a different manner. The peaks from the two different cells are different in nature. The pressure in the reference cell was approximately 1 mTorr; therefore the data from the reference cell is composed of several Gaussian (Doppler broadened) peaks. The data acquired from the cell with the buffer gas is composed of several peaks with each peak being a convolution of a Gaussian and a Lorentzian (pressure broadening) profile. This sort of profile is characterized as a Voigt profile and is much more computationally intensive than the Gaussian profile alone.

The data was reduced using a user defined function in the software package Table Curve. The software allowed the use of predefined functions for the Voigt and Gaussian profiles.

$$Voigt(a_0, a_1, a_2, a_3) = \frac{\int_{-\infty}^{\infty} \left(\frac{a_0 e^{-y^2}}{a_3^2 + \left[\frac{x-a_1}{a_2} - y \right]^2} \right) dy}{\int_{-\infty}^{\infty} \left(\frac{e^{-y^2}}{a_3^2 + y^2} \right) dy} \quad (5)$$

$$Gaussian(a_0, a_1, a_2) = a_0 e^{-.5 \left(\frac{x-a_1}{a_2} \right)^2} \quad (6)$$

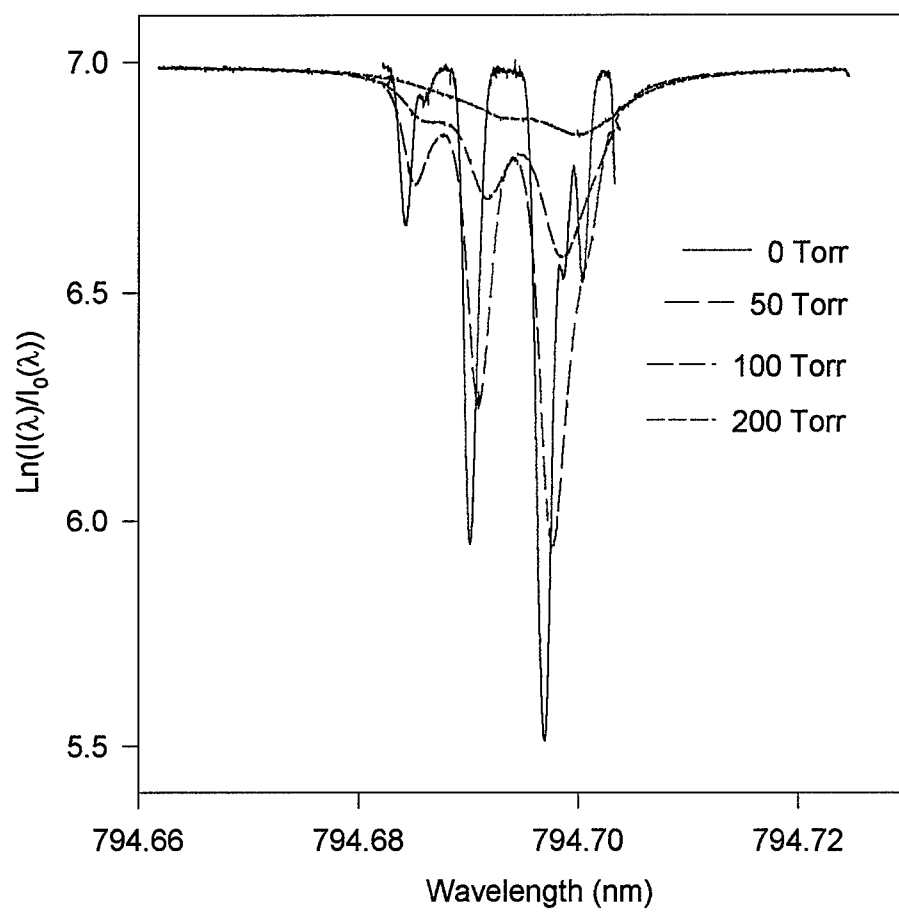


Figure 8. Typical absorption spectra near $\lambda = 794.7$ nm at $T=395$ K with argon as the collision partner.

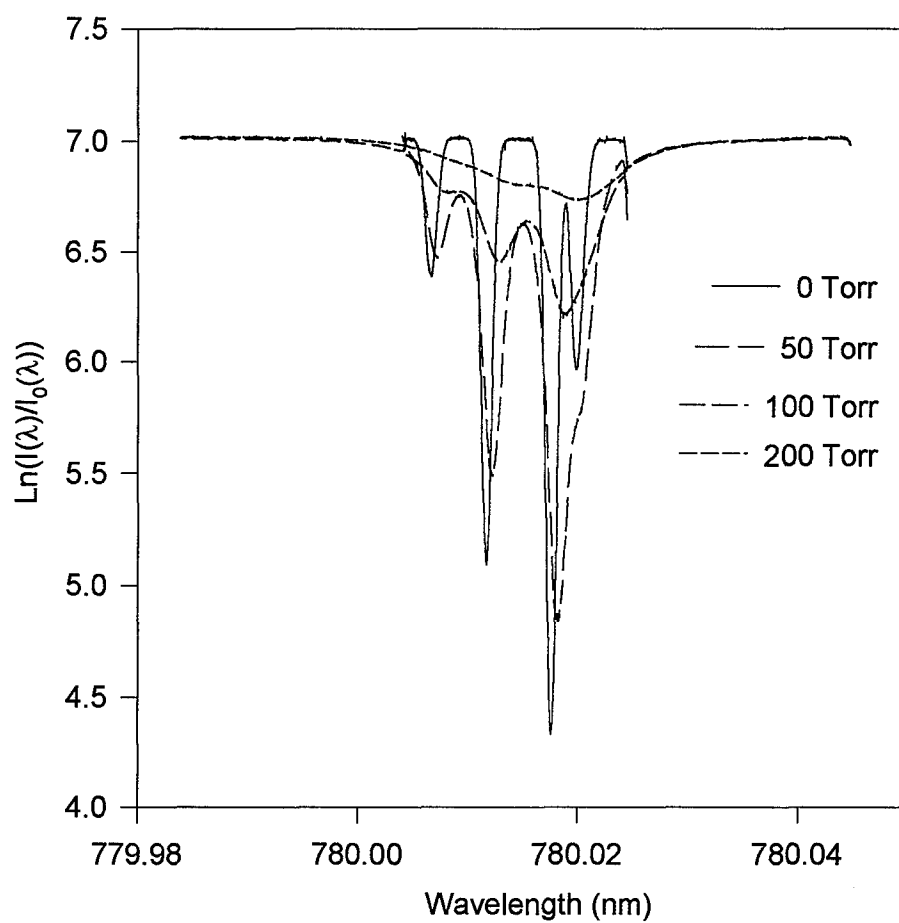


Figure 9. Typical absorption spectra near $\lambda = 780.0$ nm at $T=395$ K with argon as the collision partner.

The arguments of these functions are defined as follows:

$$Voigt(Amplitude, LineCenter, GaussianFWHM, \frac{LorentzianFWHM}{GaussianFWHM})$$

$$Gaussian(Amplitude, LineCenter, FWHM)$$

where FWHM is the full width at half maximum. Using these definitions the following expressions were used to curve fit the absorption spectra. The data from the cell with the selected gas was analyzed using equation 7 and the data from the reference cell was analyzed using equation 8:

$$\ln \left(\frac{I(\lambda)}{I_0(\lambda)} \right) = A + B\lambda + \sum_{i=1}^{8,12} Voigt(Cri_{i^{85,87}Rb_i}, D + \lambda_0 + rp_i, E_0, \frac{F}{E_0}), \quad (7)$$

$$\ln \left(\frac{I(\lambda)}{I_0(\lambda)} \right) = A + B\lambda + \sum_{i=1}^{8,12} Gaussian(Cri_{i^{85,87}Rb_i}, D + \lambda_0 + rp_i, E). \quad (8)$$

The first thing to be noticed in these expressions is the summation from 1 to 8 or to 12. Because there are 8 hyperfine split components in the D_1 line the summation ranges from 1 to 8 and since there are 12 components in the D_2 line the summation must range from 1 to 12. Equations 7 and 8 can be seen graphically represented in Figure 10.

The parameters A, B, C, D, E and F in equations 7 and 8 are curve fit parameters and are defined as follows. The terms A and B are the parameters used to fit the base line. The value for A was ≈ 3.2 for the reference cell and ≈ 7 for the data cell which appropriately reflects the relative detectivities of the incident and transmitted signals. The slope characterized by B was very small ≈ 0.1 % of the total change in the vertical axis. The subsequent terms are more easily explained by discussing their

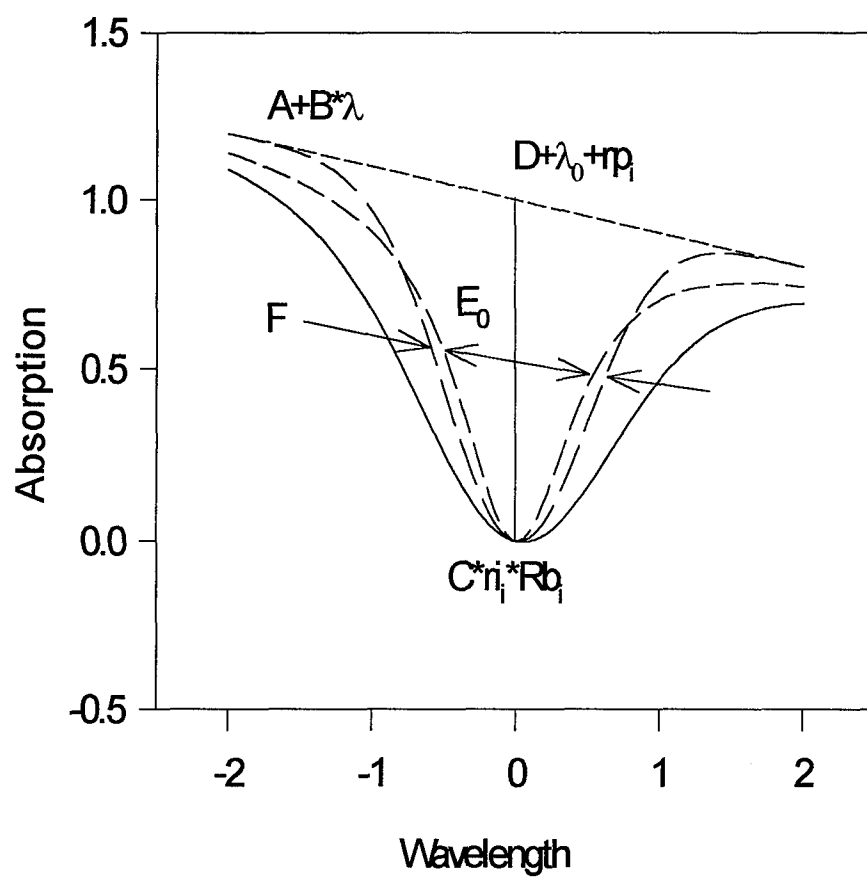


Figure 10. Single peak to illustrate the curve fitting process.

role in each position of the Voigt or Gaussian function. The first term ($Cri_i^{85,87}Rb_i$) represents the amplitude of each individual peak. The amplitude of each peak is dependent upon its line strength ri_i found in Table 1 and the rubidium concentration C which must be corrected for the relative isotopic abundance $^{85,87}Rb_i$. The rubidium concentration determined in this manner is $\approx 10^{-6}$ Torr which indicates a source temperature of ≈ 310 K. This temperature is less than the reported temperature of 395 K because the observation region was held at a much higher temperature to prevent plating of the rubidium on the windows. The next term ($D + \lambda_0 + rp_i$) is the line center of each peak where λ_0 is either 794.7 nm for the D_1 line or 780.0 nm for the D_2 line. The term rp_i is the relative position of each of the peaks which is given in Table 2. The D curve fit parameter serves two purposes. Because there is some inherent error in the initial scan wavelength of the laser this parameter D_{Ref} was curve fit using the reference cell data to characterize this source of error. For the cell with the gas D_{Buf} represents a characterization of the line shift plus the laser scan error. By differencing the values from the reference cell and the data cell the scan error is removed and the pressure line shift is determined. A plot of these shifts, $D_{Buf} - D_{Ref}$, as a function of pressure for each gas is shown in Figures 12, 14 and 16. A discussion of these figures can be found in the next section. The next term E or E_0 represent the Doppler FWHM of the peaks. This parameter was assumed to be the same for all peaks. For the data cell this parameter was not allowed to float and was fixed at the value E_0 . This value was determined by curve fitting the 0 Torr spectrum from the buffer gas cell. Using these line-widths the temperature of the cells were determined to be $T=395$ K for the buffer gas cell and $T=360$ K for the reference cell. The last term ($\frac{F}{E_0}$), which is only in the Voigt profile, is a characterization of the Lorentzian FWHM where the ratio is used in the function to force the software to return the desired width in the F parameter. A plot of these widths as a function of pressure for each gas is shown in Figures 13, 15 and 17. A discussion of these figures can be found in the next section. Figure 11 illustrates the

quality of a typical curve fit. The figure also displays the 95 % confidence limits of the fit.

At this point a discussion of the error in the experiment is in order. The largest source of error was generated in calibrating the wavelength axis. During a data scan the laser started its scan and then signaled the computer to start recording data from the lock-in amplifiers. When the scan ended the computer was then told to stop acquiring data. Though the initial wavelength and the scan length were known and the horizontal axis (wavelength axis) could be created, the laser had an initial scan position error of ± 25 MHz and linearity error of $\approx \pm 200$ MHz. Therefore a refinement of the wavelength axis was required. This problem was solved by using the reference cell data and curve fitting the ^{87}Rb hyperfine split lines with a curve fit parameter that could characterize any errors in the wavelength axis and provide a means of further refining the axis. The error in the corrected wavelength axis was typically on the order of 50 MHz over the entire 10 GHz scan region. Therefore a minimum error of 0.5 % should be expected in the line shift and pressure broadening coefficients.

Another source of error is in the statistical nature of the data acquisition. This error is characterized by one standard deviation of the curve fit parameter from the fits to the absorption spectrum. To determine the impact of this error on the reported rates, a characterization of the error in the slope Δm MHz per Torr was carried out on the D_1 pressure broadened data for CH_4 . This particular set of data was selected by a visual inspection of Figure 17 and noting that the data points showed a large scatter hence implying a reasonable characterization of this statistical error. The error analysis was carried out by using

$$\Delta m = \frac{\sum_{i=1}^N \frac{\sigma_i}{P_i}}{N} \quad (9)$$

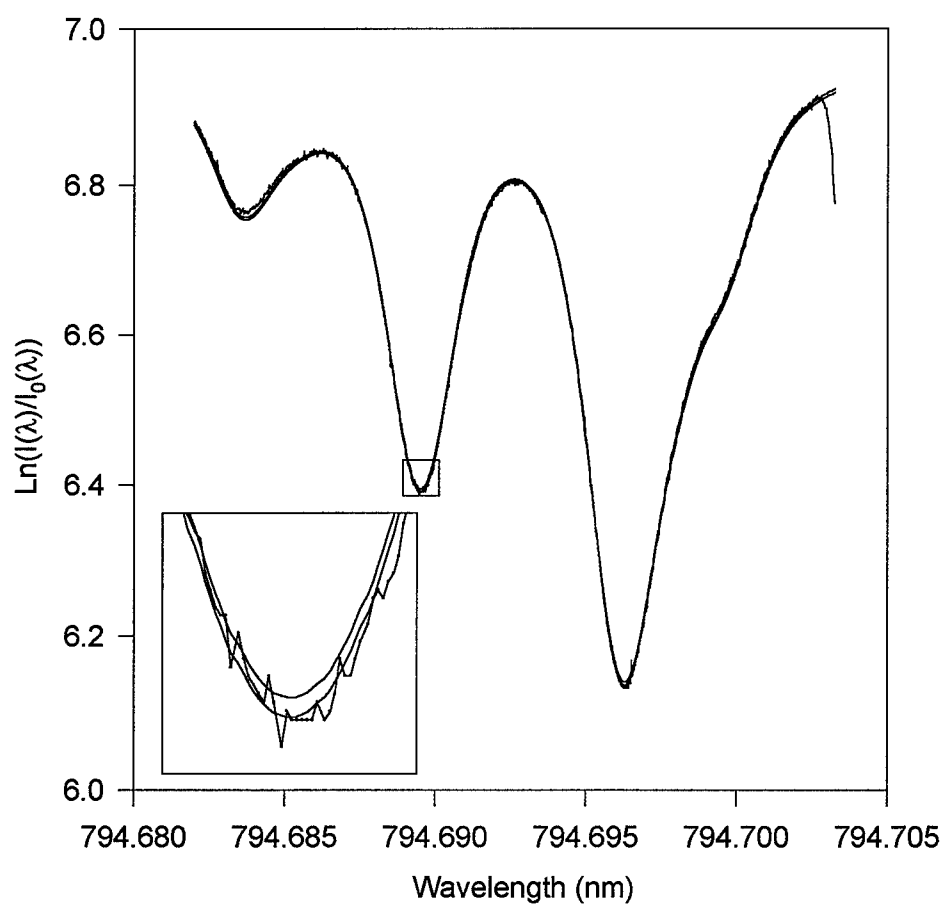


Figure 11. Curve fit of the D_1 line at 50 Torr of Helium. Displayed with the 95 % confidence limits. The expanded region is provided to illustrate the quality of the curve fits.

where σ_i is the standard error for each data point determined from the curve fit to the spectrum, P_i is the pressure of each data point and N is the total number of data points. Using this to characterize the error for the specified line leads to a value $\Delta m = 0.117$ MHz per Torr which is 0.4 % of the measured 29.1 MHz per Torr value. This value is very low because of the quality of the data and the quality of the fit to the data.

Because one of these errors is systematic and the other is statistical, the total expected minimum error is the sum of these two. For this particular case the minimum expected error is 0.26 MHz per Torr which is less than the reported value of 0.4 MHz per Torr. The reported error was arrived at based solely on the statistical scatter in the reduced data which is larger than the known sources of error.

Finally, it was stated earlier that the relative spectral position of fluorescence from the ^{87}Rb and ^{85}Rb would be characterized experimentally. This shift was measured using

$$\ln \left(\frac{I(\lambda)}{I_0(\lambda)} \right) = A + B\lambda + \sum_{i=1}^{8,12} \text{Voigt}(Cr_i^{85,87}\text{Rb}_i, D + G_{i(85\text{Rb})} + \lambda_0 + rp_i, E_0, \frac{F}{E_0}), \quad (10)$$

where $G_{i(85\text{Rb})}$ is a curve fit parameter which characterizes the shift between the two isotopes and is zero for all ^{87}Rb lines. The values measured are for the D_1 line $G_i = -0.001462(4)$ nm and for the D_2 line $G_i = -0.001892(2)$ nm. These values are in very good agreement with the values previously cited. These values can also be computed using the A and B coefficients in Table 2 and by taking into account the isotope shift of the 5^2P levels D_1 77 ± 4 MHz (32) and D_2 75 ± 4 MHz (19). The values determined in this manner are for the D_1 line -0.001485 nm and for the D_2 line -0.001812 nm, which again are in good agreement with the experimentally obtained values. A comparison of these values is given in Table 3.

Additionally, if equation 10 is used to perform the curve fitting at pressures greater than zero Torr, a characterization of the line shift for each of the two isotopes

Table 3. $\Delta\lambda$ for the ^{87}Rb ($5^2S_{\frac{1}{2}}, F = 2$ to $5^2P_{\frac{1}{2}}, F = 2$) - ^{85}Rb ($5^2S_{\frac{1}{2}}, F = 3$ to $5^2P_{\frac{1}{2}}, F = 2$) for the D_2 line and ^{87}Rb ($5^2S_{\frac{1}{2}}, F = 2$ to $5^2P_{\frac{3}{2}}, F = 3$) - ^{85}Rb ($5^2S_{\frac{1}{2}}, F = 3$ to $5^2P_{\frac{3}{2}}, F = 2$) for the D_2 line.

D_1 nm	D_2 nm	Ref
-0.001462(4)	-0.001892(2)	This work
-0.001483(2)	-0.001902(6)	(10)
-0.001485(8)	-0.001812(9)	(5) (19) (32)

is possible. This characterization was carried out and the results showed no shift within the experimental error limits $(\pm 0.03) \frac{\text{MHz}}{\text{ Torr}}$.

2.5 Results of the data reduction

A linear fit to the data in figures 12-17 provide the line shifts and broadening coefficients. The resulting linear curve fits are also shown in these figures. The slopes and the error (one standard deviation) from these fits are reported in Tables 4 and 5. The data were tested for curvature using a quadratic fit. The ratio of the quadratic coefficient to the slope yields a curvature less than 0.05% which is less than the error characterized by the scatter in the data which is $\approx 1\%$. For completeness, the intercepts for these fits are reported in Table 6. A weighted averaging was performed on the intercepts and is also given in Table 6. The origin is the expected intercept for the line shift, but the intercept for the pressure broadening data should yield the natural line width.

These results have some interesting features. The first is the anomalous affect helium has on the line shift of the rubidium D_1 line. Typically the frequency shift is towards lower frequencies but with helium the shift is strongly towards higher frequencies.

A typical characteristic of the pressure broadening for the rare gases is that the broadening is the same for both the D_1 and D_2 lines. This trend does not appear

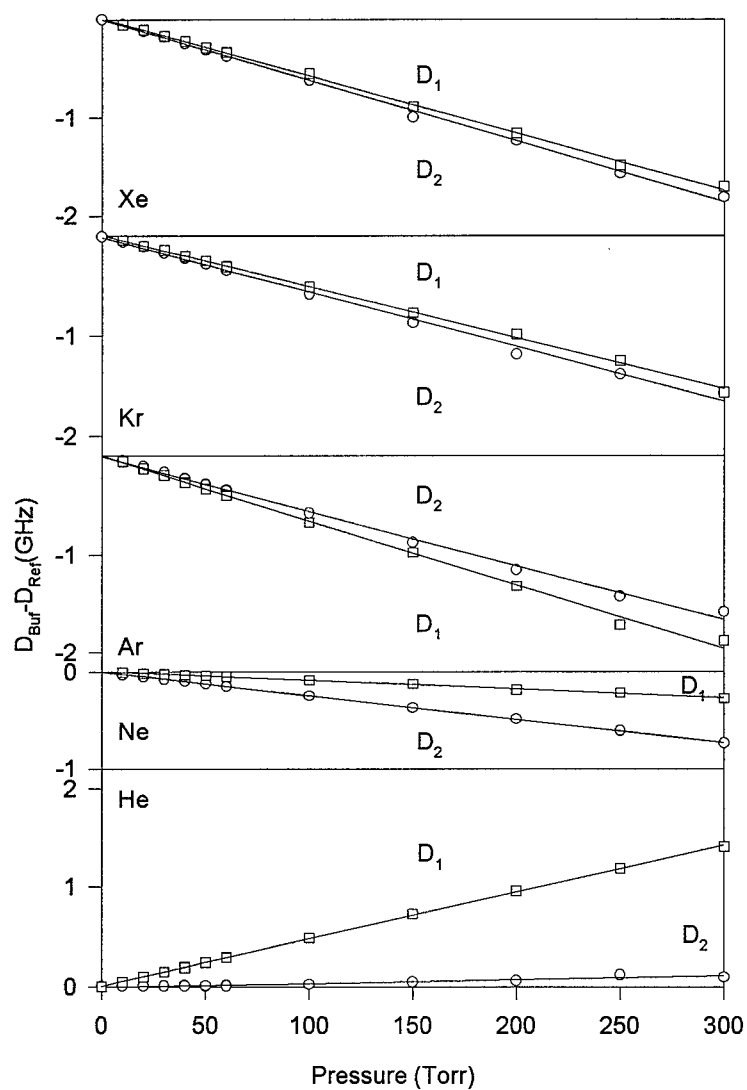


Figure 12. Line shift of the D_1 and D_2 lines in rubidium induced by rare gasses.

to hold true for the molecular gases. There is a very pronounced difference in the broadening rates for hydrogen and deuterium.

The line shifts and broadening coefficients are given in Tables 4 and 5 with one standard deviation reported for the error. These values are compared to other previously measured values and are found to be in very good agreement. The typical error bound on the data acquired in this study is much smaller than all previous measurements. This reduction in error is attributed to the improvement in resolution over previous measurements. The employment of absorption spectroscopy resulted in the acquisition of Doppler limited resolution rubidium spectra. Previous measurements of the rubidium pressure broadening used a Fabry-Perot interferometer (42), monochromator (62) and a magnetic-scanning technique (13). This high resolution in the current experiment allowed a very accurate characterization of the Doppler width which is critical to the removal of the Doppler portion of the observed Voigt profile thus allowing a precise determination of the Lorentzian (pressure broadening) width.

2.6 Determination of the interaction potentials

The classical model for collision broadening represents an atomic radiator as an elastically bound oscillating electron. The problem of collision broadening is to calculate the spectrum of an oscillator disturbed by collisions with other atoms or molecules. Such a model is termed the Impact Theory and is fully derived in reference (70). The underlying assumption of the model is that collisions only affect the phase of the oscillator and not the amplitude. The model is applied to the experimental data in a reverse manner to allow the determination of the interaction potentials between rubidium and the neutral gas particles. Several assumptions are made to construct this model. The first is a low pressure or high velocity assumption which is more rigorously stated as follows. The duration of a collision must be much smaller than the time between collisions therefore, most of the radiation or absorption

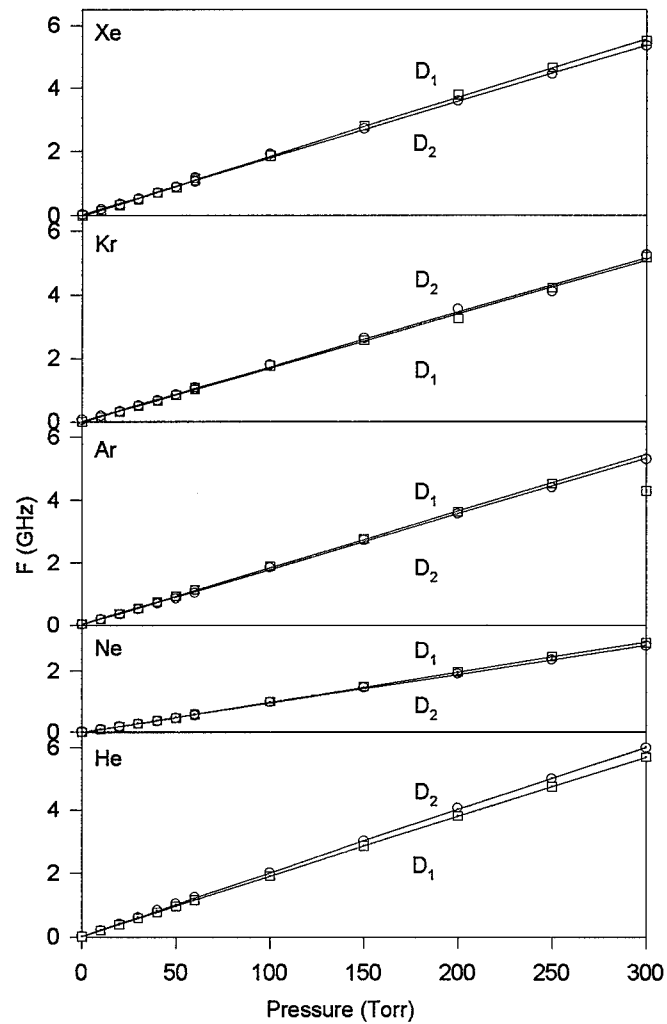


Figure 13. Pressure broadening of the D_1 and D_2 lines in rubidium induced by the rare gasses.

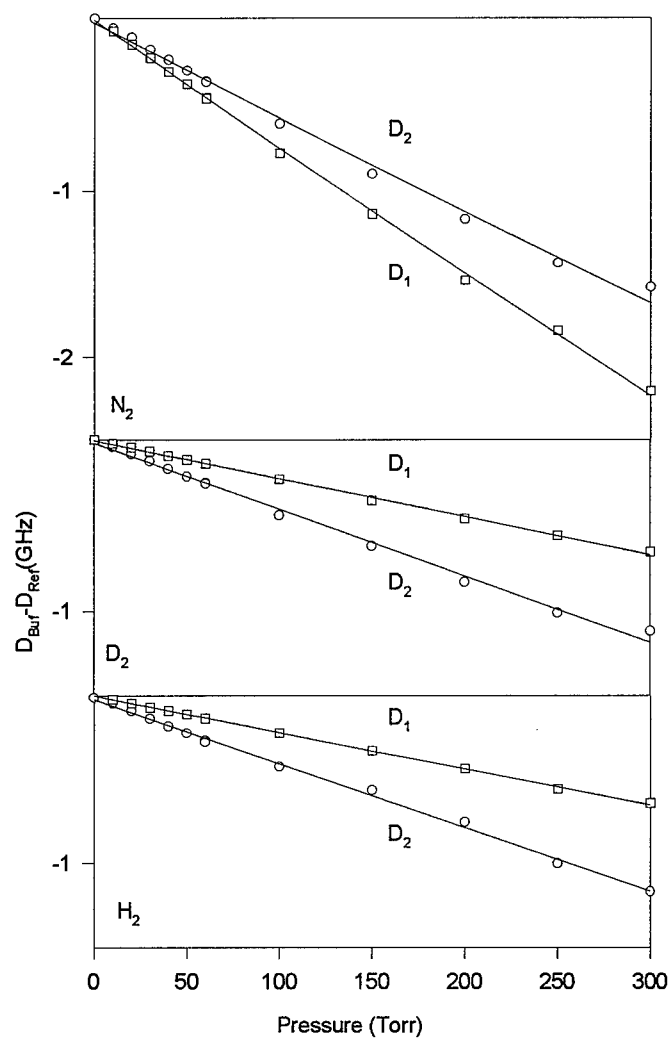


Figure 14. Line shift of the D_1 and D_2 lines in rubidium induced by H_2 , D_2 and N_2 .

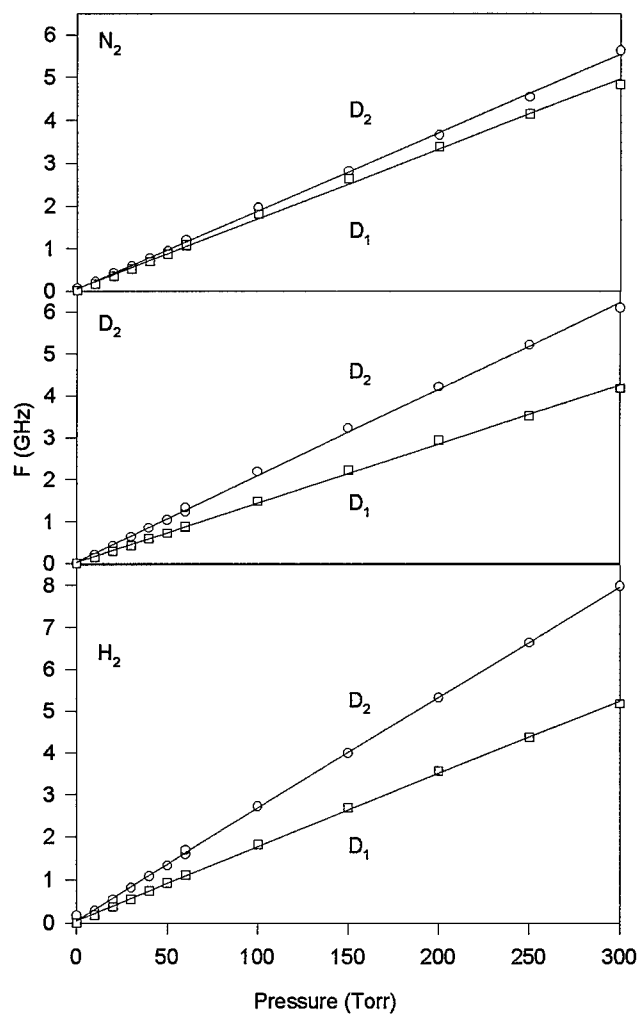


Figure 15. Pressure broadening of the D_1 and D_2 lines in rubidium induced by H_2 , D_2 and N_2 .

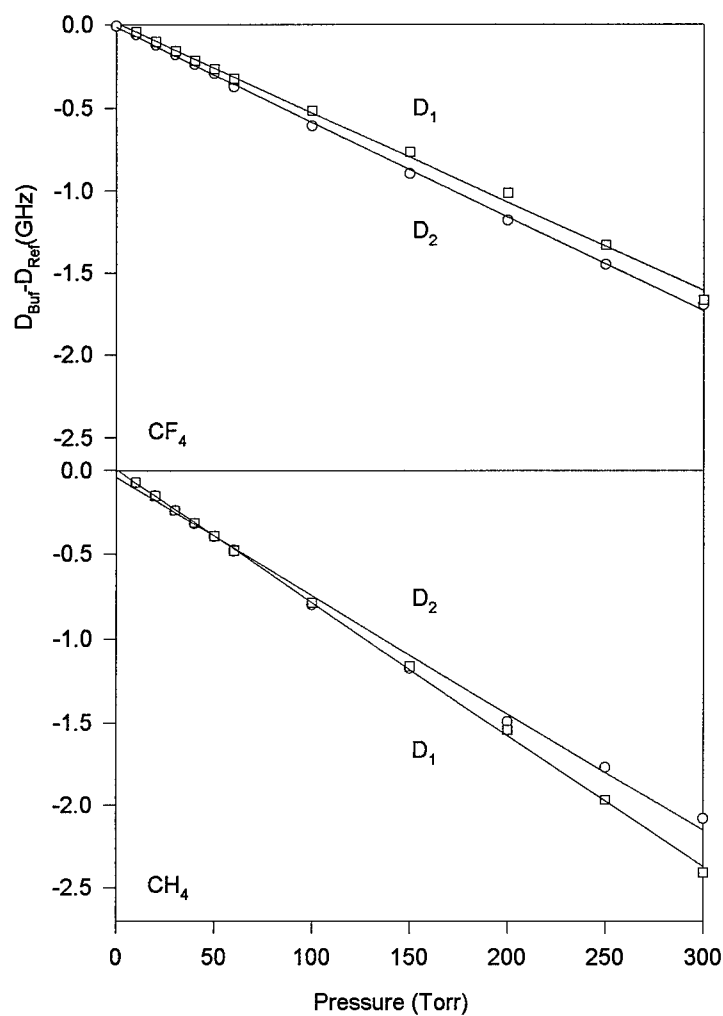


Figure 16. Line shift of the D_1 and D_2 lines in rubidium induced by collisions with CH_4 and CF_4 .

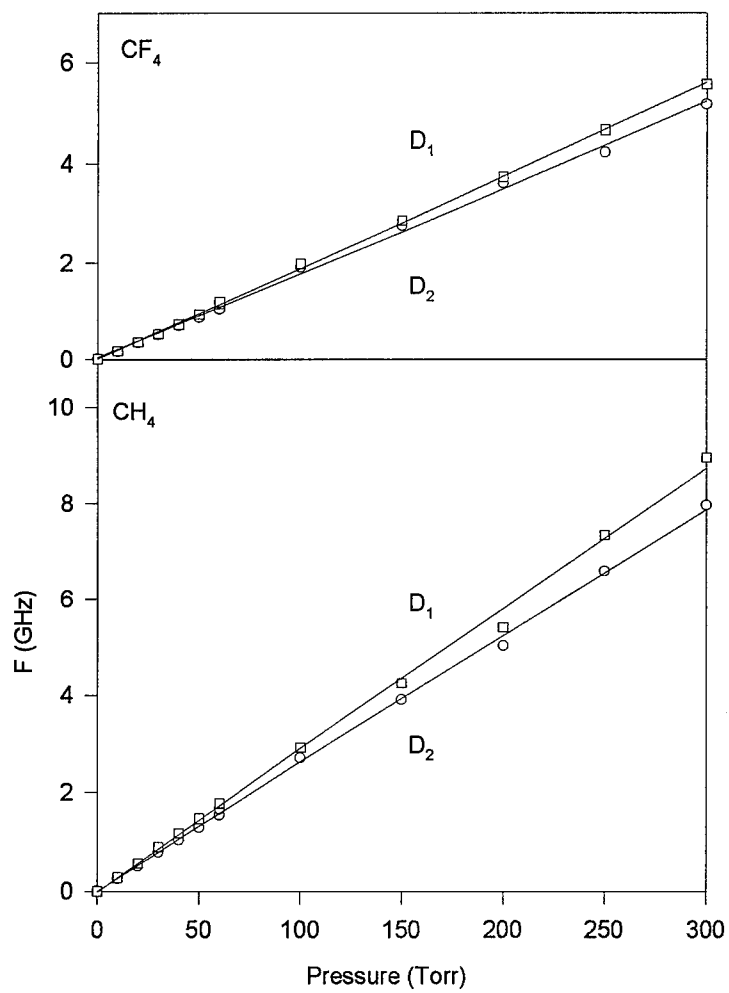


Figure 17. Pressure broadening of the D_1 and D_2 lines in rubidium induced by CH_4 and CF_4 .

Table 4. Shifts and broadening of the D_1 resonance line of rubidium accompanying collisions with inert-gas atoms and selected molecules.

Per- tur- bing gas	Shifts ($\frac{MHz}{Torr}$)					
	Experimental				Theoretical	
	This work 394K	(42) 320K	(44) 293K	(62) 320K	(36) 293K	(67) 323K
He	$+4.71 \pm 0.02$	$+5.0 \pm 1$	$+6.2 \pm 0.5$			
Ne	-0.90 ± 0.01	-1.7 ± 0.5	-1.2 ± 0.6	-0.37 ± 0.3		
Ar	-6.77 ± 0.06	-6.7 ± 0.4	-6.6 ± 0.4	-7.1 ± 0.7	-6.5	-5.4
Kr	-5.12 ± 0.05	-5.0 ± 1	-5.5 ± 0.5	-7.2 ± 0.5	-4.7	-5.5
Xe	-5.84 ± 0.06	-6.0 ± 0.2	-7.2 ± 0.9	-7.6 ± 0.7	-4.74	-6.3
H_2	-2.17 ± 0.02					
D_2	-2.22 ± 0.03					
N_2	-7.41 ± 0.06					
CH_4	-7.92 ± 0.05					
CF_4	-5.41 ± 0.08					

Per- tur- bing gas	Broadening ($\frac{MHz}{Torr}$)					
	Experimental				Theoretical	
	This work 394K	(42) 320K	(44) 293K	(62) 320K	(36) 293K	(67) 323K
He	18.90 ± 0.09	19 ± 2	18.3 ± 0.9	18.5 ± 3.3		
Ne	9.84 ± 0.05	7 ± 2	10.1 ± 1.6	9.4 ± 1.3		
Ar	18.11 ± 0.09	21 ± 2	19.4 ± 1.0	18.2 ± 2.4	16.7	14.7
Kr	17.1 ± 0.2	15 ± 1	17.3 ± 0.9	18.2 ± 1.7	22.4	15.2
Xe	18.6 ± 0.1	15 ± 3	20.8 ± 1.0	20.9 ± 2.4	21	17.4
H_2	17.3 ± 0.1					
D_2	14.1 ± 0.2					
N_2	16.3 ± 0.2					
CH_4	29.1 ± 0.4					
CF_4	18.7 ± 0.1					

Table 5. Shifts of the D_2 resonance line of rubidium accompanying collisions with inert-gas atoms and selected molecules. [†] Calculated taking account of the anisotropy of the interaction. ^{††} Calculated without taking account of the anisotropy of the interaction.

Per- tur- bing gas	Shifts ($\frac{MHz}{Torr}$)						
	Experimental				Theoretical		
	This work 394K	(42) 320K	(14) (13) 293K	(62) 320K	[†] (36) 293K	^{††} (36) 293K	(68) 323K
He	$+0.37 \pm 0.03$	$+0.9 \pm 0.2$	$+2.2 \pm 0.5$	-0.74 ± 0.3			
Ne	-2.44 ± 0.01	-2.7 ± 0.2	-3.7 ± 0.5	-2.0 ± 0.3	1.1	1.7	
Ar	-5.76 ± 0.02	-5.7 ± 0.2	-7.1 ± 0.8	-8.1 ± 1.2	-7.3	-7.9	-5.3
Kr	-5.5 ± 0.1	-5.8 ± 0.2	-8.4 ± 1.0	-8.1 ± 0.5	-5.3	-5.6	-5.5
Xe	-6.19 ± 0.08	-6.0 ± 0.2	-7.0 ± 1.1	-9.1 ± 0.7	-6.8	-4.3	-6.3
H_2	-3.83 ± 0.06						
D_2	-4.09 ± 0.04						
N_2	-5.79 ± 0.05		-8.2 ± 0.6				
CH_4	-7.0 ± 0.1		-11.3 ± 0.6				
CF_4	-5.73 ± 0.05						

Per- tur- bing gas	Broadening ($\frac{MHz}{Torr}$)						
	Experimental				Theoretical		
	This work 394K	(42) 320K	(14) (13) 293K	(62) 320K	[†] (36) 293K	^{††} (36) 293K	(68) 323K
He	20.01 ± 0.07	15 ± 2	22.5 ± 1.1	18.5 ± 3.3			
Ne	9.47 ± 0.05	13 ± 3	9.4 ± 0.4	9.8 ± 1.7	16.1	18.0	
Ar	17.7 ± 0.1	18 ± 2	19.8 ± 0.5	18.5 ± 2.4	18.3	18.1	14.6
Kr	17.2 ± 0.2	17 ± 2	17.5 ± 1.0	16.2 ± 1.3	21.3	25.8	15.1
Xe	17.8 ± 0.1	19 ± 2	19.8 ± 0.9	21.2	23.4	23.3	17.2
H_2	26.4 ± 0.2						
D_2	20.6 ± 0.2						
N_2	18.3 ± 0.2		18.9 ± 0.5				
CH_4	26.2 ± 0.3		26.0 ± 0.7				
CF_4	17.3 ± 0.3						

Table 6. The intercepts for the linear curve fits of the pressure broadening and line shift data.

MHz	Intercepts			
Pertur- bing gas	D_1		D_2	
	Shift	Broadening	Shift	Broadening
He	$+5 \pm 2$	$+14 \pm 11$	-6 ± 4	$+9 \pm 8$
Ne	$+2 \pm 2$	-18 ± 7	-2 ± 2	-9 ± 7
Ar	$+11 \pm 6$	$+28 \pm 10$	$+4 \pm 2$	$+11 \pm 15$
Kr	$+10 \pm 7$	-13 ± 26	-10 ± 15	$+13 \pm 33$
Xe	$+9 \pm 8$	-18 ± 16	$+0 \pm 10$	$+27 \pm 19$
H_2	$+0 \pm 2$	$+47 \pm 15$	-20 ± 8	$+48 \pm 20$
D_2	-5 ± 3	$+30 \pm 20$	-7 ± 5	$+38 \pm 27$
N_2	-10 ± 8	$+71 \pm 29$	-9 ± 6	$+56 \pm 20$
CH_4	$+5 \pm 7$	-18 ± 58	-40 ± 18	-1 ± 33
CF_4	$+11 \pm 11$	$+10 \pm 19$	-15 ± 7	$+37 \pm 38$
Average	1 ± 4	6 ± 5	-2 ± 4	8 ± 3
Expected	0	5.7	0	5.9

will occur between collisions. This assumption is valid for pressures less than a few atmospheres. The second assumption is that the atoms move in straight lines which is not a valid assumption for the lighter collision partners. The third assumption concerns the relative velocity of the two colliding atoms. The assumption is that the relative velocity between the colliding atoms can be characterized by the average velocity between the colliding atoms. This assumption is necessary to decouple the Doppler and the pressure broadening.

Applying the impact theory using a Lennard-Jones (6,12) potential for the rubidium-collision partner interaction, the potential represents the difference between the initial and final state potentials,

$$V(R) = C_{12}R^{-12} - C_6R^{-6} \quad (11)$$

R is the interatomic separation and C_6 and C_{12} are the coefficients for the R^{-6} and R^{-12} parts of the potential respectively. The Impact Theory using this potential

yields the following relationships for the Lorentzian full width at half maximum γ and line shift β in Hz which were derived in reference (70)

$$\gamma = 4 \left(\frac{3\pi}{8} \right)^{\frac{2}{5}} N \bar{v}^{\frac{3}{5}} \left(\frac{C_6}{\hbar} \right)^{\frac{2}{5}} B(\alpha) \quad (12)$$

$$\beta = \left(\frac{3\pi}{8} \right)^{\frac{2}{5}} N \bar{v}^{\frac{3}{5}} \left(\frac{C_6}{\hbar} \right)^{\frac{2}{5}} S(\alpha) \quad (13)$$

where N is the number density of the perturbing gas, \bar{v} is the average velocity between the radiating atom and the perturbing gas. These expressions are arrived at by performing a Fourier transform of the displacement which is a function of time of a perturbed harmonic oscillator. The perturbation of the harmonic oscillator is a result of rubidium neutral gas particle interaction. By integrating over all possible impact parameters, ρ , the following integrals are obtained

$$S(\alpha) = \int_0^\infty x \sin(\alpha x^{-11} - x^{-5}) dx \quad (14)$$

$$B(\alpha) = \int_0^\infty x \sin^2 \left\{ \frac{1}{2}(\alpha x^{-11} - x^{-5}) \right\} dx. \quad (15)$$

where

$$\alpha = \frac{63\pi}{256} \left(\frac{8}{3\pi} \right)^{\frac{11}{5}} \bar{v}^{\frac{6}{5}} C_{12} \frac{\hbar^{\frac{6}{5}}}{C_6^{\frac{11}{5}}} \quad (16)$$

$$x = \rho \left(\frac{3\pi C_6}{8 \hbar \bar{v}} \right)^{\frac{1}{5}}. \quad (17)$$

The integrals of equations 14 and 15 and the ratio $\frac{S}{2B}$ are shown in Figure 18. Also displayed, are the observed ratios $\frac{\beta}{\gamma}$ for each of the collision partners. These ratios are depicted by the horizontal lines and the labeling for each gas is across the top of the figure. By finding the intersection between the ratio $\frac{\beta}{\gamma}$ and the ratio of $\frac{S}{2B}$, α can be determined. Once α is obtained equation 12 or 13 can be used to determine C_6 then in turn using equation 16, C_{12} can be determined. It should be noted that due to the oscillations in the solution an unambiguous determination of

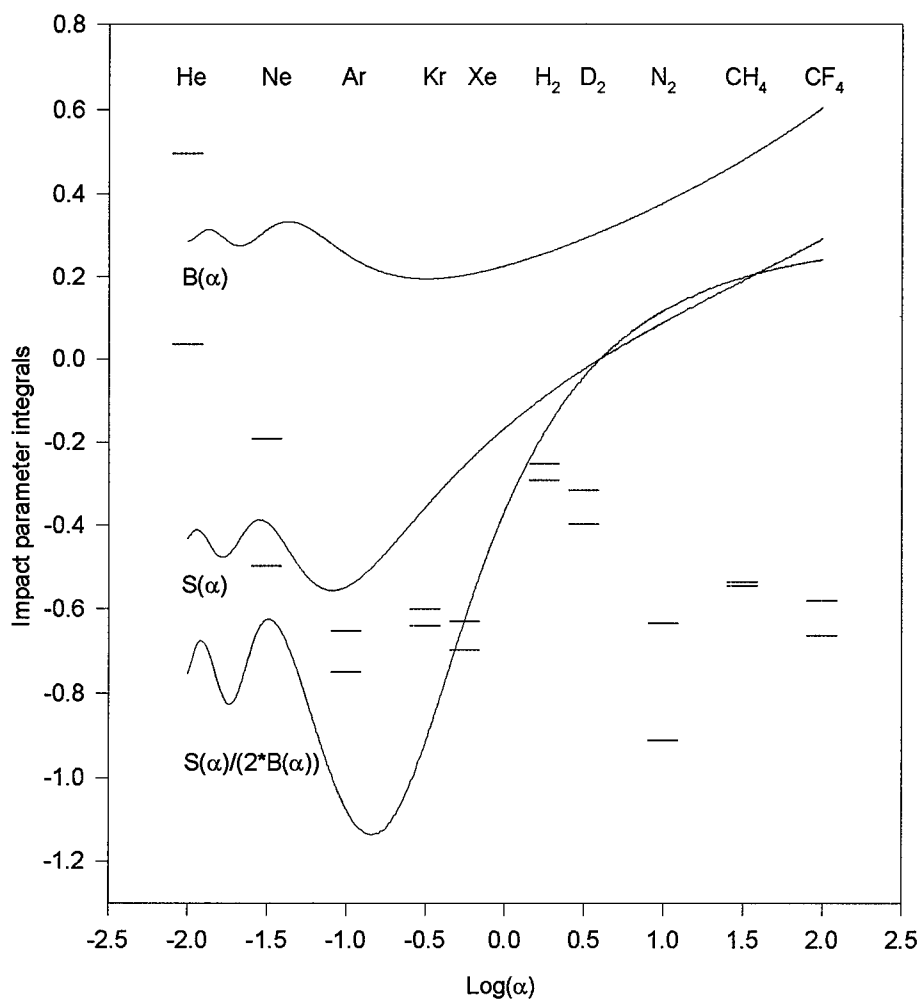


Figure 18. Solution to the impact approximation to determine the interaction potentials. Also shown are the ratios $\frac{\beta}{\gamma}$, denoted by the horizontal lines, for all of the collision partners.

α can not always be made. This technique does not always yield an unambiguous determination of C_6 and C_{12} . Table 8 lists the values for C_6 and C_{12} and Figures 19 and 20 graphically depict the potentials. For the ambiguous cases the values of α were restricted to the range of 0.16 to 10.0. This region was chosen because it most closely matched the unambiguous cases.

As can be seen in Figure 18 the ratio $\frac{\beta}{\gamma}$ for the D_1 line with helium as the collision partner does not intersect the curve for $\frac{S}{2B}$ thus the impact theory using a (6,12) potential will not yield meaningful results for this case unless α is allowed to go to infinity. This is equivalent to $C_6 = 0$. Therefore, using a potential $V(R) = C_{12}R^{-12}$, equations 18 and 19 are obtained from the impact theory which allows a straight forward determination of C_{12} (70).

$$\gamma = N\bar{v} \left[\pi^{\frac{1}{2}} \frac{C_{12}}{\bar{v}\hbar} \right]^{\frac{2}{11}} \frac{9.555 \times 10^{-3}}{\cos(\frac{\pi}{11})} \quad (18)$$

$$\beta = \pm N\bar{v} \left[\pi^{\frac{1}{2}} \frac{C_{12}}{\bar{v}\hbar} \right]^{\frac{2}{11}} \frac{9.555 \times 10^{-3}}{\sin(\frac{\pi}{11})} \quad (19)$$

It might be useful to note that a quantum mechanical theory of collision broadening exists. Using the same assumptions as outlined for the classical impact theory and adding the additional assumption that inelastic collisions can be neglected in the broadening process, then the quantum mechanical theory reduces to the classical impact theory (70). The assumption that the inelastic collisions can be neglected is valid if the cross-section for spin-orbit energy transfer are significantly smaller than the cross-section for a dephasing collision. For the rare gases this assumption is true because the spin-orbit energy transfer cross-sections are typically 10^3 to 10^5 times smaller than the cross-section for dephasing collisions. For the molecular species, the spin-orbit cross-section is ≈ 3 to 10 times smaller than the dephasing cross-section and, this assumption may not be valid for the molecular gases.

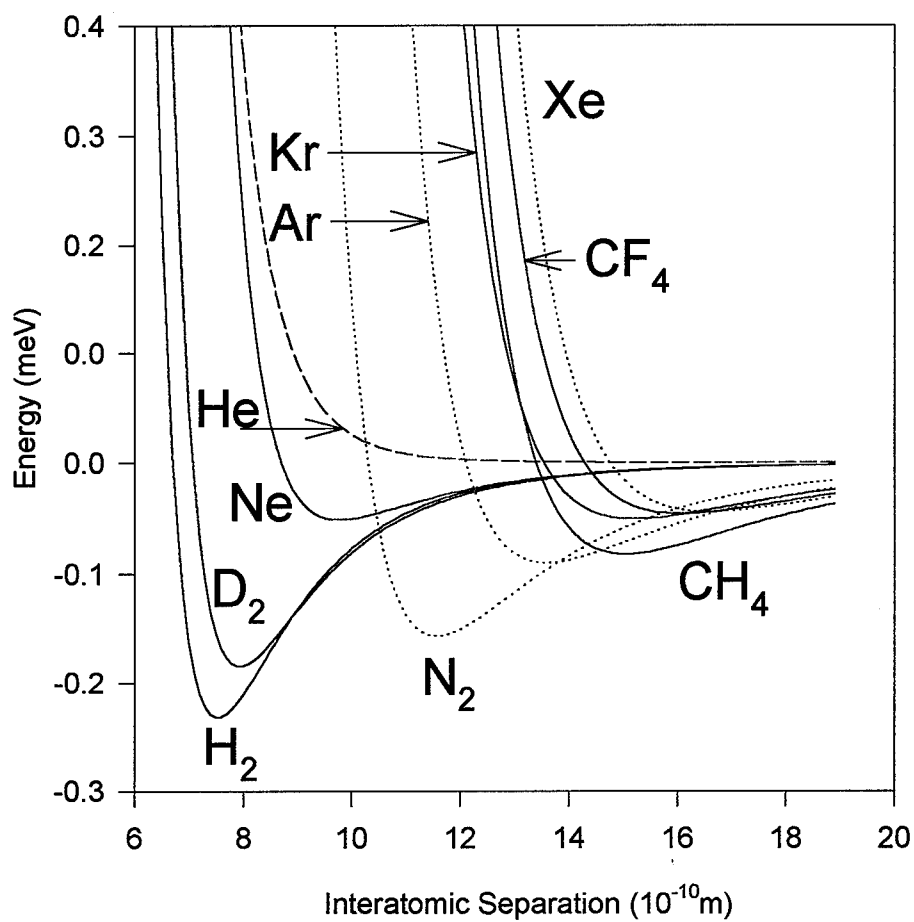


Figure 19. Interaction potential differences for the D_1 line. The solid lines depict the unambiguous potentials, the dotted lines depict the ambiguous potentials and the dashed line is for helium using the C_{12} potential.

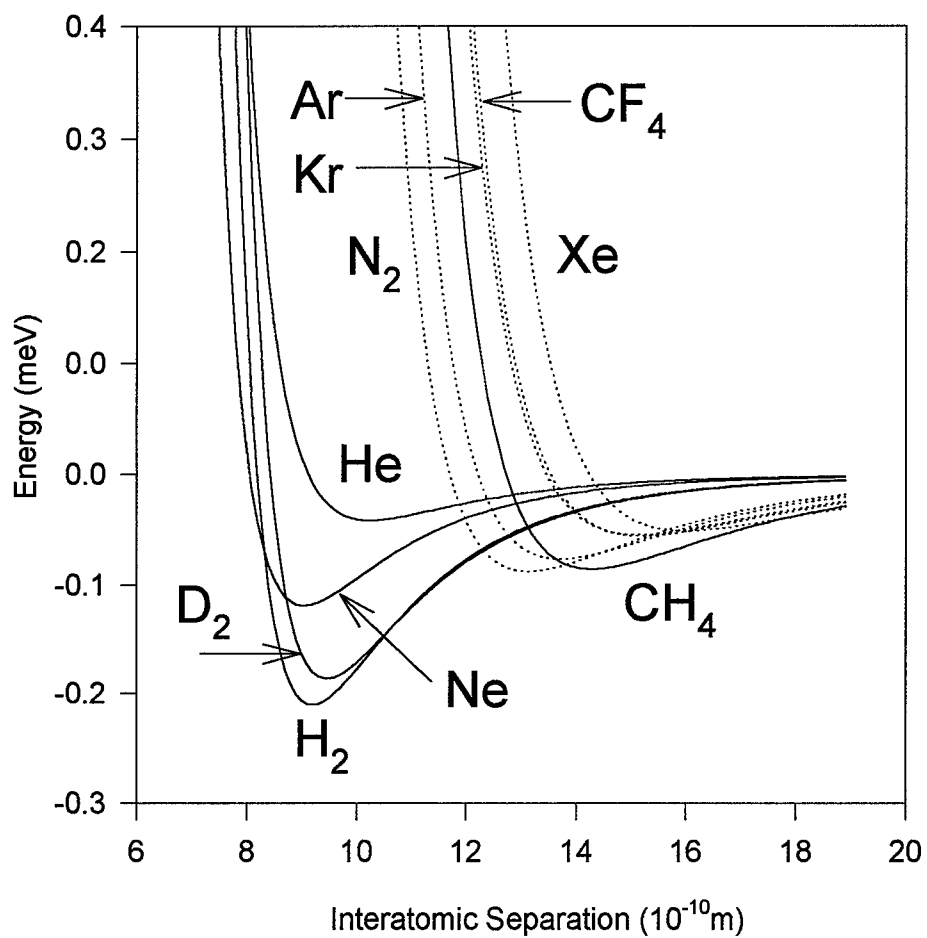


Figure 20. Interaction potential differences for the D_2 line. The solid lines depict the unambiguous potentials and the dotted lines depict the ambiguous potentials.

2.7 Theoretical determination of the interaction potentials

The long range, attractive, Van der Waals part of the potential between neutral atoms can be determined using the potential

$$V(R) = -C_6 R^{-6} \quad (20)$$

from reference (70) where C_6 is given by

$$C_6 = e^2 \alpha_d (\overline{r_{up}^2} - \overline{r_{lo}^2}) \quad (21)$$

and α_d is the dipole polarizability of the perturbing atom or molecule. The mean squared radius of the orbit of the optical electron in state $|k\rangle$, which defines a state $|n, l\rangle$ where the subscripts *up* and *lo* refer respectively to the upper and lower states of the transition. These states are given by

$$\overline{r_k^2} = \frac{1}{2} a_0^2 n^{*2} \{5n^{*2} + 1 - 3l(l+1)\}, \quad (22)$$

where a_0 is the radius of the first Bohr orbit, l is the orbital angular momentum quantum number and n^* is the effective principal quantum number of the state $|k\rangle$ with the values $n_{S_{\frac{1}{2}}}^* = 1.805$, $n_{P_{\frac{1}{2}}}^* = 2.28$ and $n_{P_{\frac{3}{2}}}^* = 2.293$ (84). The values for C_6 obtained using this method and the polarizabilities given in Table 7 are listed in Table 8.

A consideration in assessing the usefulness of the Impact Theory to determine the interaction potentials is the degree of agreement between the measured constants and the theoretically expected values. The constant C_{12} is not a reliable guide, because the theoretical value for C_{12} is a semi-empirical value (39). The constant C_6 as a theoretical estimate is more reliable and any discrepancy must throw doubt on the collision broadening theory. Table 8 shows both the theoretical estimate of the C_6 constant and the value determined experimentally from a fit to a (6,12) potential.

Table 7. Polarizability of the collision partners.

Gas	Polarizability $\alpha_d \text{\AA}^3$	Reference
He	0.201	(3)
Ne	0.390	(3)
Ar	1.62	(3)
Kr	2.46	(3)
Xe	3.99	(3)
H_2	0.790	(40)
D_2	0.7749	(40)
N_2	1.76	(40)
CH_4	2.60	(40)
CF_4	-	-

Table 8. C_6 and C_{12} constants for the 6,12 potential.

Gas	D_1			D_2		
	Experimental		Theoretical	Experimental		Theoretical
	6,12 Potential		Van der Waals	6,12 Potential		Van der Waals
	C_6 10^{-77}Jm^6	C_{12} 10^{-130}Jm^{12}	C_6 10^{-77}Jm^6	C_6 10^{-77}Jm^6	C_{12} 10^{-130}Jm^{12}	C_6 10^{-77}Jm^6
He	-	0.041	0.34	1.5	0.088	0.36
Ne	1.4	0.062	0.67	2.1	0.057	0.70
Ar	18	5.7	2.8	16	5.4	2.9
Kr	20	12	4.2	21	12	4.4
Xe	29	30	6.8	27	23	7.2
H_2	1.3	0.012	1.3	4.1	0.12	1.4
D_2	1.5	0.018	1.3	4.3	0.15	1.4
N_2	12	1.4	3.0	14	3.7	3.2
CH_4	31	18	4.4	23	9.8	4.7
CF_4	25	21	-	22	13	-

The experimental values exceed the theoretical values by factors of about three or four. This trend in the comparison of the theoretical and the experimental values for C_6 is in agreement with comparisons for other elements other than rubidium (70). A reasonable explanation for this discrepancy is the selection of a (6,12) potential to model the interaction. An improvement between the experimentally determined values for C_6 and the theoretically determined values of C_6 has been demonstrated using a (6,8,12) potential which supports the idea that higher terms in the interaction may not be negligible (70). The problem with applying a (6,8,12) potential is that with only the two inputs β and γ a unique determination of C_6 , C_8 and C_{12} can not be made without adding an additional constraint to the Cs.

2.8 Summary

The most fundamental contribution of this work is the measurement of the pressure broadening and pressure line shift for rubidium with H_2 , D_2 and CF_4 as collision partners. This data was not previously available. Additionally, this work has improved the accuracy of the values for the rare gases, N_2 and CH_4 . This increase in accuracy was primarily due to the increase in resolution made possible using absorption spectroscopy to probe the hyperfine structure in rubidium. Since the technique achieved Doppler limited resolution the Doppler width could be measured and removed accurately without the need to remove the line-shape imposed upon the observed spectra by a spectroscopic instrument.

This work also attempted to determine the interaction potentials for rubidium with the collision partners by applying the Impact Theory for pressure broadening. The model has several flaws which call into question the validity of the potential determined in this fashion. The first difficulty was the inability of the model, using the (6,12) potential, to uniquely determine the coefficients for the potential using only the pressure broadening and pressure line shift rates. Additional questions of the validity arise when the underlying assumptions are more closely examined. This

model assumes no spin-orbit transfer occurs during a collision. This assumption, while valid for the rare gases, is clearly invalid for the molecular gases. Additionally, the construction of the model only averages over the impact parameter which is acceptable for the spherically symmetric noble gases. However, for a molecule like N_2 , it would appear that an average over the additional degrees of freedom in this molecule might have some affect on the results of the model. Another assumption called into question is that all trajectories are straight lines. This assumption is not valid for the lighter gases which include He, Ne, H_2 and D_2 . Therefore, this model would only seem to rigorously apply to argon, krypton and xenon.

The next test of the model is the comparison between the theoretical and experimentally determined values for C_6 . The discrepancy between these values leads one to question if the (6,12) potential can be used to accurately model the interaction between rubidium and its collision partners. Other work has shown better agreement between the theoretical and experimental values by using potentials which have additional terms such as a (6,8,12) potential (70).

Because of these questions an understanding of what physical parameters scale with the measured rates would be desirable. The rates for pressure broadening can be converted into cross-sections using $\sigma = \frac{\gamma}{\nu}$. Once the rates have been converted to cross-sections they need to further be converted into a collision probability $\frac{\sigma}{\sigma_{gk}}$ where $\sigma_{gk} = \pi(R_{Rb} + R_{gas})^2$ is the gas kinetic cross-section. R_{Rb} is the radius of the rubidium atom and is given by equation 22 and R_{gas} is the radius of the collision partner which are given in Table 9. These collision probabilities are plotted versus the dipole polarizability of the collision partner in Figures 21 and 22. As seen in these figures a correlation between the dipole polarizability and the collision probability clearly exists.

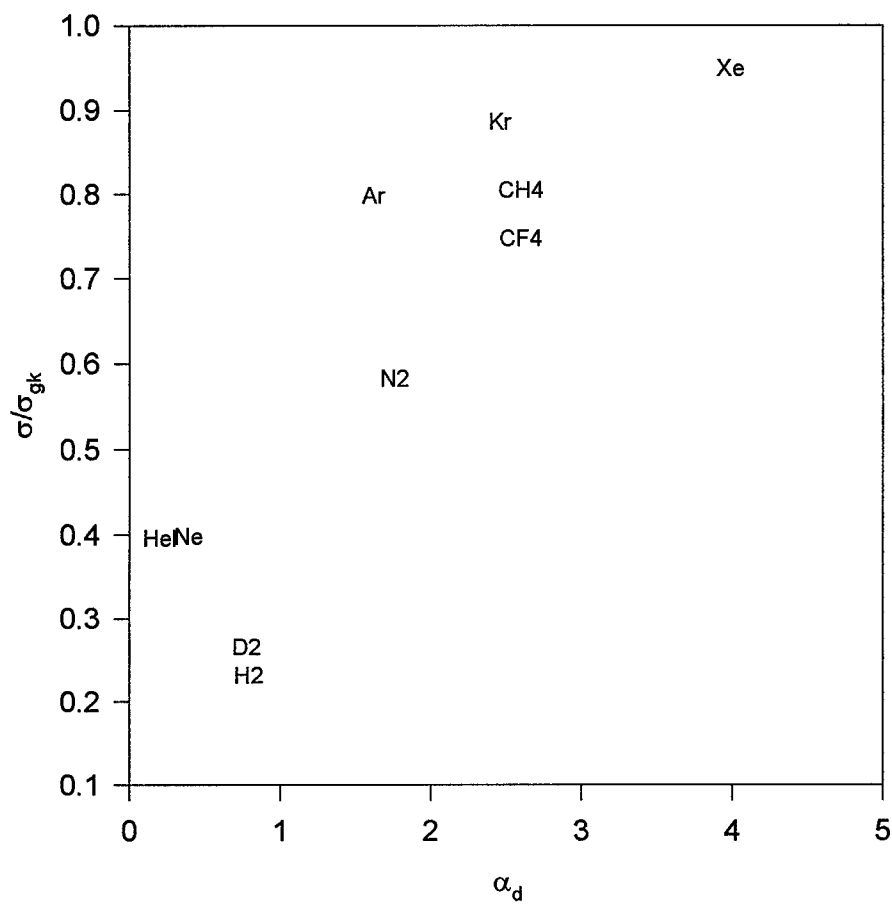


Figure 21. The interaction probability versus the dipole polarizability for the pressure broadening cross-sections for the D_1 line.

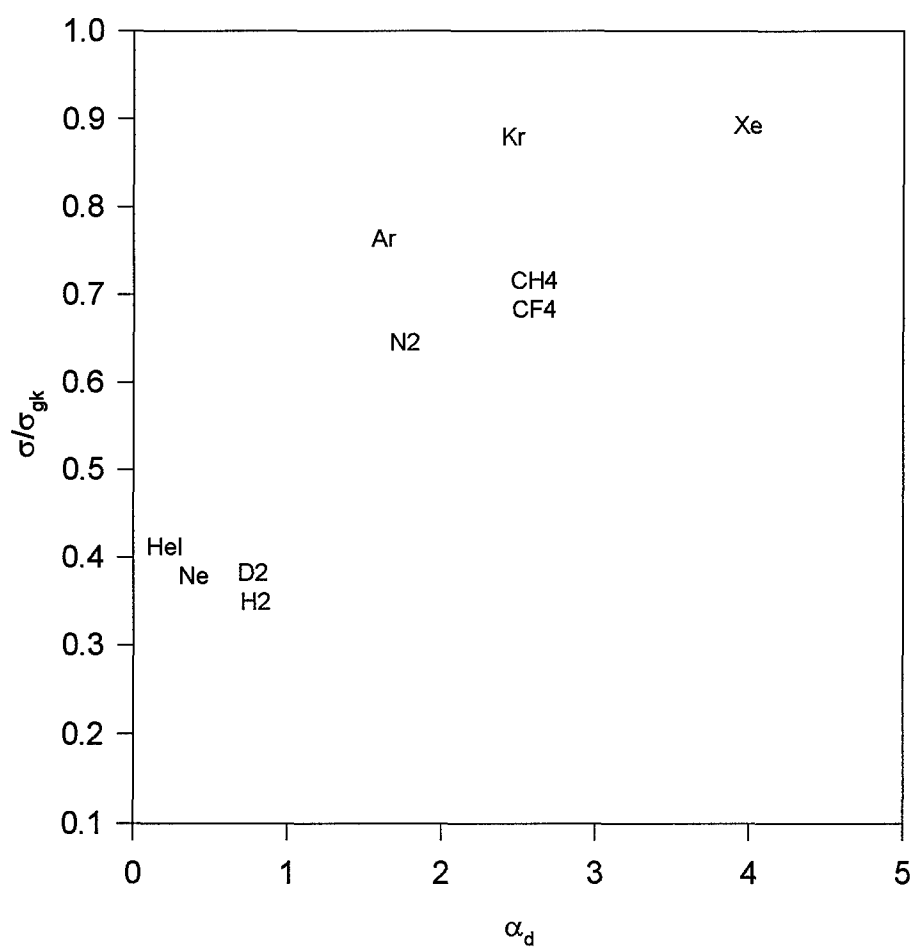


Figure 22. The interaction probability versus the dipole polarizability for the pressure broadening cross-sections for the D_2 line.

Table 9. Radius of the pressure broadening collision partners.

Reference (40)	
Gas	Radius \AA
He	2.556
Ne	2.78
Ar	3.4
Kr	3.6
Xe	4.05
H_2	2.93
D_2	2.93
N_2	3.7
CH_4	3.8
CF_4	4.7

III. Spin-Orbit and Zeeman Energy Transfer in Rubidium 5^2P Levels

3.1 Summary of collisional mixing between the 5^2P fine structure levels induced by rare gas atoms and selected molecules

The rates for energy transfer in rubidium induced by collisions with rare gas atoms was first examined by Beahn (11). Beahn used resonance fluorescence to measure the energy transfer collision cross-sections for the $P_{\frac{1}{2}} \leftrightarrow P_{\frac{3}{2}}$ of rubidium with He, Ne and Ar as shown schematically in Figure 23. Sensitized fluorescence was used to measure these cross-sections and Beahn's experimental apparatus used a filtered white light source to prepare the rubidium sample. This work established the cross-section for He collisions and bounded the cross-sections for Ne and Ar. Krause (49) continued the work by improving the measurement of the cross-sections and by adding the cross-sections for Kr, Xe and Rb collision partners. Krause improved upon Beahn's work by using a rubidium lamp as the light source and used a monochromator to select the pump frequency. This work was further improved by Gallagher (31) who extended the measurement of the collision cross-sections with rare gases to include their temperature dependence. Further work using alkali atoms as collision partners was performed by Vadla (77) who measured the energy transfer cross-sections for K and Cs. Vadla also further refined the experimental apparatus by using a laser as the pump source instead of a filtered lamp.

While these measurements were being performed Bellisio (12), who also used sensitized fluorescence, measured the fine structure collision energy transfer cross-sections induced by collisions with N_2 . Hryciyshyn (41) measured cross sections induced by collisions with H_2 , HD, D_2 , N_2 , CH_4 , CD_4 , C_2H_4 and C_2H_6 . This work was followed by Lijnse (52) who examined the cross sections for N_2 , O_2 , H_2 and H_2O . Phaneuf (66) made measurements of the cross-sections for CH_4 , CH_2D_2 and

CD_4 over the temperature range 300-650 K. Finally an additional measurement of the mixing cross-section for H_2 and N_2 was performed by Mestdagh (55).

The present work measured the energy transfer cross-sections between the $5^2P_{\frac{3}{2}}$ and the $5^2P_{\frac{1}{2}}$ levels in rubidium caused by collisions with the following collision partners: CF_4, CH_4, D_2, H_2 and N_2 .

3.2 Measurement of the fine-structure collisional mixing cross-sections

3.2.1 Collisional mixing process.

The radiative and collision processes affecting the kinetics of the 5^2P levels in rubidium are shown in figure 23. The reactions for the fine structure kinetics are listed in equations 23 through 28.

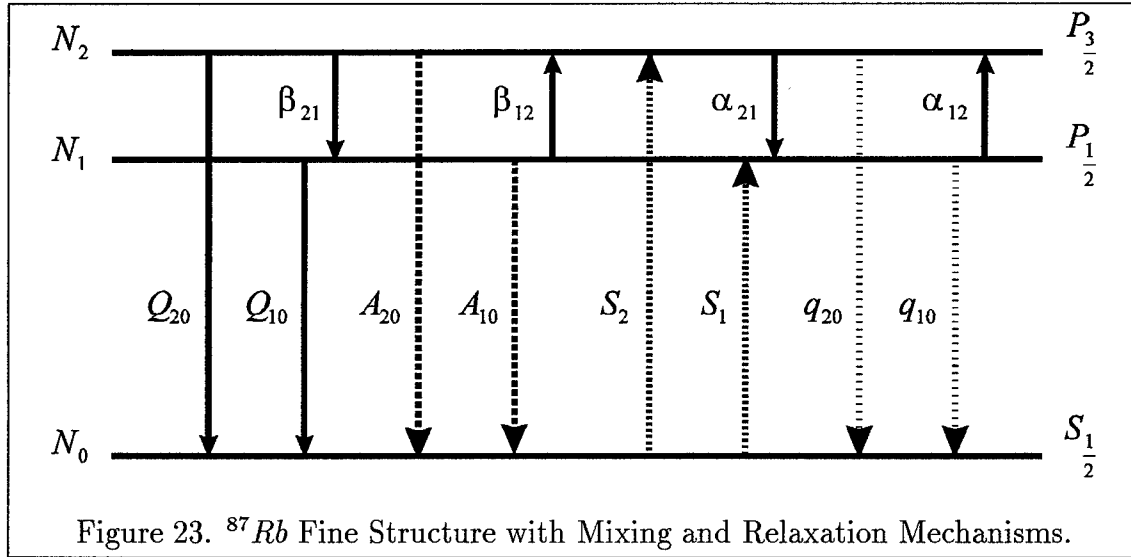


Figure 23. ^{87}Rb Fine Structure with Mixing and Relaxation Mechanisms.

Laser excitation:

$$Rb(^2S_{\frac{1}{2}}) + h\nu_{1,2} \xrightarrow{S_{1,2}} Rb(^2P_{\frac{1}{2},\frac{3}{2}}) \quad (23)$$

Spontaneous emission:

$$Rb(^2P_{\frac{1}{2},\frac{3}{2}}) \xrightarrow{A_{10}N_1, A_{20}N_2} Rb(^2S_{\frac{1}{2}}) + h\nu_{1,2} \quad (24)$$

Quenching:

$$Rb(^2P_{\frac{1}{2},\frac{3}{2}}) + Rb(^2S_{\frac{1}{2}}) \xrightarrow{q_{10,20}} Rb(^2S_{\frac{1}{2}}) + Rb(^2S_{\frac{1}{2}}) + \Delta E \quad (25)$$

$$Rb(^2P_{\frac{1}{2},\frac{3}{2}}) + X \xrightarrow{Q_{10,20}} Rb(^2S_{\frac{1}{2}}) + X + \Delta E \quad (26)$$

Spin-orbit relaxation:

$$Rb(^2P_{\frac{1}{2}}) + Rb(^2S_{\frac{1}{2}}) \xrightleftharpoons{\beta_{12,21}} Rb(^2P_{\frac{3}{2}}) + Rb(^2S_{\frac{1}{2}}) + \Delta E \quad (27)$$

$$Rb(^2P_{\frac{1}{2}}) + X \xrightleftharpoons{\alpha_{12,21}} Rb(^2P_{\frac{3}{2}}) + X + \Delta E \quad (28)$$

The rate equations for the processes shown in figure 23 are:

$$\begin{aligned} \frac{dN_1}{dt} = & S_1 + N_0N_2\beta_{21} + N_2N_g\alpha_{21} - A_{10}N_1 \\ & - N_0N_1\beta_{12} - N_1N_g\alpha_{12} - N_1N_gQ_{10} - N_0N_1q_{10} \end{aligned} \quad (29)$$

$$\begin{aligned} \frac{dN_2}{dt} = & S_2 + N_0N_1\beta_{12} + N_1N_g\alpha_{12} - A_{20}N_2 \\ & - N_0N_2\beta_{21} - N_2N_g\alpha_{21} - N_2N_gQ_{20} - N_0N_2q_{20} \end{aligned} \quad (30)$$

The terms for equations 23 through 30 are defined in table 10.

With a continuous wave laser source a steady-state condition is created such that $\frac{dN_1}{dt} = \frac{dN_2}{dt} = 0$. Under these conditions equations 29 and 30 yield:

$$S_1 + N_2[N_0\beta_{21} + N_g\alpha_{21}] = N_1[A_{10} + N_0\beta_{12} + N_g\alpha_{12} + N_gQ_{10} + N_0q_{10}] \quad (31)$$

$$S_2 + N_1[N_0\beta_{12} + N_g\alpha_{12}] = N_2[A_{20} + N_0\beta_{21} + N_g\alpha_{21} + N_gQ_{20} + N_0q_{20}]. \quad (32)$$

Table 10. Definition of terms for the fine structure collisional mixing.

Term	Description
N_0	The number density of ground state rubidium atoms
$N_{1,2}$	The number density of rubidium atoms in levels 1 and 2
N_g	The number density of buffer gas atoms/molecules
$A_{10,20}$	Einstein A coefficients for levels 1 and 2
α_{if}	Rate coefficient for collisional mixing from i to f induced by the buffer gas
β_{if}	Rate coefficient for collisional mixing from i to f induced by ground state Rubidium atoms
Q_{i0}	Rate coefficient for quenching induced by the buffer gas
q_{i0}	Rate coefficient for quenching induced by ground rubidium atoms
X	Buffer gas
ΔE	Energy released or absorbed in the reaction
$\nu_{1,2}$	Frequency of the transition

If it is assumed that the number density of rubidium atoms in the observation cell is much less than the number density of the buffer gas in the cell ($N_0 \ll N_g$), then the terms containing N_0 can be neglected leading to equations 33 and 34.

$$S_1 + N_2 N_g \alpha_{21} = N_1 [A_{10} + N_g \alpha_{12} + N_g Q_{10}] \quad (33)$$

$$S_2 + N_1 N_g \alpha_{12} = N_2 [A_{20} + N_g \alpha_{21} + N_g Q_{20}] \quad (34)$$

The excitation laser can selectively pump the $5^2P_{\frac{3}{2}}$ or the $5^2P_{\frac{1}{2}}$ level. The first case is the selective pumping of the $5^2P_{\frac{1}{2}}$ level which means that $S_1 \neq 0$ and $S_2 = 0$. Solving equation 34 under these conditions provides:

$$\frac{N_2}{N_1} = \frac{N_g \alpha_{12}}{A_{20} + N_g (\alpha_{21} + Q_{20})}. \quad (35)$$

Alternatively by selectively pumping the $5^2P_{3/2}$ level where $S_1 = 0$ and $S_2 \neq 0$ equation 33 provides:

$$\frac{N_1}{N_2} = \frac{N_g \alpha_{21}}{A_{10} + N_g(\alpha_{12} + Q_{10})}. \quad (36)$$

In the limit as $N_g \rightarrow 0$ collisional deactivation is negligible and $N_g \ll \frac{A_{20}}{\alpha_{21} + Q_{20}}$ or $N_g \ll \frac{A_{10}}{\alpha_{12} + Q_{10}}$ therefore, equations 35 and 36 can be simplified to

$$\frac{N_f}{N_i} = \frac{N_g \alpha_{if}}{A_{f0}} \quad (37)$$

where i is the initially prepared level and f is the collisionally populated level. Note, $N_g \geq 1\text{mTorr}$ and $N_0 \approx 10^{-7}\text{ Torr}$ therefore N_0 is always less than N_g . The transition rate can be written as

$$R = N_g \int_0^\infty \sigma(v) v f(v) dv \quad (38)$$

where $f(v)$ is the Maxwell velocity distribution. By making the assumption that the cross-section varies slowly with respect to speed then the rate can be reduced to $R_{if} = N_g \bar{v} \sigma_{if}$ where \bar{v} is the average velocity of the collision partner $\bar{v} = \sqrt{\frac{8kT}{\pi\mu}}$ and σ_{if} is the collisional mixing cross-section from i to f . The rate of energy exchange from equation 37 is given by $\alpha_{if} N_g = \frac{A_{f0} N_f}{N_i}$. By experimentally measuring the ratios $\frac{N_1}{N_2}$ and $\frac{N_2}{N_1}$ for the two separate cases then the rates $R_{if} = N_g \alpha_{if} = A_{f0} \frac{N_f}{N_i} = N_g \bar{v} \sigma_{if}$ can be found. Rewriting equation 37 provides the cross-section:

$$\sigma_{if} = \frac{A_{f0} N_f}{N_g \bar{v} N_i}. \quad (39)$$

3.2.2 Experimental Procedure.

The experimental apparatus for measuring the fine structure mixing cross-sections is depicted schematically in Figure 24. A Spectra-Physics 15 watt argon ion laser was used to pump a tunable Coherent 899 Ti:Sapphire ring laser. The

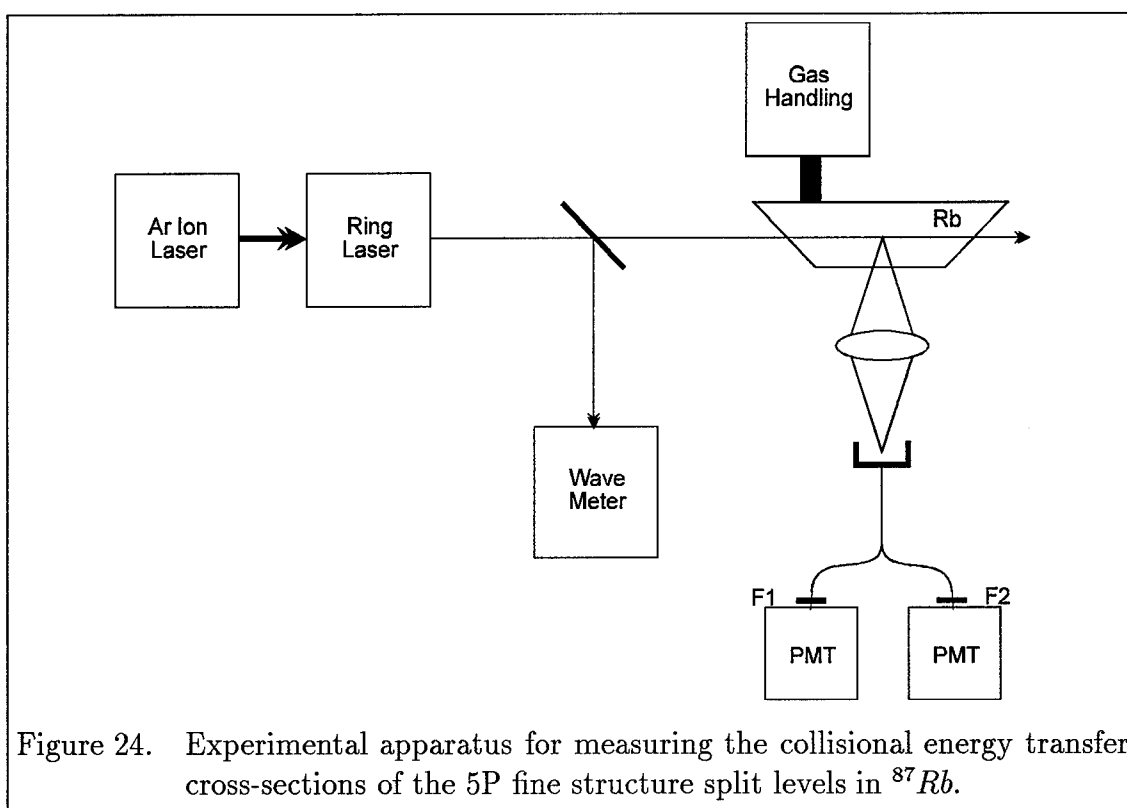


Figure 24. Experimental apparatus for measuring the collisional energy transfer cross-sections of the $5P$ fine structure split levels in ^{87}Rb .

ring laser is capable of producing a single mode beam which is frequency tunable over the range 720 to 825 nm at up to 1.5 watts continuous wave operation. The laser is reported to have a frequency stability of $\approx 500\text{kHz}$ and have a line width of $\approx 500\text{kHz}$. The ring laser's frequency was monitored by using the wave meter built into the laser head. The rubidium cell consisted of a rectangular glass fluorocell with a 1 cm and a 2 cm path length. The cell was blown onto a glass valve as was a rubidium break-seal ampul. The rubidium was 99.8 % pure with naturally occurring isotopic concentrations. The cell was attached to a vacuum system which could bring the pressure in the cell down to ≈ 1 mTorr. The gasses used were either 99.99 or 99.999 % purity gasses. The gas flow into and out of the cell was controlled by a very precise needle valve. This allowed the pressure to be controlled to a precision of 1 mTorr which was typically better than the change in pressure due to out-gassing. The laser was tuned to the $5^2P_{\frac{1}{2}}$ or the $5^2P_{\frac{3}{2}}$ line and the fluorescence from both of these lines was coupled into a fiber optic. The fiber bundle was split sending

the output through the two filters F1 and F2 where F1's line center was located at 780.2 nm with a FWHM of 1.2 nm and rejected the fluorescence from the D_1 line and F2's line center was located at 795.1 nm with a FWHM of 1.2 nm and rejected the fluorescence from the D_2 line. These filtered signals were then detected using two C31034 photo multiplier tubes (PMTs) via a photon counting system. The dark count of the PMTs were ≈ 50 counts per second. The relative signals from the two PMTs are related to the concentrations of the emitting states:

$$\frac{I_1}{I_2} = \frac{N_1 A_{10} \gamma_{F2} \gamma_{P1}}{N_2 A_{20} \gamma_{F1} \gamma_{P2}} \left(\frac{\lambda_2}{\lambda_1} \right)^3 \quad (40)$$

where γ_{F1} and γ_{F2} are corrections for the differences in transmission through the optics for each wave length, γ_{P1} and γ_{P2} are corrections for the differences in the detectivity of the two PMTs and λ_1 and λ_2 are the detected wavelengths. By using equations 35, 36, 39 and 40 the collisional mixing cross-sections were determined. Figure 25 displays typical analyzed data.

Some of the potentially difficult issues to be dealt with were as follows. A high rubidium concentration is desirable to maximize the fluorescence signal but, because of rubidium's short lifetime, 27.0 ns for the $5^2P_{1/2}$ level and 28.1 ns for the $5^2P_{3/2}$ level (53), there was a potential problem with photon trapping. To avoid the problem of self trapping the concentration of rubidium in the cell was kept at $\sim 10^{-7}$ Torr or $\sim 10^{10}$ per cm^3 . Figure 26 represents the satellite, I_s , to pump intensity, I_p , ratio as a function of rubidium concentration where the pump intensity, I_p is the optically prepared state and the satellite intensity I_s is the collisionally excited state. The rubidium concentration was determined by measuring the absorption of the laser beam as it was passed through the rubidium cell. The correct operating region is represented by the flat part of the curve which indicates a number density of $\sim 10^{10}$ per cm^3 . This is an order of magnitude lower than the concentration reported by Krause (49) to prevent self trapping. Another issue was the question of saturating the pumped transition. A calculation of the saturation intensity for

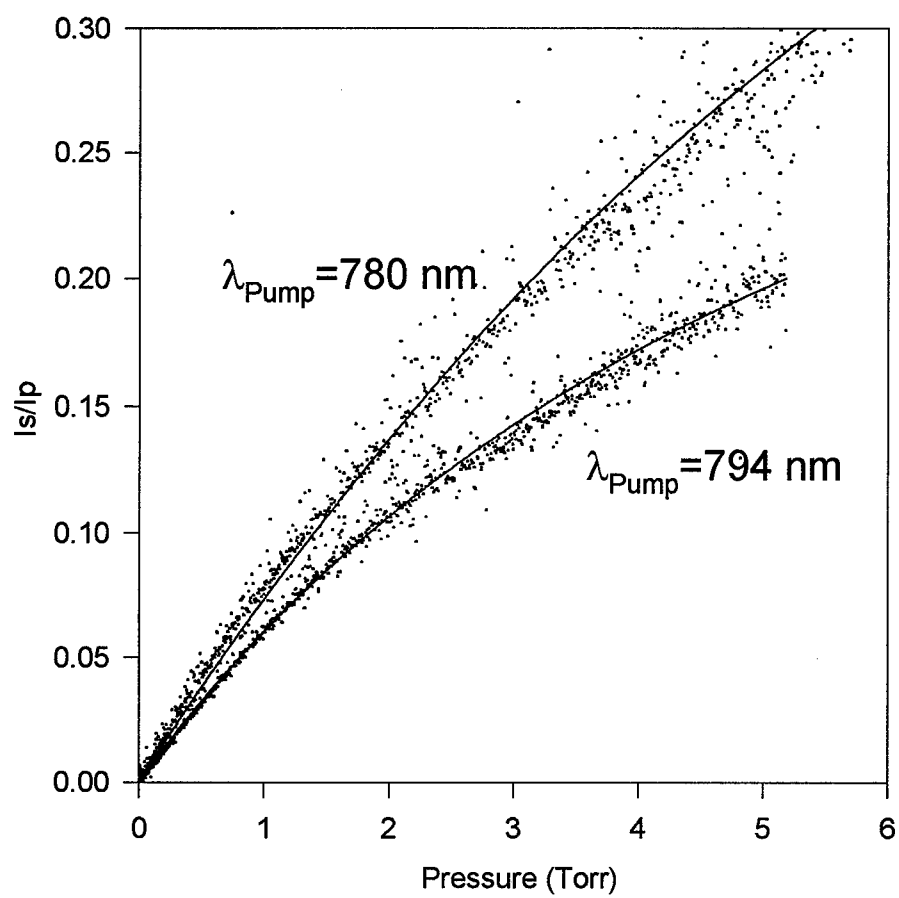


Figure 25. Spin-orbit energy transfer in ^{87}Rb induced by N_2 .

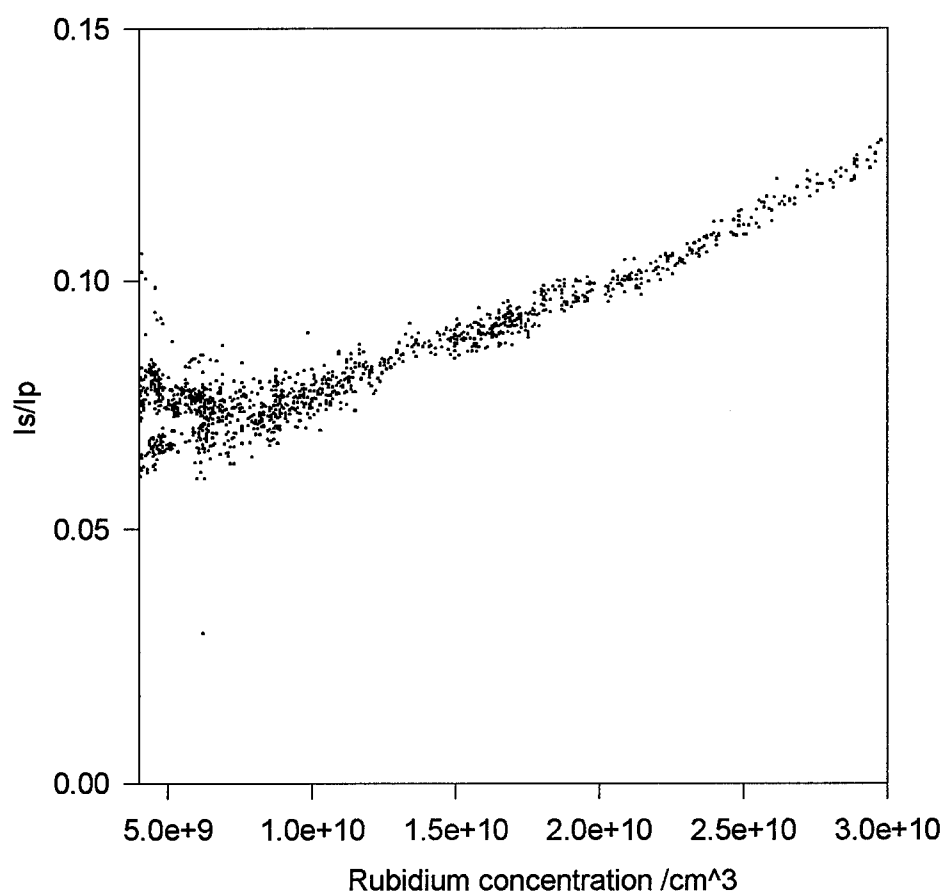


Figure 26. Satellite to pump line intensity ratio as a function of rubidium concentration.

rubidium using

$$I_s = \frac{hc4\pi}{\lambda_0^3 g(\lambda_0)}, \quad (41)$$

where $g(\lambda_0)$ is the natural line shape evaluated at line center λ_0 , yields $I_s = 4.7 \frac{mW}{cm^2}$ (82). An experimental determination of the saturation intensity is represented in Figure 27. From this data the saturation power was determined to be $0.17 \pm .02$ mW for a beam 0.2 cm in diameter. That yields a measured saturation intensity of $5.4 \pm 0.6 \frac{mW}{cm^2}$ which is in very good agreement with the expected value. The last issue was to determine how the laser intensity would affect the measured satellite to pump intensity ratio. Equations 33 and 34 were examined and noting that it is always the equation which represents the satellite level that is used to characterize the number density ratios, it was expected that a saturated transition would not have an affect on the measured ratio. This was tested by examining the measured intensity ratios as a function of laser power which is shown in Figure 28. No variation of the measured intensity ratio was observed as the laser power was changed. The points which are not on the line are artifacts from the chop mode used on the photon counters. The laser power used to measure the spin-orbit cross-sections was ≈ 0.03 mW.

3.2.3 Data analysis.

There were two systematic sources of error in the data: (1) the detection of scattered laser light and (2) the filters used to isolate the D_1 and D_2 lines allowed a few percent transmission of the unwanted line (i.e. filter F1 allowed a few percent of the D_1 line to pass through and filter F2 allowed a few percent of the D_2 line to pass through). Therefore, the detected signals contained light which should have been rejected by the filter (filter leakage). The detected intensities for the pump and satellite lines consisted of the following components. For the pump line

$$P_p = I_p + S_l \quad (42)$$

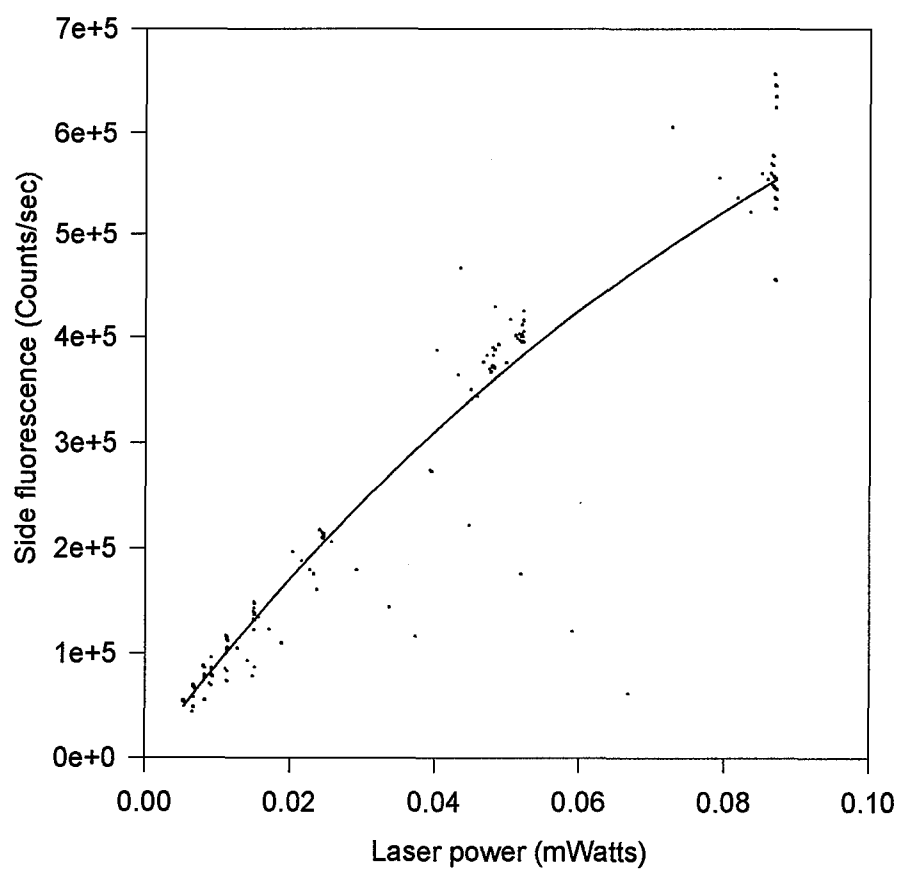


Figure 27. Total fluorescence as a function of laser power.

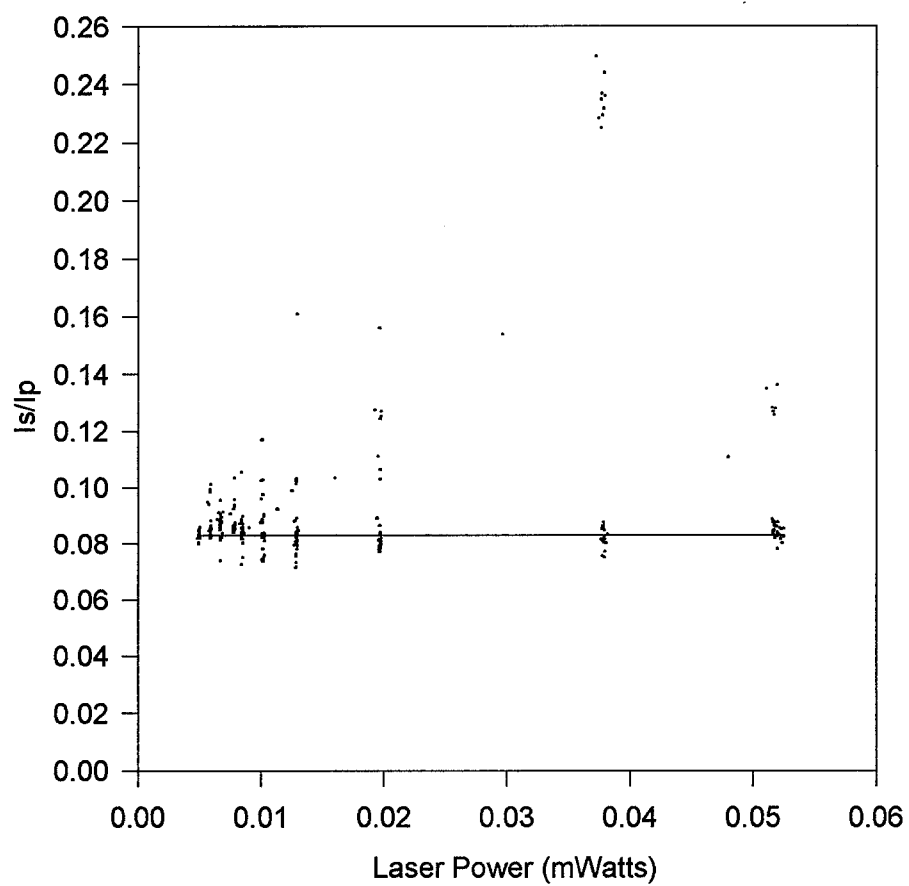


Figure 28. Satellite to pump line intensity as a function of laser power.

for the satellite line

$$P_s = I_s + \alpha P_p \quad (43)$$

where I_p is the intensity of the pump line, I_s is the intensity of the satellite line, S_l is scattered light and α is the fraction of light at the pump wavelength which passes through the filter at the satellite wavelength. The ratio of these two detected signals yields

$$\frac{P_s}{P_p} = \frac{I_s + \alpha P_p}{P_p} \quad (44)$$

where $\alpha = \frac{P_s}{P_p}$ when no collision partners are present. Once α is known a simple subtraction corrects the signal from the satellite line. This correction is shown in Figure 29.

The removal of the scatter from the pumped line could not be performed as cleanly. The correction for the laser scatter was performed by tuning the laser off resonance and characterizing the laser scatter and the laser's power. The scattered light could then be subtracted from the pumped lines signal using the following equation

$$I_p = P_p - S_l \frac{P_l}{P_{l0}} \quad (45)$$

The scattered light was weighted based on the observed laser power P_l relative to the laser power recorded when the scatter was recorded P_{l0} . This correction is illustrated in Figure 29. The inherent problems in this was the change in laser power when the laser's frequency was changed ($\approx 20\%$). With such a large change in laser power it seemed likely that the spot of the beam could physically move on the cell as the frequency of the laser was changed thus causing an additional change in the scatter. This uncertainty is the largest source of error in this data collection.

Once these corrections have been made Figure 25 represents the resulting intensity ratio. At this point the intensity needs to be converted into a number density ratio. The conversion is accomplished using equation 40. The conversion requires the relative detectivities of the two filter-PMT combinations. The relative detectivity

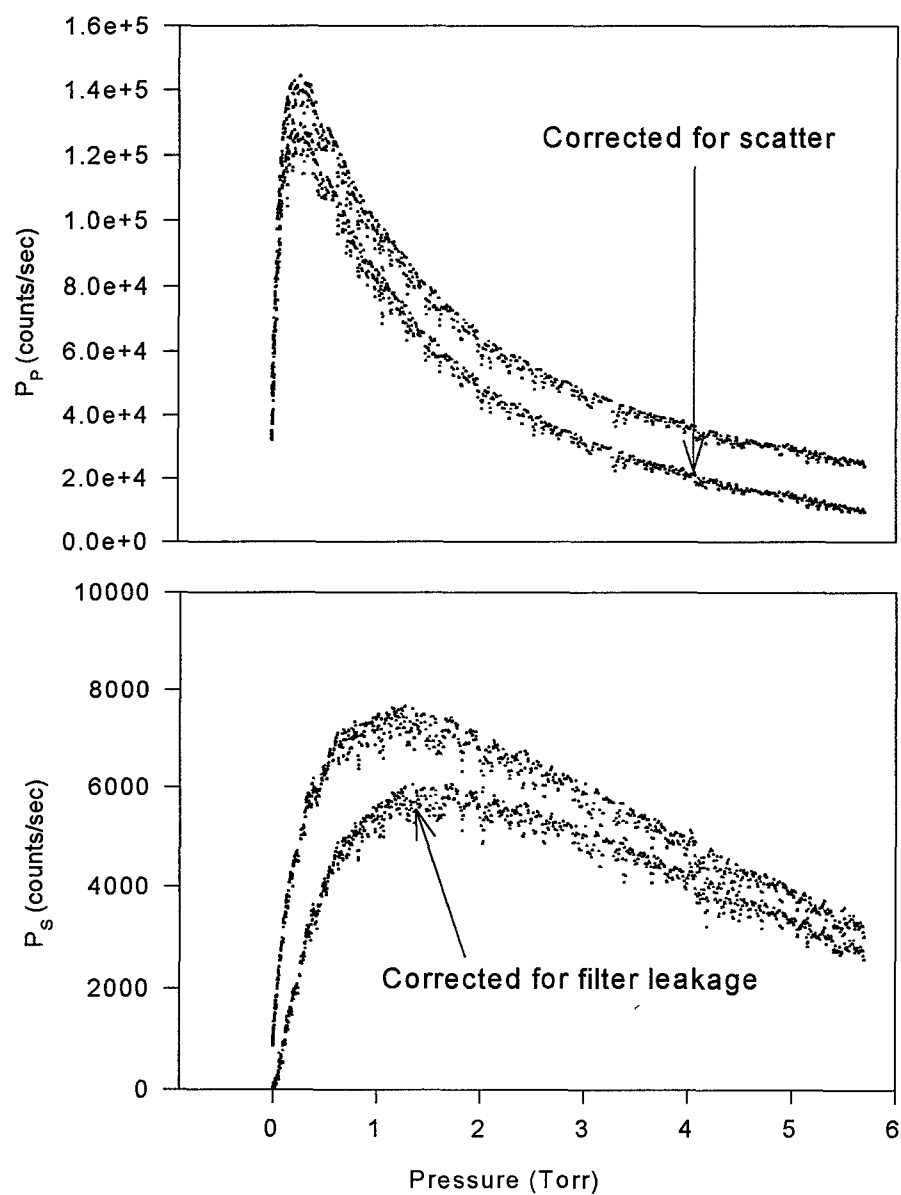


Figure 29. Spin-orbit energy transfer pump and satellite lines and the filter leakage and scattered light corrections.

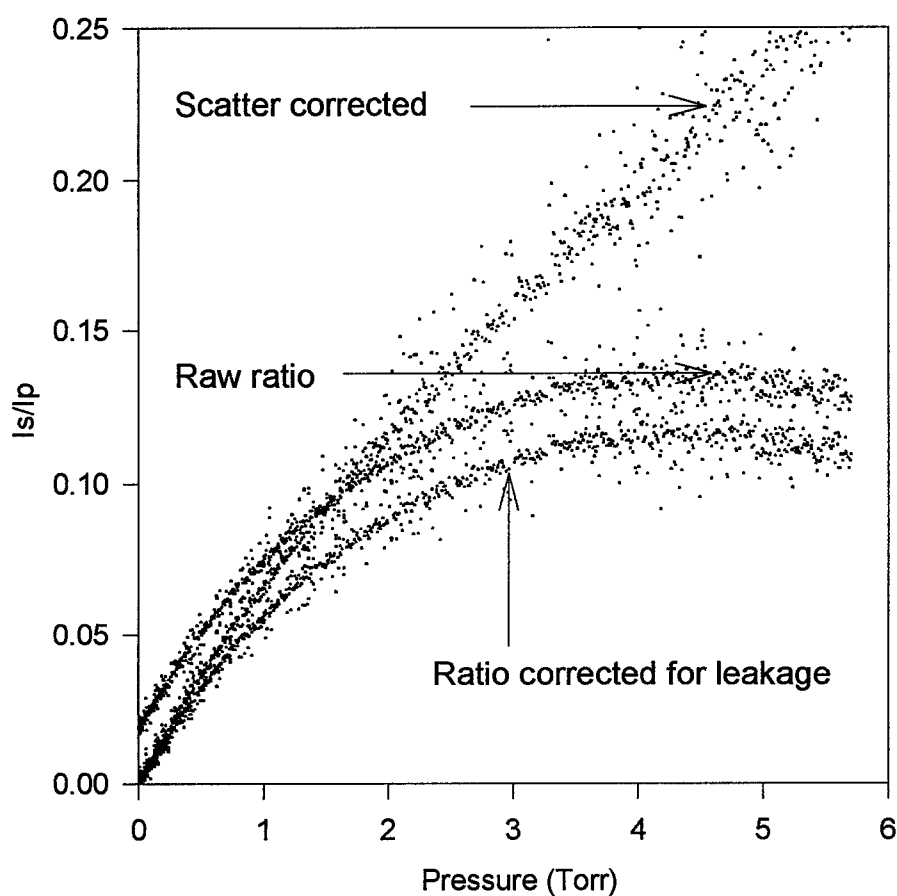


Figure 30. Satellite to pumped line ratio preparing the $5^2P_{3/2}$ level using N_2 as the collision partner with the filter leakage and scattered light correction.

was never directly measured. Rather, the intensity ratio was curve fit to $\frac{I_s}{I_p} = \frac{ap}{1+bP}$ where a and b are curve fit parameters and P is the pressure thus allowing a to be determined. Once the value for a was known for each case (preparing the $5^2P_{\frac{1}{2}}$ and the $5^2P_{\frac{3}{2}}$ levels) it was converted into a cross-section taking into account the wavelength and A coefficient corrections. These two cross-sections were then ratioed and compared to the value obtained using detailed balance thus allowing a determination of the relative detectivities. The relative detectivity measured in the manner resulted in an average value from the five measurements of 0.88 ± 0.05 .

The measured cross-sections and values from previous experiments are also listed in Table 11. Additionally, in Table 12 are listed the cross-sections for the rare gasses. These are given for comparison only. In a similar manner the quenching cross-sections can be determined. The possible variation of the quenching rate due to the scatter correction yields a large error bar.

The largest source of error in the energy transfer cross-sections is from the uncertainty in the scattered light correction. The analysis of this correction results in a 12 % uncertainty in the cross-sections. This error is much larger (approximately an order of magnitude) than the statistical error obtained from the curve fit to the data.

3.2.4 Theoretical Discussion of cross-sections.

The theories describing collisional mixing in alkali atoms deal exclusively with the mixing of the 2P fine structure split levels. The theories fall into one of two categories. The first is the theoretical description of the collision process of an alkali atom with the rare gases. The second is a description of the collisional process of an alkali atom with diatomic molecules.

Extensive theoretical work has been accomplished for the calculation of the collisional mixing cross-sections (61) (65) (69). The paper by Reid (69) reports a quantum mechanical theory for the fine structure transitions of the lowest 2P states

Table 11. Excitation transfer cross-sections for Rb induced by molecular collisions.

¹ These values were obtained from a plot of cross-section vs temperature.

Collision Partner	$^2P_{\frac{1}{2}} \rightarrow ^2P_{\frac{3}{2}}$ (σ_1) \AA^2	$^2P_{\frac{3}{2}} \rightarrow ^2P_{\frac{1}{2}}$ (σ_2) \AA^2	T $^{\circ}\text{K}$	$\frac{\sigma_1}{\sigma_2}$	$\frac{g_2}{g_1} \exp$ $(\frac{-\Delta E}{kT})$	Ref
H_2	10.0 ± 1.2	13.9 ± 1.7	330	.72	.72	This Work
	7 ± 3	-	340	-	-	(55)
	26 ± 13	-	1720	-	-	(55)
	> 50	> 30	1720	-	1.63	(52)
	11	15	340	.71	.72	(41)
D_2	21.4 ± 2.6	29.8 ± 3.6	330	.72	.72	This Work
	22	30	340	.75	.72	(41)
N_2	13.2 ± 1.6	18.4 ± 2.2	330	.72	.72	This Work
	10 ± 5	-	340	-	-	(55)
	20 ± 10	-	1720	-	-	(55)
	99 ± 20	60 ± 12	1720	1.63 ± 0.04	1.63	(52)
	16	23	340	.73	.72	(41)
	< 2	7	300	$< .29$.66	(12)
O_2	66 ± 33	40 ± 20	1720	1.63 ± 0.04	1.63	(52)
HD	18	25	340	.74	.72	(41)
H_2O	120 ± 25	73 ± 15	1720	1.63 ± 0.04	1.63	(52)
CH_4	29.5 ± 3.5	41.0 ± 5.0	330	.72	.72	This Work
	-	36^1	340	-	-	(66)
	30	42	340	.73	.72	(41)
CF_4	9.5 ± 1.1	13.2 ± 1.6	330	.72	.72	This Work
CD_4	-	36^1	340	-	-	(66)
	28	38	340	.73	.72	(41)
CH_2D_2	-	37^1	340	-	-	(66)
C_2H_4	23	32	340	.74	.72	(41)
C_2H_6	57	77	340	.74	.72	(41)

Table 12. Excitation transfer cross-sections for Rb induced by collisions with rare gas atoms and alkali metals. ¹ Theoretical values.

Collision Partner	$^2P_{\frac{1}{2}} \rightarrow ^2P_{\frac{3}{2}}$ (σ_1) \AA^2	$^2P_{\frac{3}{2}} \rightarrow ^2P_{\frac{1}{2}}$ (σ_2) \AA^2	T $^{\circ}\text{K}$	$\frac{\sigma_1}{\sigma_2}$	$\frac{g_2}{g_1} \exp$ ($\frac{-\Delta E}{kT}$)	Ref
Rb	53 ± 6	68 ± 9	340	.78	.73	(49)
Cs	$16.5 \pm 30\%$	$15 \pm 30\%$	573	1.1	1.1	(77)
K	$60 \pm 30\%$	$54 \pm 30\%$	573	1.1	1.1	(77)
He	7.2×10^{-2}	-	400	-	-	(61) ¹
	7.0×10^{-2}	10.5×10^{-2}	340	.67	.73	(31)
	$7.6 \times 10^{-2} \pm 10\%$	$10.3 \times 10^{-2} \pm 10\%$	340	.74	.73	(49)
	$.10 \pm 10\%$	$.12 \pm 10\%$	373	.83	.80	(11)
Ne	2.2×10^{-4}	-	400	-	-	(61) ¹
	1.4×10^{-3}	2.2×10^{-3}	340	.67	.73	(31)
	$1.7 \times 10^{-3} \pm 10\%$	$2.3 \times 10^{-3} \pm 10\%$	340	.74	.73	(49)
	$10^{-3} - 10^{-2}$	$10^{-3} - 10^{-2}$	373	-	.80	(11)
Ar	1.6×10^{-3}	-	400	-	-	(61) ¹
	5.1×10^{-4}	7.3×10^{-4}	340	.70	.73	(31)
	$1.0 \times 10^{-3} \pm 10\%$	$1.6 \times 10^{-3} \pm 10\%$	340	.63	.73	(49)
	$10^{-3} - 10^{-2}$	$10^{-3} - 10^{-2}$	373	-	.80	(11)
Kr	3.6×10^{-4}	4.5×10^{-4}	340	.81	.73	(31)
	$6.4 \times 10^{-4} \pm 10\%$	$1.5 \times 10^{-3} \pm 10\%$	340	.43	.73	(49)
Xe	3.4×10^{-4}	4.9×10^{-4}	340	.69	.73	(31)
	$7.9 \times 10^{-4} \pm 10\%$	$2.1 \times 10^{-3} \pm 10\%$	340	.38	.73	(49)

of an alkali atom on collision with a rare gas atom. Reid has displayed this method in the calculation of both the total and differential inelastic cross-sections for fine structure transitions between the $3^2P_{\frac{3}{2}}$ and $3^2P_{\frac{1}{2}}$ states of Na on collision with He. The method is equally applicable to other alkali and rare gas systems. The paper by Olson (61) utilized the Reid method and the pseudo-potential calculations of Baylis (8) to calculate the mixing total cross-sections for a range of alkali and rare gases. Table 12 provides the theoretical cross-sections for Rb with He, Ne and Ar.

Additional work has been accomplished on the theoretical treatment of the fine structure collisional mixing cross-sections induced by collisions with a diatomic molecule. Pascale (65) performed close-coupling quantum mechanical calculations of Rubidium's 5^2P levels in the rigid-rotor approximation for low-energy collisions ($E \leq 0.3$ ev) with H_2 and D_2 molecules lying in the ground electronic and vibrational state.

The study by Pascale concluded that two main nonadiabatic coupling mechanisms are in competition for inducing fine structure transitions. There are radial coupling terms which result from spin orbit decoupling during the collision which are located at short ($R \leq 8a.u.$) and intermediate ($R \simeq 12 - 15a.u.$) distances. The study by Pascale also shows that the rotational levels of the molecule play an important role during the collision for D_2 as well as for H_2 . In particular, it was shown that close-coupling calculations including the rotational levels of H_2 and D_2 are necessary for correctly interpreting the crossed-beam measurements of Cuvellier (25).

3.3 Collisional mixing between the 5^2P Zeeman split levels induced by rare gas atoms and selected molecules

The present work examined the energy transfer cross-sections among the Zeeman split levels of rubidium. Figure 31 illustrates the splitting of the 5^2S and 5^2P levels in the presence of a strong applied magnetic field, where B_0 is the applied magnetic field, μ_B is the Bohr magneton and g_j is the electronic gyromagnetic fac-

tor. The line splitting is explained in greater detail later in the chapter. It is the energy transfer between these Zeeman split levels which has been observed.

The only previous work on the collisional mixing cross-sections in rubidium was performed by Kedzierski (46). He examined the cross-sections for the 6^2P levels in ^{87}Rb using He, Ne and Ar as collision partners. While there is no other Zeeman energy transfer work done in rubidium another closely related topic is the measurement of the disorientation and disalignment cross-sections. These cross-sections are a characterization of the depolarization due to collisions with inert gases. This topic has been extensively studied and is summarized in reference (9). The disorientation and disalignment cross-sections can be transformed into a reduced set of Zeeman energy transfer cross-sections by making two assumptions about the relationships between Zeeman cross-sections. These assumptions are presented later in this chapter and have been tested for validity using the Zeeman energy transfer cross-sections with nitrogen as the buffer gas.

3.4 *Experimental determination of the Zeeman structure collisional mixing cross-sections*

3.4.1 *Theoretical description of the hyperfine and Zeeman Splitting induced by an applied magnetic field.*

The theoretical description of the Zeeman structure in alkali atoms has been extensively explored(48). The theories take into account the magnetic moments from the electron spin, the electrons orbital angular momentum and the nuclear spin coupled to an applied magnetic field. For the $S_{\frac{1}{2}}$ and $P_{\frac{1}{2}}$ ($J = \frac{1}{2}$) levels an expression for the splitting with an applied magnetic field can be found (48). The good quantum number for representing the Zeeman split energy levels is $m = m_J + m_I$. For $m = \pm(J + I)$,

$$E_H = \frac{A}{2}I \pm \frac{1}{2}g_J\mu_B H_0 \mp Ig_I\mu_B H_0 \quad (46)$$

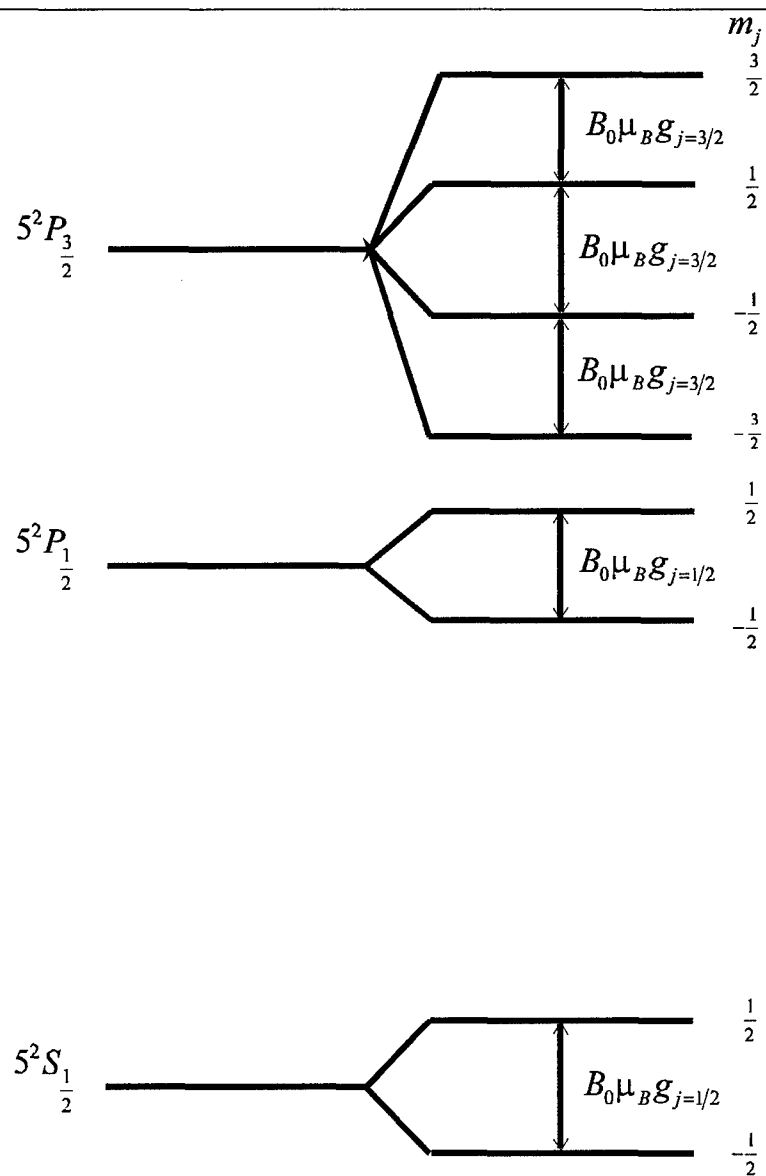


Figure 31. ^{87}Rb Zeeman split levels in the high field limit.

and for $m = J + I - 1, J + I - 2, \dots, 1 - (J + I)$

$$E_H = -\frac{A}{4} - mg_I\mu_B H_0 \pm \frac{1}{2} \sqrt{A^2(I + \frac{1}{2})^2 + 2Am(g_J - g_I)\mu_B H_0 + (g_J - g_I)^2 \mu_B^2 H_0^2} \quad (47)$$

Equations 46 and 47 are plotted as a function of magnetic field in Figures 32 and 33, respectively.

Table 13. Term definitions for the Zeeman energy shifts.

Term	Description
E_H	Energy shift in the presence of a magnetic field
A	Coefficient for hyperfine splitting
I	Nuclear spin
g_J	Electronic gyromagnetic factor
g_I	Nuclear gyromagnetic factor
$\mu_B = \frac{e\hbar}{2m_e}$	Bohr magneton $14.8 \frac{GHz}{Tesla}$
H_0	Applied magnetic field

Figure 34 provides the spectrum of the $5^2P_{\frac{1}{2}}, m_j = \frac{1}{2} \rightarrow 5^2S_{\frac{1}{2}}, m_j = \frac{1}{2}$ transition obtained using saturation spectroscopy. The structure is described in the expanded region in Figure 32. A schematic diagram of the experimental apparatus used to perform the saturation spectroscopy is shown in Figure 35. A Spectra-Physics 15 watt argon ion laser was used to pump a tunable Coherent 899 Ti:Sapphire ring laser. The ring laser is capable of producing a single mode beam which is frequency tunable over the range 720 to 825 nm at up to 1.5 watts continuous wave operation. The laser is reported to have a frequency stability of $\approx 500 kHz$ and have a line width of $\approx 500 kHz$. The laser's line width is approximately an order of magnitude smaller than the natural line width of rubidium. The ring laser's frequency was monitored by using the wave meter built into the laser head. The beam from the ring laser was split into two components and each component was chopped at different frequencies ω_1 and ω_2 using the inside and outside chopper on a single chopper wheel. The two beams were then routed through the rubidium cell in opposite directions. The beams

needed to be aligned very precisely for the apparatus to work. The rubidium cell consisted of a rectangular glass fluorocell with a 1 cm and a 2 cm path length. The cell was blown onto a glass valve as was a rubidium break-seal ampul. The rubidium was 99.8 % pure with naturally occurring isotopic concentrations. The side fluorescence from the cell was then coupled into a photon multiplier tube which provided the signal to the lock-in amplifier. The lock-in amplifier detected the sum frequency $\omega = \omega_1 + \omega_2$ thus yielding a sub-Doppler spectrum. A more complete explanation of this technique can be found in reference (26). A value of 106 ± 35 for the isotope shift was obtained from this spectrum. The spectrum was analyzed by comparing the observed spectrum to the predicted line positions from equations 46 and 47 for the two isotopes. The isotope shift is compared to previously measured values in Table 14.

Table 14. The isotope shift between ^{87}Rb and ^{85}Rb .

Isotope Shift	Reference
106 ± 35	Sat Spec
88 ± 2	Absorption
77 ± 3	(32)
77.7 ± 2.1	(10)
105 ± 15	(27)

The solution for the Zeeman splitting of the $P_{\frac{3}{2}}$ level is not as straight forward. To accurately represent this level an additional interaction energy term must be added to the Hamiltonian. This term represents the affect on the electron caused by taking into account the spatial extent of the nucleus (i.e. not treating the nucleus as a point charge). The mathematical treatment of this interaction leads to an expansion of the interaction energy where the first contributing term is the electric quadrupole term. Therefore, the quadrupole moment must be taken into account to accurately represent the energy shifts in the $5^2P_{\frac{3}{2}}$ level.

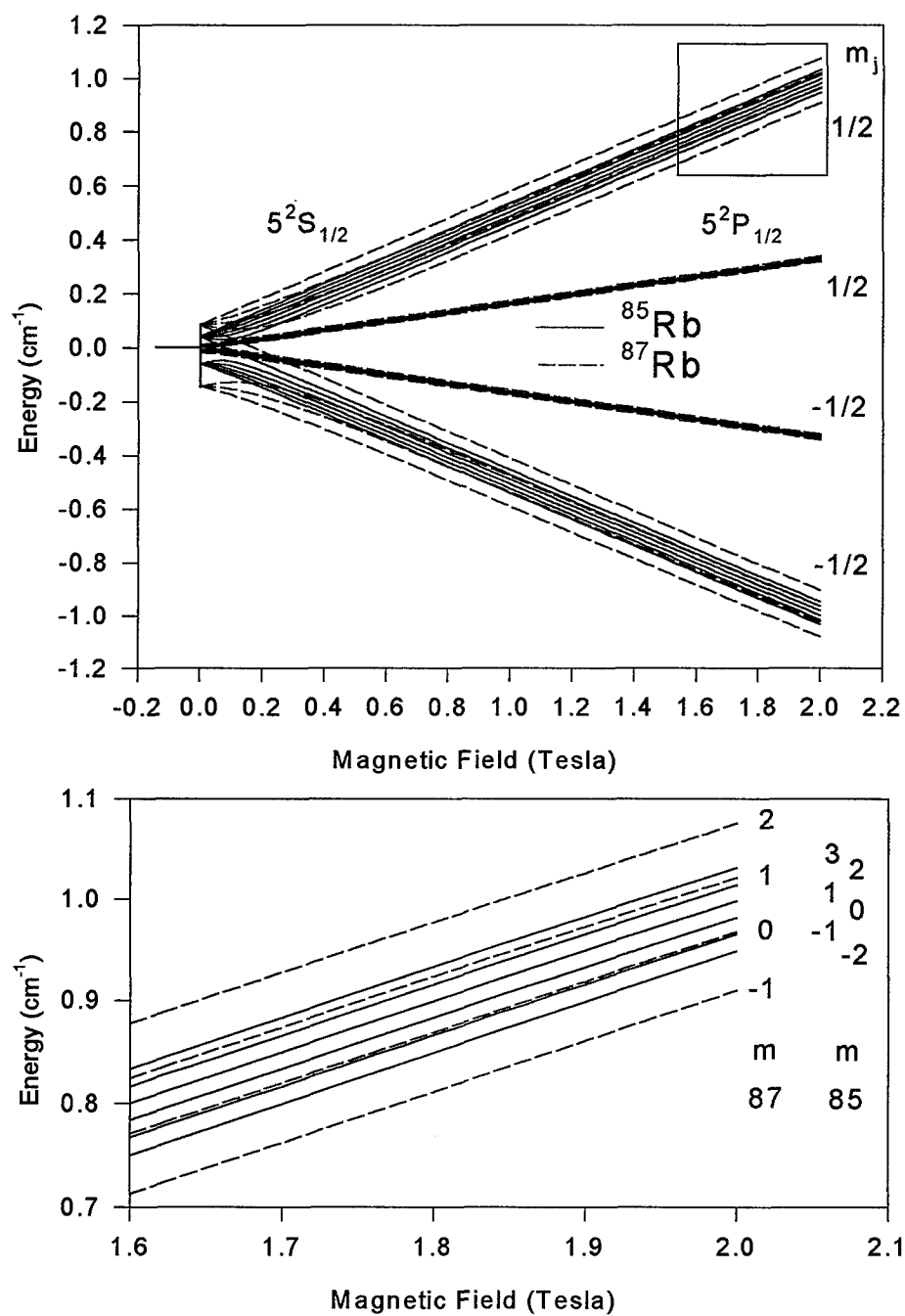


Figure 32. Hyperfine and Zeeman structure energy shifts with respect to zero for the $5^2S_{1/2}$ and the $5^2P_{1/2}$ level.

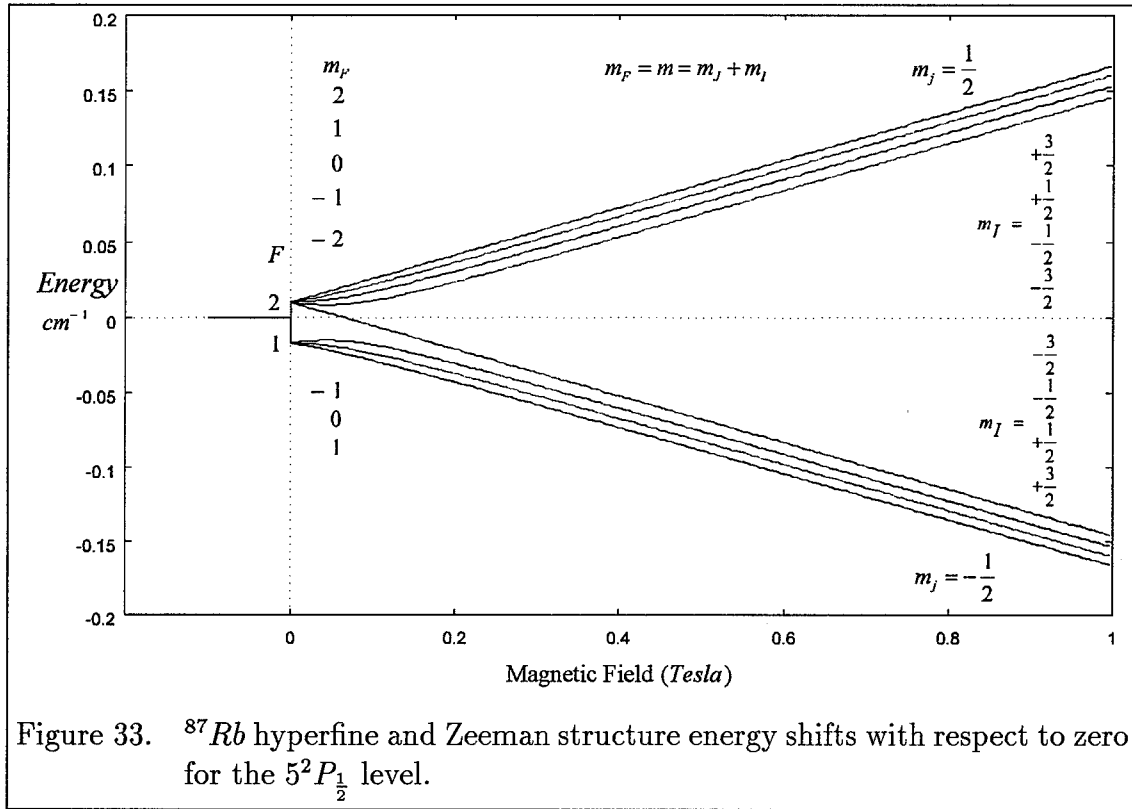


Figure 33. ^{87}Rb hyperfine and Zeeman structure energy shifts with respect to zero for the $5^2P_{\frac{1}{2}}$ level.

Because of this additional term there is no analytic solution that spans from the low magnetic field limit to the high magnetic field limit. Therefore, the Zeeman energy levels are represented in the low and the high magnetic field limits. The energy shift for the $5^2P_{\frac{3}{2}}$ is given by the following equation

$$E_{P_{\frac{3}{2}}} = E_{HF} + E_Q + E_B \quad (48)$$

where E_{HF} is the hyperfine energy shift, E_Q is the quadrupole energy shift and E_B is the energy shift induced by the applied magnetic field. Examining the weak magnetic field limit first, the hyperfine split energy term is

$$E_{HF} = \frac{AC}{2} \quad (49)$$

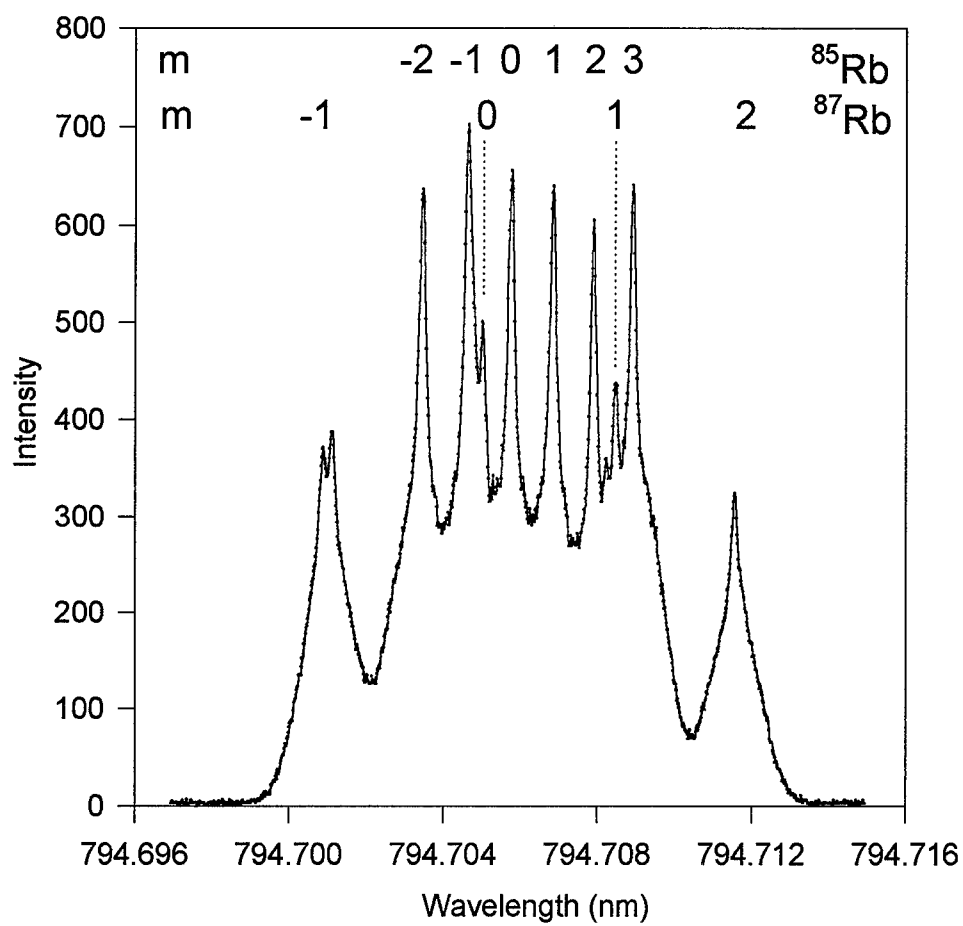
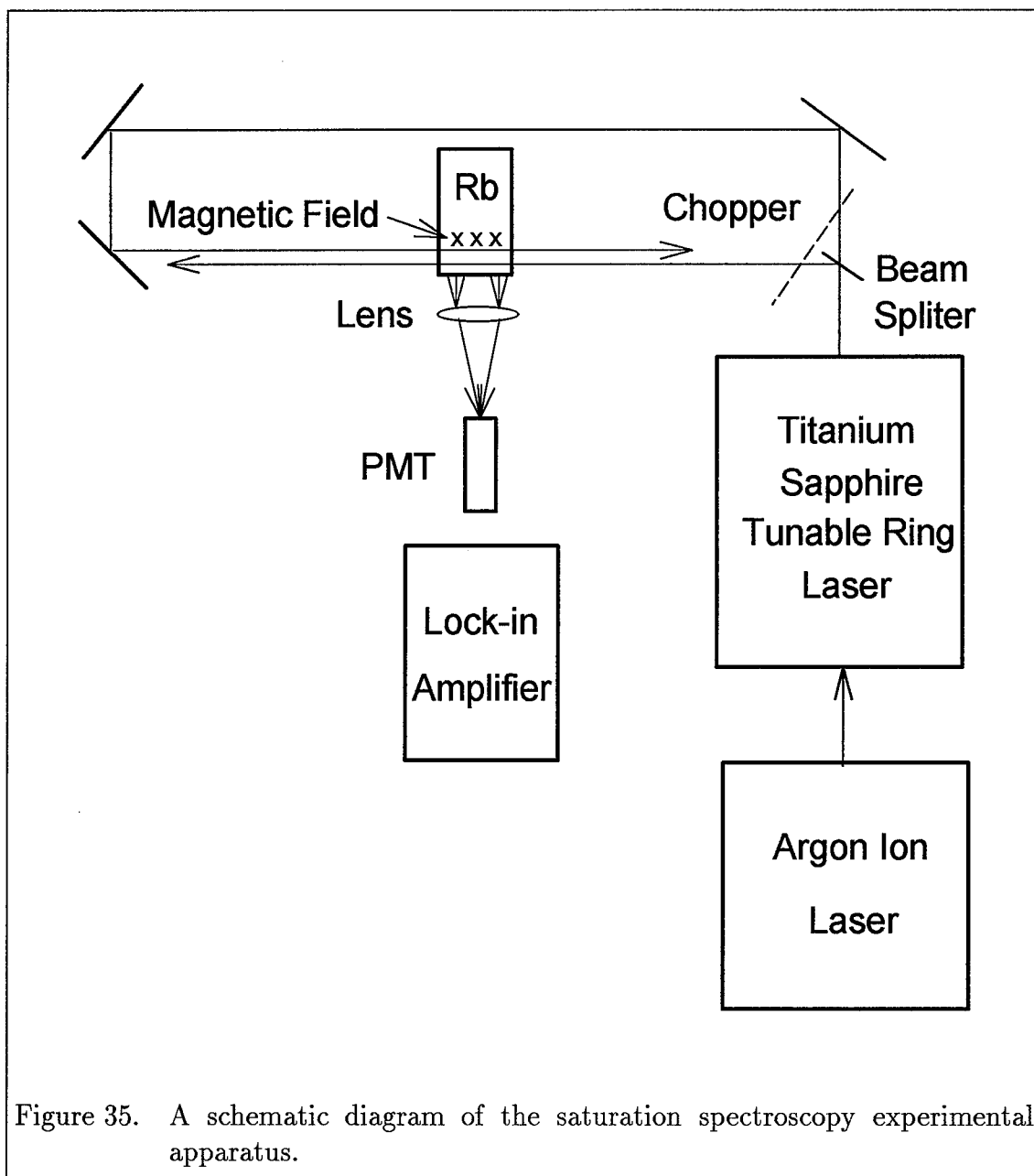


Figure 34. Saturation spectrum of the $5^2P_{\frac{1}{2}}, m_j = \frac{1}{2} \rightarrow 5^2S_{\frac{1}{2}}$ transition at 1 Tesla. The labels represent the Zeeman structure of the ground state.



where A is the hyperfine coupling constant. The quadrupole interaction energy shifts are given by

$$E_Q = B \frac{\frac{3}{4}C(C+1) - I(I+1)J(J+1)}{2J(2J-1)I(2I-1)} \quad (50)$$

where $C = F(F+1) - I(I+1) - J(J+1)$, $F = I+J, I+J-1, \dots |I-J|$ and B is the quadrupole coupling constant. Finally the energy shift induced by the applied magnetic field is given by

$$E_B = \mu_B H_0 m_F \left[g_J \frac{F(F+1) + J(J+1) - I(I+1)}{2F(F+1)} - g_I \frac{F(F+1) + I(I+1) - J(J+1)}{2F(F+1)} \right]. \quad (51)$$

The weak field limit is shown in Figure 36 using the values given in Table 15.

Table 15. Rubidium constants ¹ Theoretical value.

⁸⁷ Rb	$P_{\frac{3}{2}}$	$P_{\frac{1}{2}}$	$S_{\frac{1}{2}}$
A MHz	84.845(55) ⁽⁵⁾	406.2(8) ⁽⁵⁾	3417.34130642(15) ⁽⁵⁾
B MHz	12.52(9) ⁽⁵⁾	-	-
g_J	1.3362(13) ⁽⁵⁾	$\frac{2}{3}^1$	2.00233113(20) ⁽⁵⁾
Nuclear		gyromagnetic constant	
g_I		-0.0009951414(10) ⁽⁵⁾	

⁸⁵ Rb	$P_{\frac{3}{2}}$	$P_{\frac{1}{2}}$	$S_{\frac{1}{2}}$
A MHz	25.009(22) ⁽⁵⁾	120.72(25) ⁽⁵⁾	1011.910813(2) ⁽⁵⁾
B MHz	25.88(3) ⁽⁵⁾	-	-
g_J	1.3362(13) ⁽⁵⁾	$\frac{2}{3}^1$	2.00233113(20) ⁽⁵⁾
Nuclear		gyromagnetic constant	
g_I		-0.0002936400(6) ⁽⁵⁾	

In the strong magnetic field limit the hyperfine split energy levels are given by

$$E_{HF} = A m_I m_J. \quad (52)$$

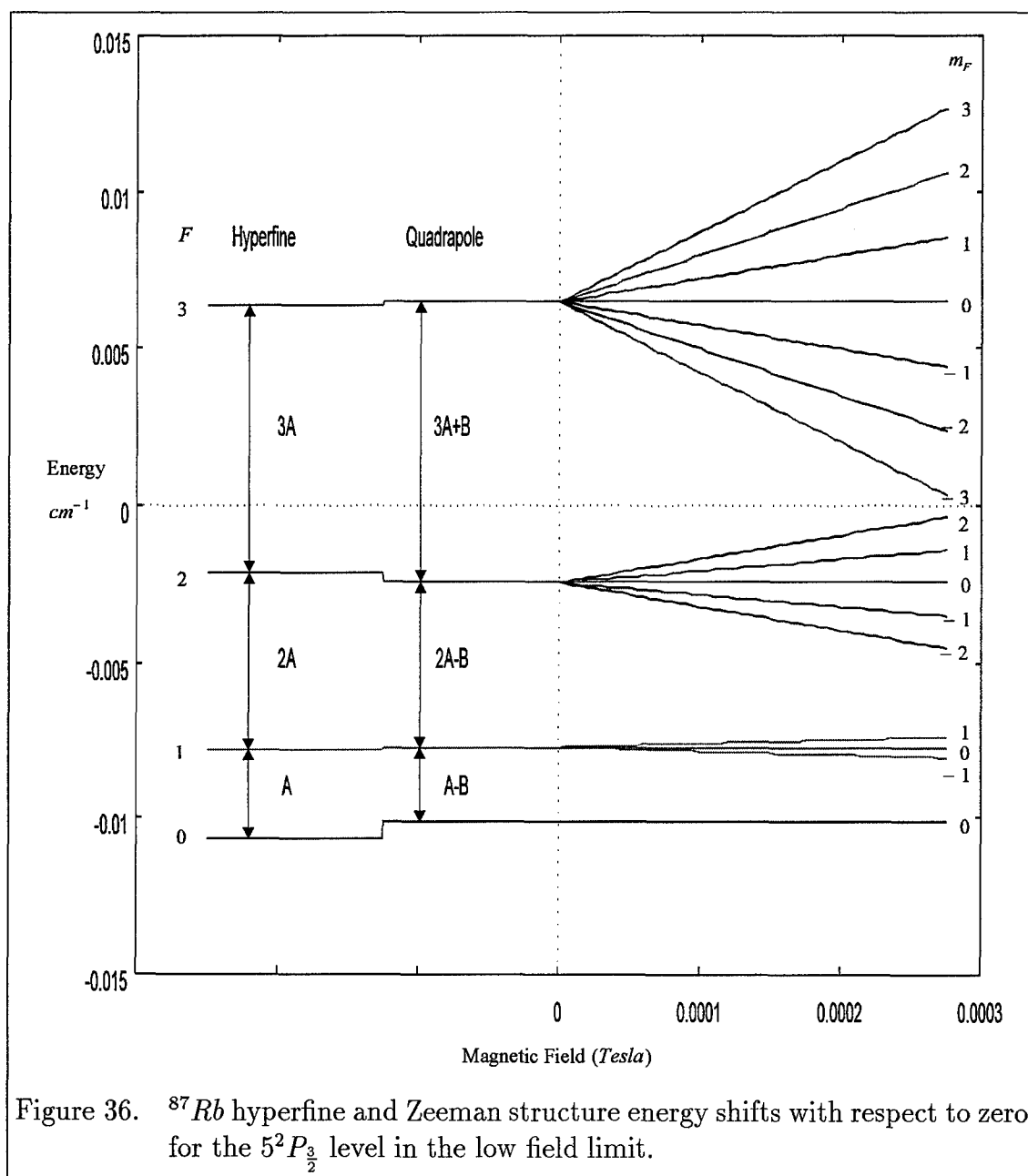


Figure 36. ^{87}Rb hyperfine and Zeeman structure energy shifts with respect to zero for the $5^2P_{3/2}$ level in the low field limit.

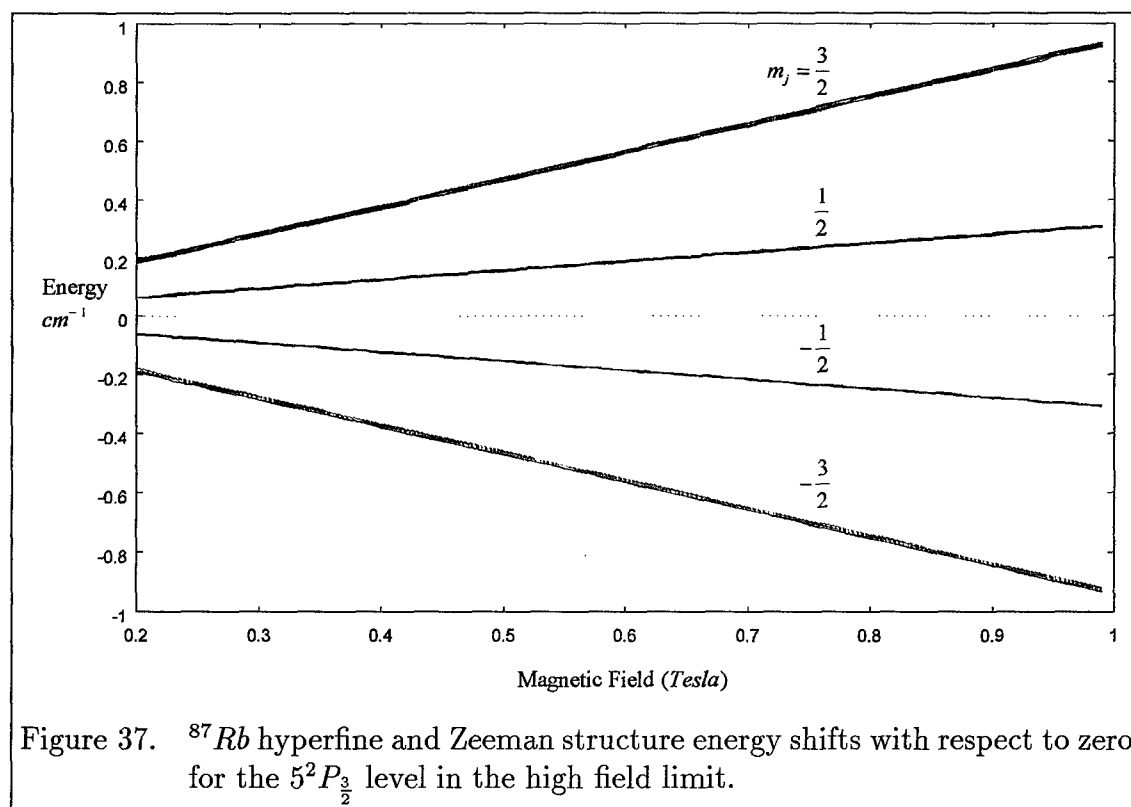
The quadrupole contribution is given by

$$E_Q = \frac{B}{4} \frac{3m_J^2 - J(J+1)}{J(2J-1)} \frac{3m_I^2 - I(I+1)}{I(2I-1)} \quad (53)$$

and the contribution to the energy shifts induced by the magnetic field is given by

$$E_B = \mu_B H_0 (m_J g_J - m_I g_I). \quad (54)$$

The strong field limit is shown in Figure 37 using the values given in Table 15. If the quadrupole term is neglected then a solution for arbitrary values of J can be found in reference (35).



3.4.2 Zeeman structure collisional mixing process.

This study was specifically interested in the high field limit case. The Zeeman structure collisional mixing process with selective excitation to the $5^2P_{\frac{1}{2}} \ m_j = -\frac{1}{2}$ level is depicted in Figure 38. The coupled set of rate equations for this system is given by equation 55 and the terms are defined in Table 16.

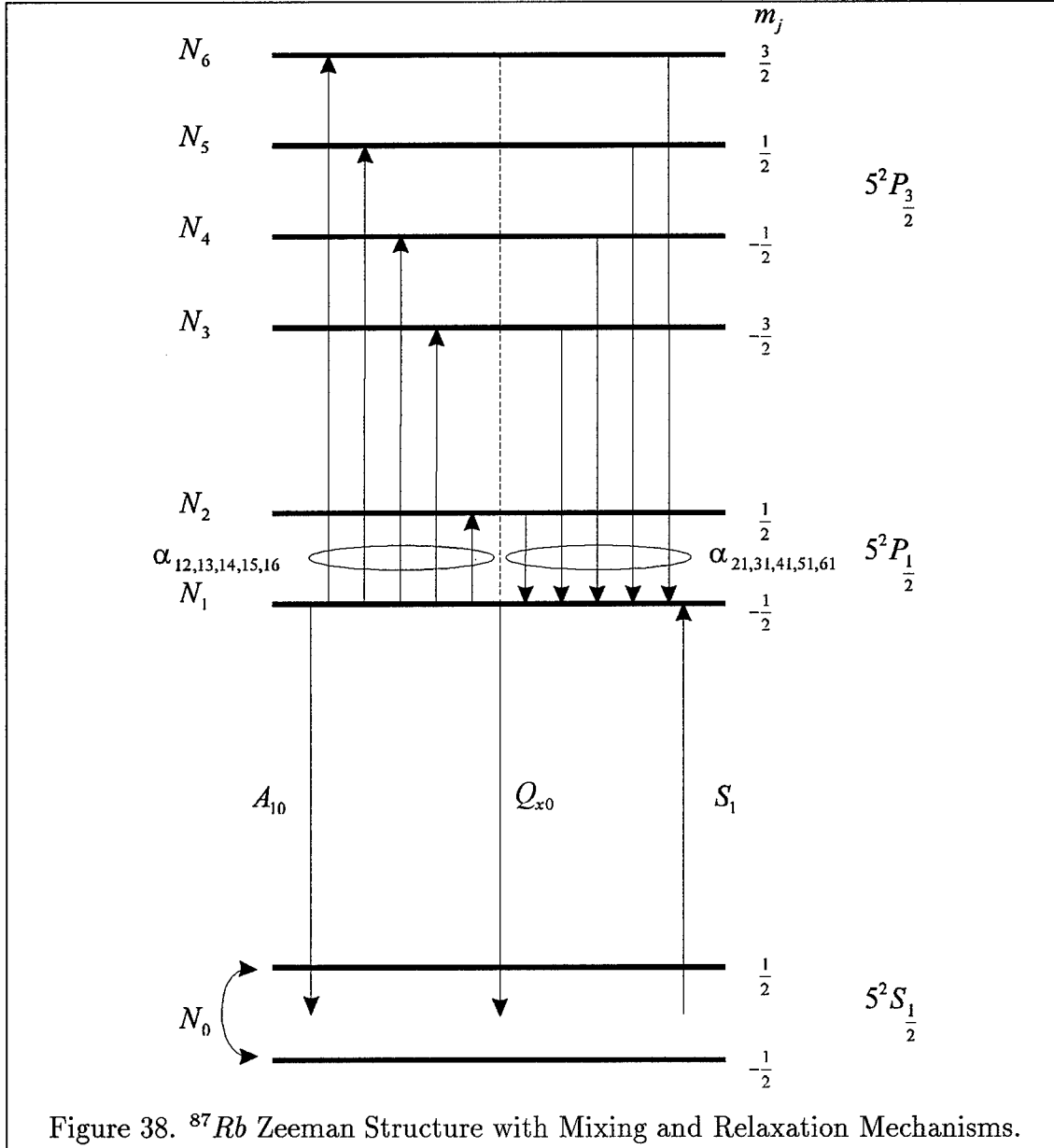


Figure 38. ^{87}Rb Zeeman Structure with Mixing and Relaxation Mechanisms.

$$\frac{dN_q}{dt} = S_q - A_{q0}N_q - Q_{q0}N_qN_g - N_gN_q \sum_{p=1}^6 \sum_{p \neq q} \alpha_{qp} + N_g \sum_{p=1}^6 \sum_{p \neq q} \alpha_{pq}N_p \quad (55)$$

Table 16. Definition of terms for the Zeeman split collisional mixing.

Term	Description
N_x	The number density of rubidium atoms in level $x=1,2,\dots,6$
N_g	The number density of buffer gas atoms/molecules
A_{x0}	Einstein A coefficients for level $x=1,2,\dots,6$
$\alpha_{p,q}$	Rate coefficient for collisional mixing from the q to p level induced by the buffer gas
Q_{x0}	Rate coefficient for quenching of level $x=1,2,\dots,6$ induced by the buffer gas

Using a tunable narrow line-width laser allows the selective population of individual levels. Assuming that only one level is pumped such that $S_k \neq 0$ and $S_q = 0$ where k is the index of the pumped level and by using a continuous wave laser to achieve steady state conditions, $\frac{dN_q}{dt} = 0$, then for all of the satellite levels equation 55 can be simplified to

$$0 = -A_{q0}N_q - Q_{q0}N_qN_g - N_gN_q \sum_{p=1}^6 \sum_{p \neq q} \alpha_{qp} + N_g \sum_{p=1}^6 \sum_{p \neq q} \alpha_{pq}N_p \quad (56)$$

Solving equation 56 for N_q and explicitly separating the initially prepared state from the summation yields

$$N_q = \frac{N_gN_k\alpha_{kq} + N_g \sum_{p \neq q,k} \alpha_{pq} \frac{N_p}{N_q}}{A_{q0} + N_g(Q_{q0} + \sum_{p \neq q} \alpha_{qp})}. \quad (57)$$

Dividing through by N_k and factoring yields

$$\frac{N_q}{N_k} \left[1 - \frac{N_g \sum_{p \neq q,k} \alpha_{pq} \frac{N_p}{N_q}}{A_{q0} + N_g[Q_{q0} + \sum_{p \neq q} \alpha_{qp}]} \right] = \frac{N_g\alpha_{kq} \frac{N_p}{N_q}}{A_{q0} + N_g[Q_{q0} + \sum_{p \neq q} \alpha_{qp}]}. \quad (58)$$

This expression can further be simplified to

$$\frac{N_q}{N_k} = \frac{N_g \alpha_{kq}}{A_{q0} + N_g [Q_{q0} + \sum_{p \neq q} \alpha_{qp} - \sum_{p \neq q, k} \alpha_{pq} \frac{N_p}{N_q}]}. \quad (59)$$

The rate of energy transfer is given by $R_{kq} = N_g \bar{v} \sigma_{kq} = N_g \alpha_{kq}$ which reduces to $\sigma_{kq} = \frac{\alpha_{kq}}{\bar{v}}$ for the cross-section.

This formalism leads to 30 mixing cross-sections. By using the detailed balance principle

$$\sigma_{pq} = \sigma_{qp} \exp\left(\frac{E_p - E_q}{kT}\right) \quad (60)$$

the number of independent cross-sections can be cut in half. The energy gap $E_p - E_q \ll kT$ such that $\sigma_{pq} = \sigma_{qp}$. Note, the degeneracy for each of the six levels is four for ^{87}Rb and six for ^{85}Rb . The number of cross-sections can further be reduced by applying the following relations:

$$\sigma(J, m \leftrightarrow J, m') = \sigma(J, -m \leftrightarrow J, -m') \quad (75) \quad (61)$$

$$\sigma(J, m \rightarrow J', m) = \sigma(J, -m \rightarrow J', -m) \quad (46) \quad (62)$$

Throughout the literature search no validation for these relations could be found. Equation 61 is an assumption made which allows the Zeeman energy transfer cross-sections to be reduced to a set of four cross-sections, the disorientation and disalignment cross-sections. Equation 62 is a symmetry argument justified by the very small energy spacing, $\ll kT$, between Zeeman split levels. These relationships have apparently not been tested for validity with rubidium and no validation for these relationships has been found for the other alkali metal.

3.4.3 Experimental procedure.

The measurement of the mixing cross-sections for the Zeeman split levels was handled in a similar manner to the fine structure split lines except it was not possible

to monitor both the pumped line and all of the collisionally mixed levels simultaneously. Instead, a $1\frac{1}{3}$ meter monochromator was used to scan through the lines and the signal was detected by a PMT. The magnetic field was provided by a Lake Shore magnet using a model 647 and 637 power supplies. The magnet's poles were 1 inch in diameter and the separation was 2 cm. The magnet was maintained at a current of 80 amps which resulted in a field strength of 2 Tesla. A schematic diagram of the experimental apparatus is shown in Figure 39.

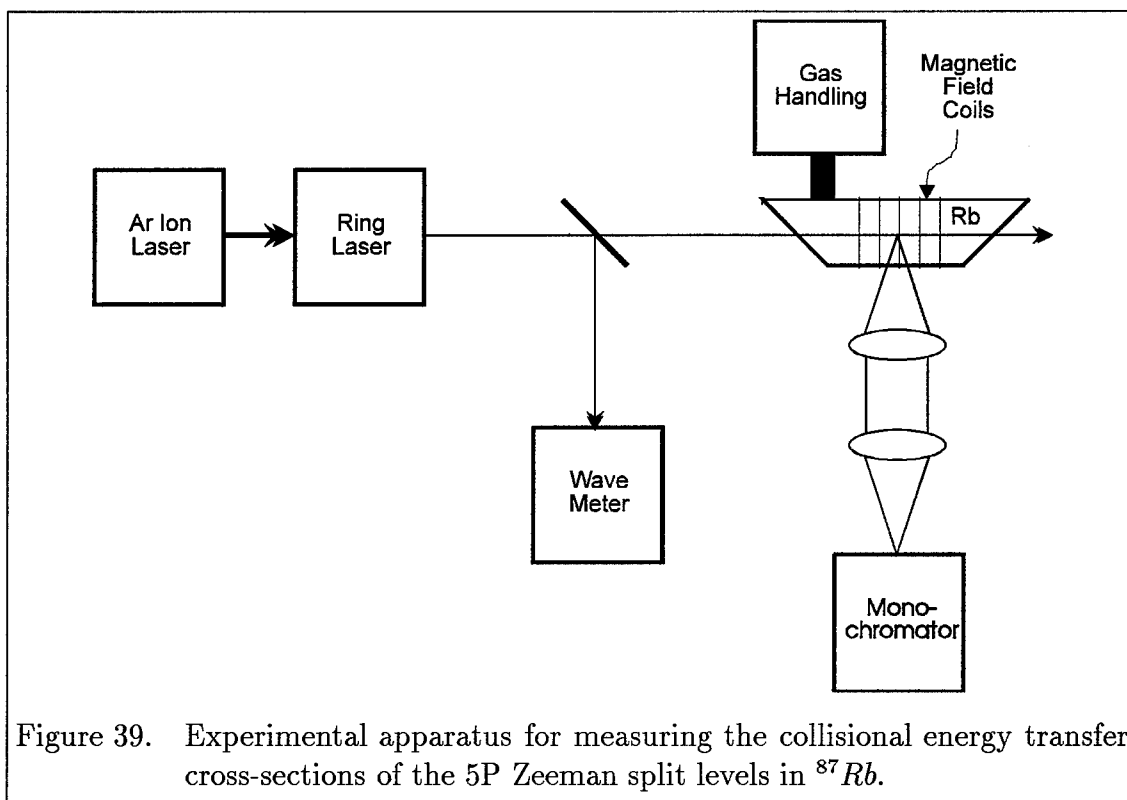


Figure 39. Experimental apparatus for measuring the collisional energy transfer cross-sections of the 5P Zeeman split levels in ^{87}Rb .

Similar problems existed for the Zeeman energy transfer as existed for the spin-orbit energy transfer. These included maintaining an appropriate rubidium concentration to ensure there was no self trapping or self transfer. Figure 40 illustrates the manner in which the appropriate rubidium concentration was obtained. Essentially, the intensity ratios for the $(l = 1, m_j = \frac{1}{2} \rightarrow l = 0, m_j = \pm\frac{1}{2})$ and $(l = 1, m_j = -\frac{1}{2} \rightarrow l = 0, m_j = \pm\frac{1}{2})$ transitions were used. These ratios should be equal and should not depend on the rubidium concentration. Since the two lines

from each level have different line strengths one line would be more strongly self absorbed than the other line causing a change in the ratio as a function of rubidium concentration. The observation path length was ≈ 2 mm, and the data collections were performed with a rubidium concentration of 10^{-7} Torr. Also there was the question of the affect the laser power would have on the measured rates. As with the spin-orbit case there did not seem to be any dependence of the rates on laser power. This is illustrated by Figure 41 by the approximately constant value in the intensity ratio. The intensity plot was curve fit to determine the saturation intensity. The value obtained was 0.1 ± 0.08 mW which leads to a saturation intensity of $3.2 \pm 2.6 \frac{\text{mW}}{\text{cm}^2}$ for a 0.2 cm diameter beam which is in good agreement with the previous measurement for the spin-orbit energy transfer.

An additional complication was the addition of the magnetic field. This imposed the constraint that the rubidium vapor cell must fit between the magnet's poles. In order to prevent rubidium from sticking to the walls of the cell it was necessary to heat the rubidium cell. This meant that thermal control of the Rb cell needed to be incorporated in a manner that did not interfere with the magnetic field. This was accomplished by wrapping the cell with a heat tape. The heat tape was applied in a single layer to allow for the smallest possible profile. The wrapped cell was then mounted between the magnet's poles. A probe to monitor the magnetic field was also placed between the poles. The field was then set to the operating level of 2 Tesla and the heat tape's voltage slowly increased to the operating voltage of 60 volts. No detectable change in the magnetic field was observed allowing the cell to be heated without affecting the magnetic field.

The monochromator was the key part of this experiment. The Zeeman line separation is $\approx B\mu_B g_J$ which for the $5^2P_{\frac{1}{2}}$ level is $\Delta\lambda \approx 0.037$ nm at 2 Tesla. The monochromator resolution at $\lambda = 780$ nm, was $\Delta\lambda = .012$ nm. This resolution was sufficient to resolve each peak in the spectrum, but insufficient to completely isolate each of the lines. Typical emission spectra is shown in Figures 42 through 46.

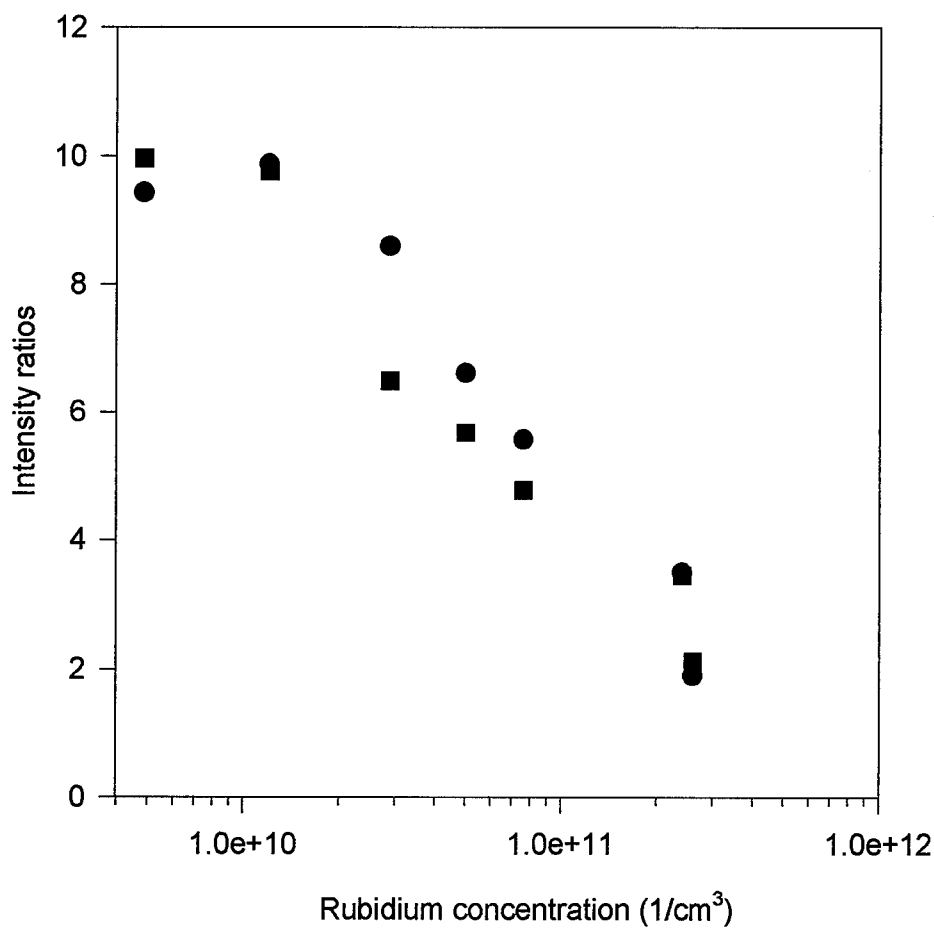


Figure 40. Intensity ratios versus rubidium concentration using 1 Torr of nitrogen. The circles are for $\frac{I(5^2P_{3/2}, m_j = \frac{1}{2} \rightarrow 5^2S_{1/2}, m_j = \frac{1}{2})}{I(5^2P_{3/2}, m_j = \frac{1}{2} \rightarrow 5^2S_{1/2}, m_j = -\frac{1}{2})}$ and the squares are for $\frac{I(5^2P_{3/2}, m_j = -\frac{1}{2} \rightarrow 5^2S_{1/2}, m_j = -\frac{1}{2})}{I(5^2P_{3/2}, m_j = -\frac{1}{2} \rightarrow 5^2S_{1/2}, m_j = \frac{1}{2})}$.

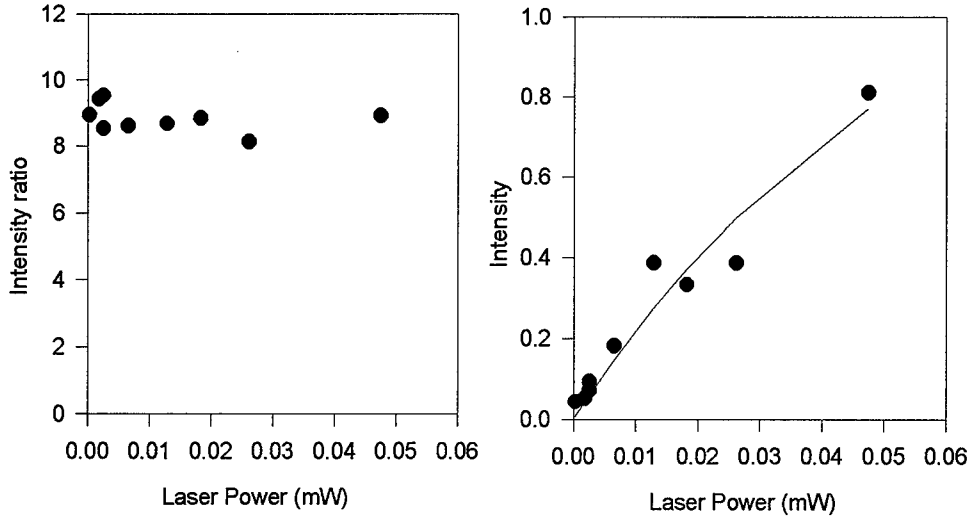


Figure 41. The figure on the left is for the intensity ratio $\frac{I(5^2P_{3/2}, m_j = \frac{1}{2} \rightarrow 5^2S_{1/2}, m_j = \frac{1}{2})}{I(5^2P_{3/2}, m_j = \frac{1}{2} \rightarrow 5^2S_{1/2}, m_j = -\frac{1}{2})}$ versus laser power, and the figure on the right is the fluorescence intensity of the prepared state versus laser power.

There was a systematic error in the data due to scattered light. The most severe case was the $5^2P_{3/2}, m_j = \pm\frac{3}{2}$ pumped lines shown in Figure 46. Because linearly polarized light was used to prepare these circularly polarized transitions the states could only be weakly prepared. Thus, a weak signal was observed which exaggerated the scattered light problem. As a note, because there was such a low signal it was not possible to acquire the spin-orbit transfer cross-sections for these levels. The scattered light problem was corrected as follows. A data-scan consisted of collecting the signal from the monochromator $I_m = I_{sig} + I_{sc}$ which consisted of the desired signal I_{sig} and the scattered light I_{sc} ; the total fluorescence $I_{tf} = I_f + I_{ts}$ which consisted of the total side fluorescence I_f and scattered light I_{ts} ; and the laser intensity I_{lp} . Turning the magnetic field off causes the resonant line in the rubidium to change frequency such that the only signal was from the scattered light. A second scan was then performed collecting the scatter signal I_{sc} , the total scatter

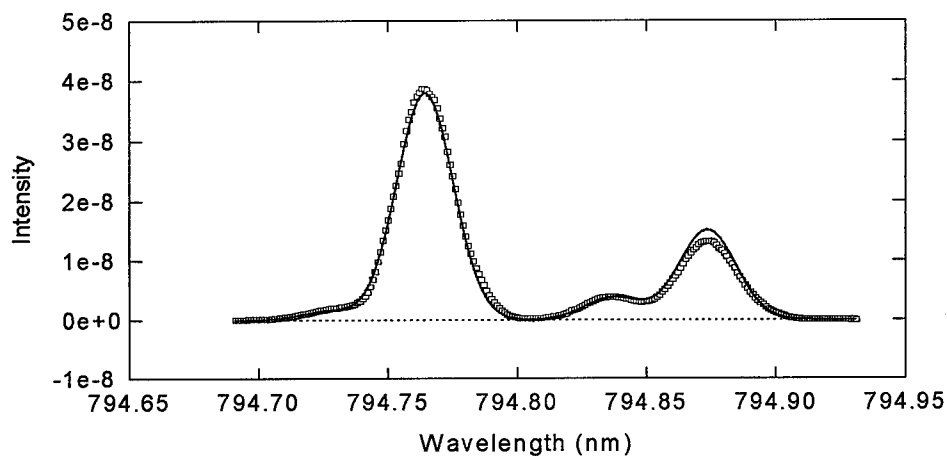


Figure 42. Typical scatter corrected data for the $(5^2S_{1/2}, m_j = -\frac{1}{2}) \rightarrow (5^2P_{1/2}, m_j = -\frac{1}{2})$ pumped transition at 1.2 Torr of nitrogen scanning the $5^2P_{1/2}$ manifold with the resulting curve fit shown.

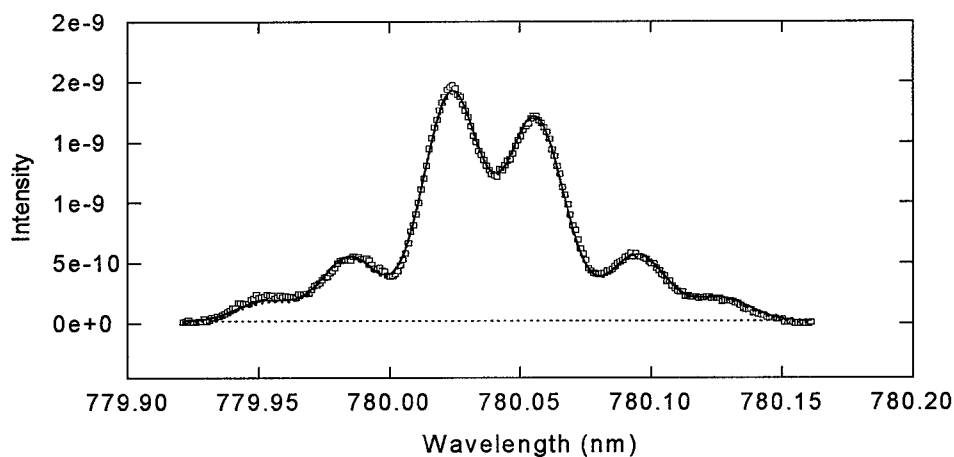


Figure 43. Typical scatter corrected data for the $(5^2S_{1/2}, m_j = -\frac{1}{2}) \rightarrow (5^2P_{3/2}, m_j = -\frac{1}{2})$ pumped transition at 1.2 Torr of nitrogen scanning the $5^2P_{3/2}$ manifold with the resulting curve fit shown.

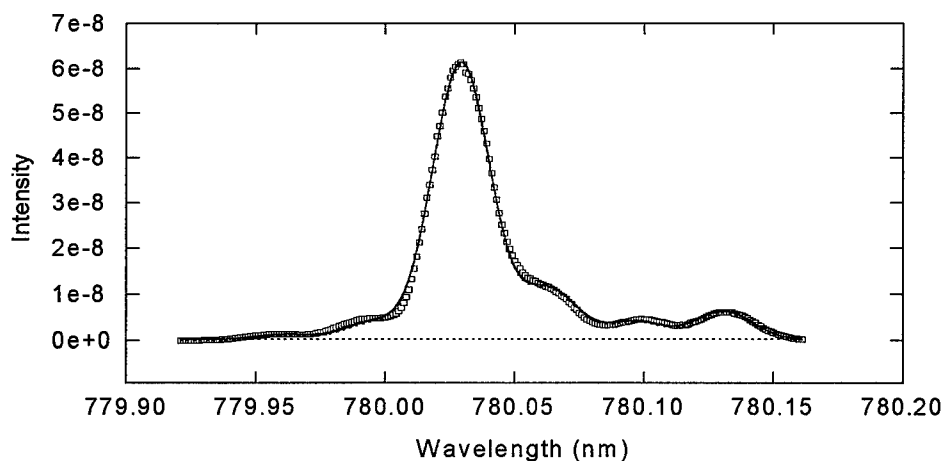


Figure 44. Typical scatter corrected data for the $(5^2S_{\frac{1}{2}}, m_j = -\frac{1}{2}) \rightarrow (5^2P_{\frac{3}{2}}, m_j = -\frac{1}{2})$ pumped transition at 1.2 Torr of nitrogen scanning the $5^2P_{\frac{3}{2}}$ manifold with the resulting curve fit shown.

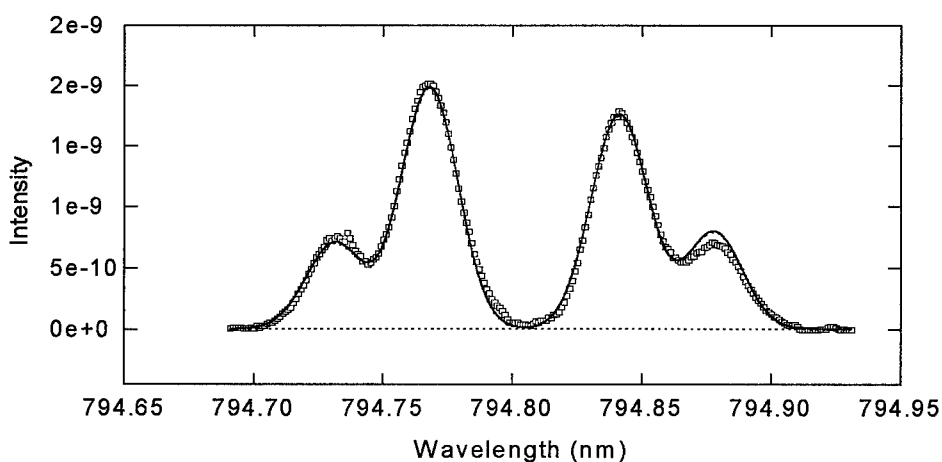


Figure 45. Typical scatter corrected data for the $(5^2S_{\frac{1}{2}}, m_j = -\frac{1}{2}) \rightarrow (5^2P_{\frac{3}{2}}, m_j = -\frac{1}{2})$ pumped transition at 1.2 Torr of nitrogen scanning the $5^2P_{\frac{3}{2}}$ manifold with the resulting curve fit shown.

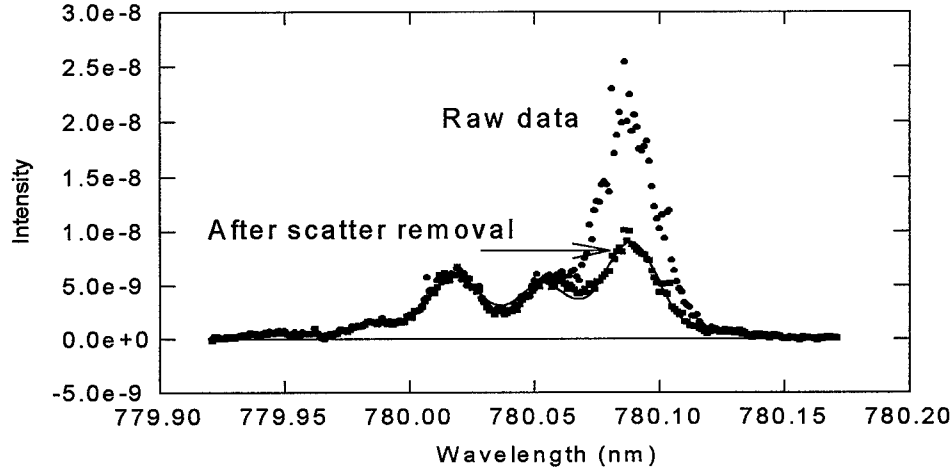


Figure 46. Typical scatter corrected data for the $(5^2S_{\frac{1}{2}}, m_j = -\frac{1}{2}) \rightarrow (5^2P_{\frac{3}{2}}, m_j = -\frac{3}{2})$ pumped transition at 1.0 Torr of nitrogen scanning the $5^2P_{\frac{3}{2}}$ manifold with the resulting curve fit shown. This figure also shows the data before the scatter is removed.

I_{ts} and the laser intensity I_{lps} . The total side fluorescence was then obtained using $I_f = (\frac{I_f + I_{ts}}{I_{lp}} - \frac{I_{ts}}{I_{lps}})I_{lp}$ and the signal was corrected by $I_{sig} = (\frac{I_{sig} + I_{sc}}{I_{lp}} - \frac{I_{sc}}{I_{lps}})I_{lp}$. The signal I_{sig} was ratioed to the total fluorescence I_f from the cell. This corrected for any drift in the laser's power or frequency. It also corrected for any changes in the rubidium concentration which might have occurred during a scan.

3.5 Data analysis

The scatter corrected data was curve fit using the software package Table Curve. The functional form used to fit the data was Gaussian. For the following analysis the arguments of the Gaussian function are defined to be

$$\text{Gaussian}(\text{Amplitude}, \text{PeakCenter}, \text{PeakFWHM})$$

$$I = I_0 + \sum_{i=1}^{4,6} \text{Gaussian}(I_i, \lambda_0 + \delta + \lambda_i, \Delta\lambda) \quad (63)$$

The summation ranges to four and six for the D_1 and D_2 lines respectively, I_0 is the fit parameter for the non zero base line, $\Delta\lambda$ is the fit parameter for the FWHM for each peak which is assumed to be the same for all peaks. i.e. the FWHM is defined by the monochromator's maximum resolution. The parameter λ_0 is 794.7 nm and 780.0 nm for the D_1 and D_2 lines respectively, δ is a curve fit parameter which allows a characterization of the shift of the entire spectrum due to error obtaining the initial scan position. The parameters I_i and λ_i are given in Table 17. The parameter λ_i is

Table 17. Coefficients for the Zeeman energy transfer curve fitting.

	I_i		λ_i	
i	D_1	D_2	D_1	D_2
1	$\frac{I_{+\frac{1}{2}}}{R_d}$	$\frac{2}{8} \frac{I_{-\frac{1}{2}}}{R_d}$	$-B_0\mu_B g_{j=\frac{1}{2}}$	$-B_0\mu_B g_{j=\frac{3}{2}}$
2	$I_{-\frac{1}{2}}$	$I_{+\frac{3}{2}}$	0	$-2B_0\mu_B(g_{j=\frac{3}{2}} - g_i)$
3	$I_{+\frac{1}{2}}$	$I_{-\frac{1}{2}}$	$B_0\mu_B(g_i - g_{j=\frac{1}{2}})$	0
4	$\frac{I_{-\frac{1}{2}}}{R_d}$	$I_{+\frac{1}{2}}$	$B_0\mu_B g_i$	$B_0\mu_B(g_i - g_{j=\frac{3}{2}})$
5	-	$I_{-\frac{3}{2}}$	-	$B_0\mu_B g_{j=\frac{3}{2}}$
6	-	$\frac{2}{8} \frac{I_{+\frac{1}{2}}}{R_d}$	-	$B_0\mu_B g_i$

the relative spacing between the peaks. The values for λ_i are derived by examining equations 47 and 54 in the high field limit and noting that the separation of the lines is given by $B_0\mu_B g_j$ and treating the $5^2P, m_j = -\frac{1}{2} \rightarrow 5^2S, m_j = -\frac{1}{2}$ as the reference line. The magnetic field B_0 , is a curve fit parameter to allow for fluctuations in the magnetic field. The last parameter I_i represents the intensity of each of the peaks. When the appropriate substitution are made I_{m_j} represents the curve fit parameter for the intensity of the m_j level and $R_d = 2.5$ is the relative detectivities

of the circular and linear polarization. Curve fits to the raw data are illustrated in Figures 42 through 46.

Once the intensities are determined they must be converted into number densities. This is accomplished by dividing each line by its line strength. The line strengths are given in Table 18. The number densities are ratioed $\frac{N_s}{N_p}$ and plotted

Table 18. Zeeman split lines theoretical line strengths.

Ref (84)	m_j	$+\frac{1}{2}$	$-\frac{1}{2}$
$P_{\frac{1}{2}}$	$+\frac{1}{2}$	4	4
	$-\frac{1}{2}$	4	4
$P_{\frac{3}{2}}$	$+\frac{3}{2}$	6	-
	$+\frac{1}{2}$	8	2
	$-\frac{1}{2}$	2	8
	$-\frac{3}{2}$	-	6

as a function of pressure as in Figures 47 through 52. This reduced data is further reduced by curve fitting it to equation 59 using the equivalent form

$$\frac{N_s}{N_p} = \frac{ax}{1 + bx} \quad (64)$$

where x is the pressure a is the rate of transfer relative to the A coefficient from the pumped level to the satellite level. The b coefficient is the quenching from the satellite level plus the total rate out of the satellite level due to collisions plus the total rate into the satellite level from the other satellite levels all of which is relative to the A coefficient. The curve fits performed in this manner are shown graphically in Figures 47 through 52. Table 19 and in an alternate form Table 25 list the cross-sections for the Zeeman energy transfer. Given in Table 26 are the only other Zeeman energy transfer cross-sections that could be found for rubidium. These cross-sections are for the 6^2P levels and are provided for comparison purposes only.

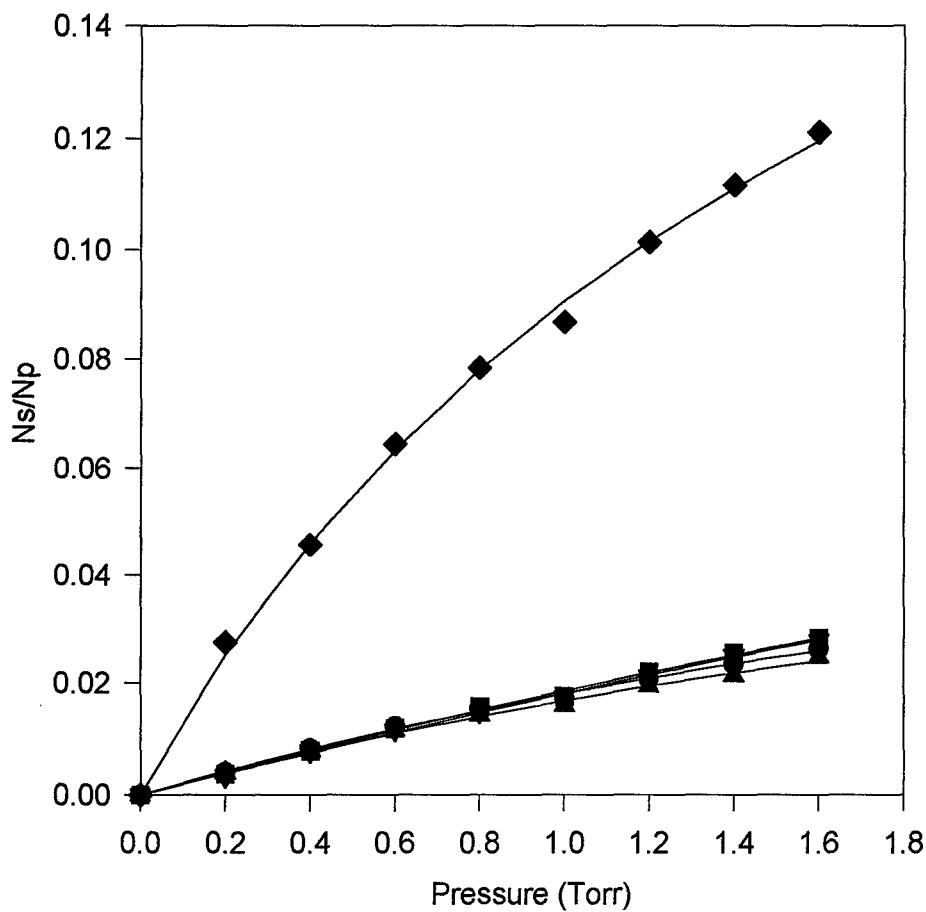


Figure 47. Zeeman energy transfer to the satellite levels with the $5^2P_{\frac{1}{2}}, m_j = -\frac{1}{2}$ level prepared by pumping the $5^2S_{\frac{1}{2}}, m_j = -\frac{1}{2} \rightarrow 5^2P_{\frac{1}{2}}, m_j = -\frac{1}{2}$ transition. $\diamond \frac{N_S(5^2P_{\frac{1}{2}}, m_j = +\frac{1}{2})}{N_P}$, $\square \frac{N_S(5^2P_{\frac{3}{2}}, m_j = -\frac{1}{2})}{N_P}$, $\nabla \frac{N_S(5^2P_{\frac{3}{2}}, m_j = -\frac{3}{2})}{N_P}$, $\circ \frac{N_S(5^2P_{\frac{3}{2}}, m_j = +\frac{3}{2})}{N_P}$, and $\triangle \frac{N_S(5^2P_{\frac{3}{2}}, m_j = +\frac{1}{2})}{N_P}$.

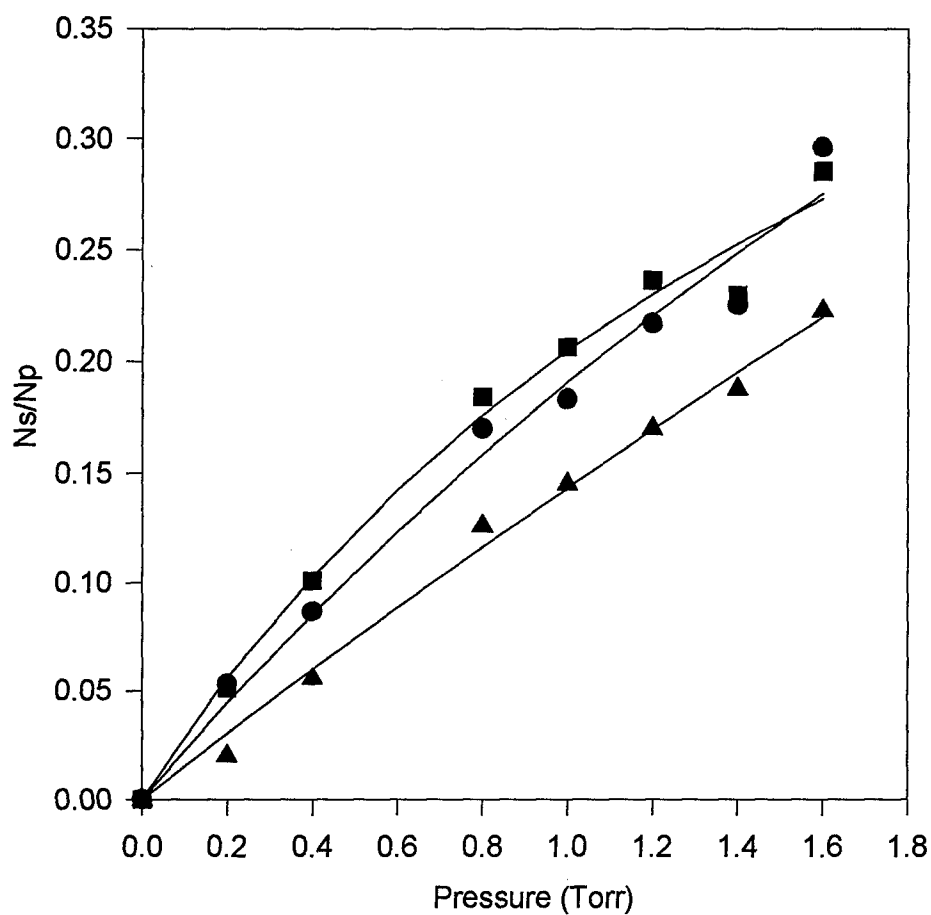


Figure 48. Zeeman energy transfer to the satellite levels with the $5^2P_{3/2}, m_j = \frac{3}{2}$ level prepared by pumping the $5^2S_{1/2}, m_j = \frac{1}{2} \rightarrow 5^2P_{3/2}, m_j = \frac{3}{2}$ transition. ○ $\frac{N_S(5^2P_{3/2}, m_j = -1/2)}{N_P}$, □ $\frac{N_S(5^2P_{3/2}, m_j = +1/2)}{N_P}$, and △ $\frac{N_S(5^2P_{3/2}, m_j = -3/2)}{N_P}$.

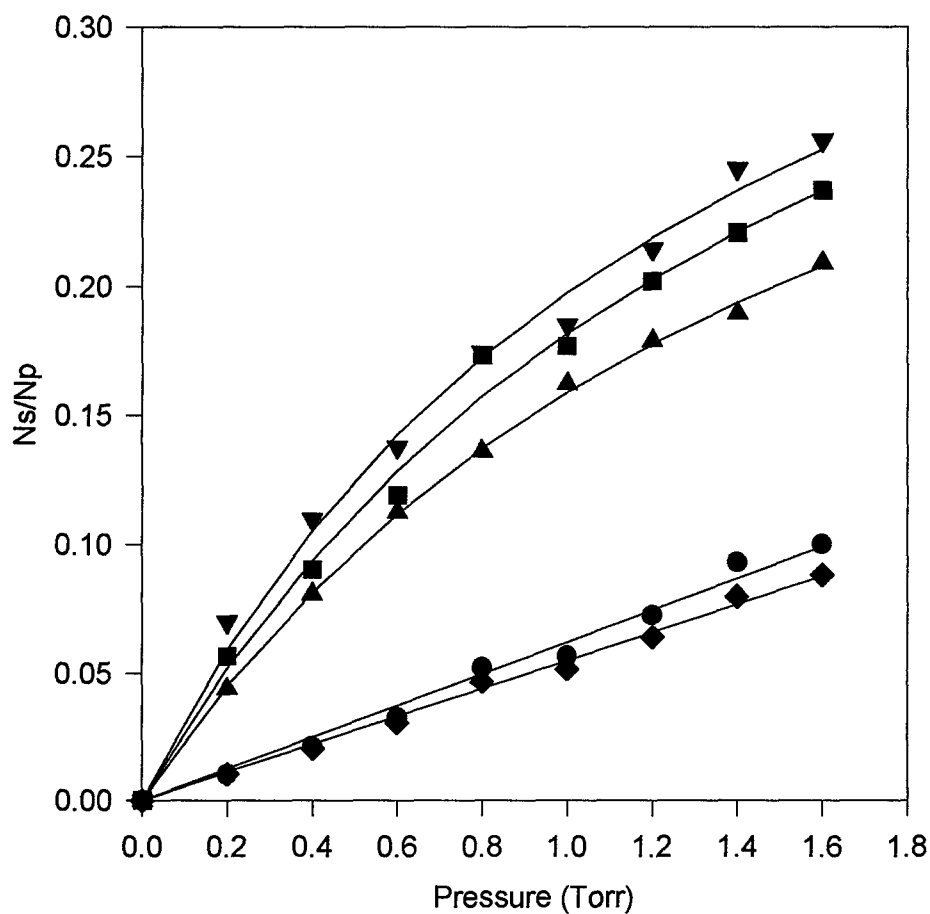


Figure 49. Zeeman energy transfer to the satellite levels with the $5^2P_{3/2}, m_j = -\frac{1}{2}$ level prepared by pumping the $5^2S_{1/2}, m_j = -\frac{1}{2} \rightarrow 5^2P_{3/2}, m_j = -\frac{1}{2}$ transition. $\nabla \frac{N_S(5^2P_{3/2}, m_j = -\frac{3}{2})}{N_P}$, $\square \frac{N_S(5^2P_{3/2}, m_j = +\frac{3}{2})}{N_P}$, $\triangle \frac{N_S(5^2P_{3/2}, m_j = +\frac{1}{2})}{N_P}$, $\circ \frac{N_S(5^2P_{1/2}, m_j = -\frac{1}{2})}{N_P}$, and $\diamond \frac{N_S(5^2P_{1/2}, m_j = +\frac{1}{2})}{N_P}$.

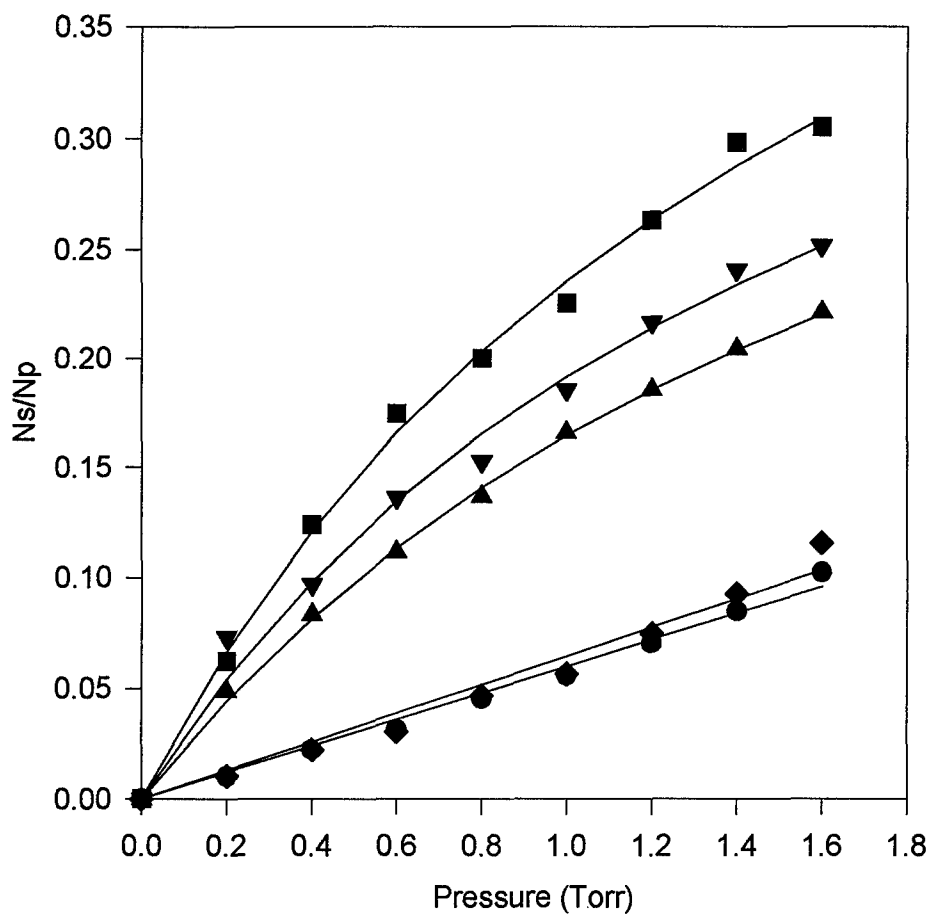


Figure 50. Zeeman energy transfer to the satellite levels with the $5^2P_{3/2}, m_j = \frac{1}{2}$ level prepared by pumping the $5^2S_{1/2}, m_j = \frac{1}{2} \rightarrow 5^2P_{3/2}, m_j = \frac{1}{2}$ transition. $\square \frac{N_S(5^2P_{3/2}, m_j=+\frac{3}{2})}{N_P}$, $\nabla \frac{N_S(5^2P_{3/2}, m_j=-\frac{3}{2})}{N_P}$, $\triangle \frac{N_S(5^2P_{3/2}, m_j=-\frac{1}{2})}{N_P}$, $\diamond \frac{N_S(5^2P_{1/2}, m_j=+\frac{1}{2})}{N_P}$ and $\circ \frac{N_S(5^2P_{1/2}, m_j=-\frac{1}{2})}{N_P}$.

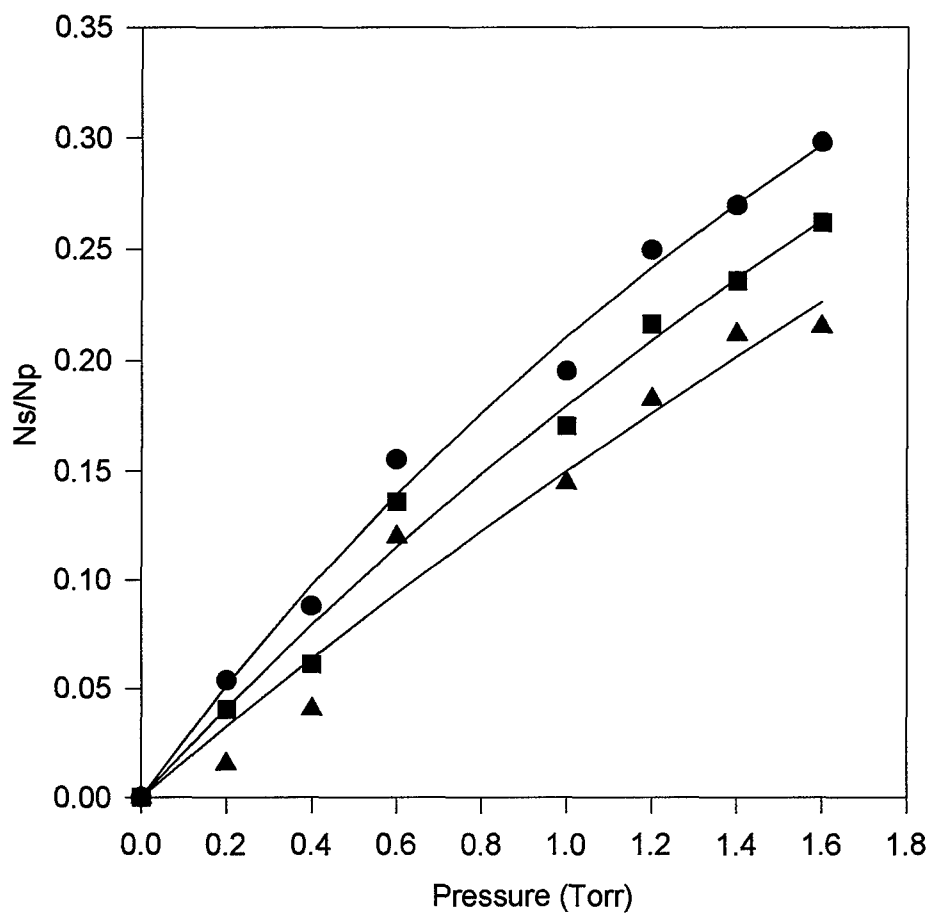


Figure 51. Zeeman energy transfer to the satellite levels with the $5^2P_{3/2}, m_j = -\frac{3}{2}$ level prepared by pumping the $5^2S_{1/2}, m_j = -\frac{1}{2} \rightarrow 5^2P_{3/2}, m_j = -\frac{3}{2}$ transition. $\bigcirc \frac{N_S(5^2P_{3/2}, m_j = -\frac{1}{2})}{N_P}$, $\square \frac{N_S(5^2P_{3/2}, m_j = +\frac{1}{2})}{N_P}$, and $\triangle \frac{N_S(5^2P_{3/2}, m_j = +\frac{3}{2})}{N_P}$.

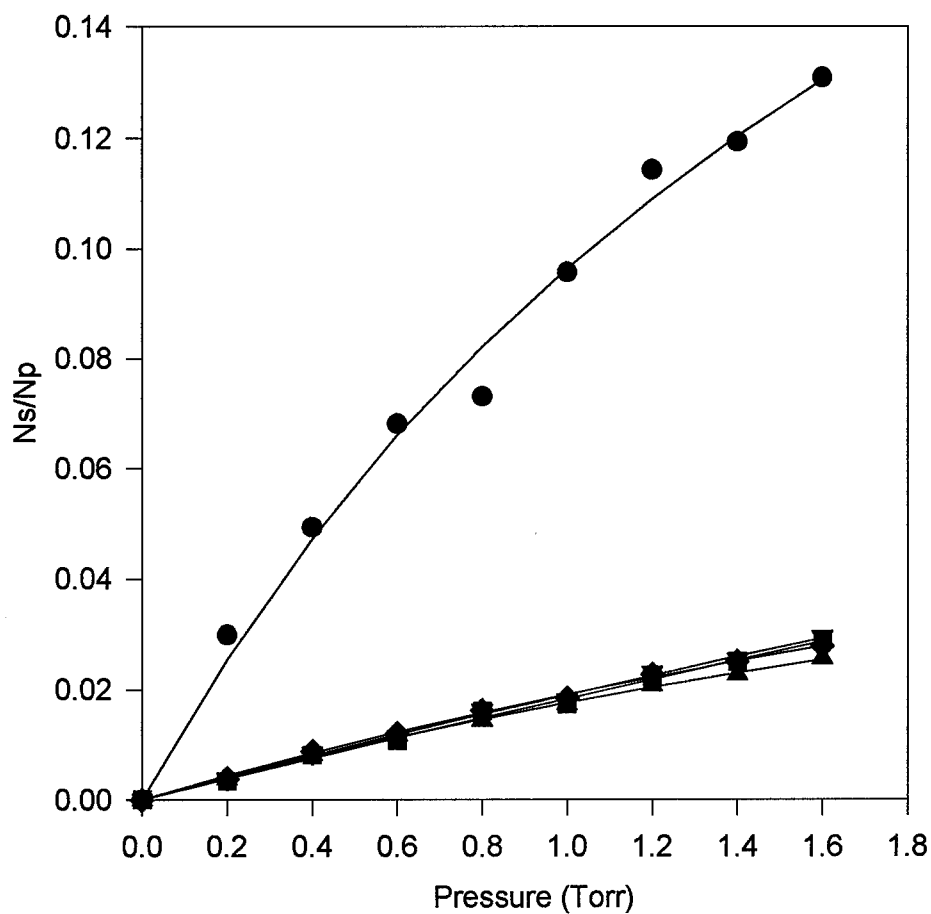


Figure 52. Zeeman energy transfer to the satellite levels with the $5^2P_{\frac{1}{2}}, m_j = \frac{1}{2}$ level prepared by pumping the $5^2S_{\frac{1}{2}}, m_j = \frac{1}{2} \rightarrow 5^2P_{\frac{1}{2}}, m_j = \frac{1}{2}$ transition. $\bigcirc \frac{N_S(5^2P_{\frac{1}{2}}, m_j = -\frac{1}{2})}{N_P}$, $\nabla \frac{N_S(5^2P_{\frac{3}{2}}, m_j = +\frac{1}{2})}{N_P}$, $\square \frac{N_S(5^2P_{\frac{3}{2}}, m_j = +\frac{3}{2})}{N_P}$, $\diamond \frac{N_S(5^2P_{\frac{3}{2}}, m_j = -\frac{3}{2})}{N_P}$ and $\triangle \frac{N_S(5^2P_{\frac{3}{2}}, m_j = -\frac{1}{2})}{N_P}$.

Table 19. Excitation transfer cross-sections for the 5^2P Zeeman split levels in Rb induced by collisions with nitrogen.

\AA^2		Satellite					
P	J, m_j	$\frac{3}{2}, +\frac{3}{2}$	$\frac{3}{2}, +\frac{1}{2}$	$\frac{3}{2}, -\frac{1}{2}$	$\frac{3}{2}, -\frac{3}{2}$	$\frac{1}{2}, +\frac{1}{2}$	$\frac{1}{2}, -\frac{1}{2}$
a	$\frac{3}{2}, +\frac{3}{2}$	-	75 ± 9	57 ± 8	37 ± 4	-	-
r	$\frac{3}{2}, +\frac{1}{2}$	90 ± 5	-	59 ± 2	73 ± 7	15 ± 2	14 ± 1
e	$\frac{3}{2}, -\frac{1}{2}$	71 ± 5	61 ± 2	-	82 ± 6	13 ± 1	15 ± 1
n	$\frac{3}{2}, -\frac{3}{2}$	40 ± 8	52 ± 6	66 ± 6	-	-	-
t	$\frac{1}{2}, +\frac{1}{2}$	4.7 ± 0.3	5.0 ± 0.2	5.2 ± 0.1	5.5 ± 0.2	-	32 ± 3
	$\frac{1}{2}, -\frac{1}{2}$	5.4 ± 0.2	5.1 ± 0.2	4.9 ± 0.2	4.7 ± 0.2	33 ± 1	-

In Tables 20, 21 and 22 the relations between the cross-sections given in equations 60, 61 and 62 respectively are compared for the nitrogen gas data. As can be seen, in all cases there is very good agreement for all three relations. The only exceptions are the values obtained from the $5^2P_{\frac{3}{2}}, m_j = \frac{3}{2}$, and the $5^2P_{\frac{3}{2}}, m_j = -\frac{3}{2}$ pumped lines. This less than ideal agreement is attributed to the poor signal to noise ratio of the data taken for these lines.

Seeing that these relations appear to be valid, then by applying them, the set of independent cross-sections can be reduced from thirty to nine and are reported in Table 23. Noting that the last four entries in Table 23 are the spin-orbit energy transfer rates, the set of independent Zeeman cross-sections is reduced to six. Figure 53 graphically represents the energy transfer process that each cross-section represents. The values measured for each of the gases is given in Table 24.

Table 20. Comparison of the Zeeman energy transfer cross-sections for nitrogen using detail-balance.

$J, +m \rightarrow J, +m$	\bar{A}^2	Ratio	$e^{\frac{\Delta E}{kT}}$
$\frac{3}{2}, +\frac{3}{2} \rightarrow \frac{3}{2}, +\frac{1}{2}$	75 ± 9	0.83 ± 0.16	1
$\frac{3}{2}, +\frac{1}{2} \rightarrow \frac{3}{2}, +\frac{3}{2}$	90 ± 5		
$\frac{3}{2}, +\frac{3}{2} \rightarrow \frac{3}{2}, -\frac{1}{2}$	57 ± 8	0.80 ± 0.18	1
$\frac{3}{2}, -\frac{1}{2} \rightarrow \frac{3}{2}, +\frac{3}{2}$	71 ± 5		
$\frac{3}{2}, +\frac{3}{2} \rightarrow \frac{3}{2}, -\frac{3}{2}$	37 ± 4	0.93 ± 0.35	1
$\frac{3}{2}, -\frac{3}{2} \rightarrow \frac{3}{2}, +\frac{3}{2}$	40 ± 8		
$\frac{3}{2}, +\frac{1}{2} \rightarrow \frac{3}{2}, -\frac{1}{2}$	59 ± 2	0.97 ± 0.06	1
$\frac{3}{2}, -\frac{1}{2} \rightarrow \frac{3}{2}, +\frac{1}{2}$	61 ± 2		
$\frac{3}{2}, +\frac{1}{2} \rightarrow \frac{3}{2}, -\frac{3}{2}$	73 ± 7	1.4 ± 0.24	1
$\frac{3}{2}, -\frac{3}{2} \rightarrow \frac{3}{2}, +\frac{1}{2}$	52 ± 6		
$\frac{3}{2}, -\frac{1}{2} \rightarrow \frac{3}{2}, -\frac{3}{2}$	82 ± 6	1.24 ± 0.18	1
$\frac{3}{2}, -\frac{3}{2} \rightarrow \frac{3}{2}, -\frac{1}{2}$	66 ± 6		
$\frac{1}{2}, +\frac{1}{2} \rightarrow \frac{1}{2}, -\frac{1}{2}$	32 ± 3	0.97 ± 0.12	1
$\frac{1}{2}, -\frac{1}{2} \rightarrow \frac{1}{2}, +\frac{3}{2}$	33 ± 1		
$\frac{1}{2}, +\frac{1}{2} \rightarrow \frac{3}{2}, +\frac{1}{2}$	5.0 ± 0.2	0.33 ± 0.07	0.36
$\frac{3}{2}, +\frac{1}{2} \rightarrow \frac{1}{2}, +\frac{1}{2}$	15 ± 2		
$\frac{1}{2}, +\frac{1}{2} \rightarrow \frac{3}{2}, -\frac{1}{2}$	5.2 ± 0.1	0.40 ± 0.04	0.36
$\frac{3}{2}, -\frac{1}{2} \rightarrow \frac{1}{2}, +\frac{1}{2}$	13 ± 1		
$\frac{1}{2}, -\frac{1}{2} \rightarrow \frac{3}{2}, +\frac{1}{2}$	5.1 ± 0.2	0.36 ± 0.05	0.36
$\frac{3}{2}, +\frac{1}{2} \rightarrow \frac{1}{2}, -\frac{1}{2}$	14 ± 1		
$\frac{1}{2}, -\frac{1}{2} \rightarrow \frac{3}{2}, -\frac{1}{2}$	4.9 ± 0.2	0.33 ± 0.03	0.36
$\frac{3}{2}, -\frac{1}{2} \rightarrow \frac{1}{2}, -\frac{1}{2}$	15 ± 1		

Table 21. Comparison of the Zeeman energy transfer cross-sections for nitrogen using the relation $\sigma(J, m \rightarrow J, m') = \sigma(J, -m \rightarrow J, -m')$.

$J = \frac{3}{2} \text{ } ^1\text{A}^2$					$J = \frac{1}{2} \text{ } ^1\text{A}^2$	
$+m \rightarrow +m'$	$+\frac{3}{2}$	$+\frac{1}{2}$	$-\frac{1}{2}$	$-\frac{3}{2}$	$+m \rightarrow +m'$	$-\frac{1}{2}$
$-m \rightarrow -m'$	$-\frac{3}{2}$	$-\frac{1}{2}$	$+\frac{1}{2}$	$+\frac{3}{2}$	$-m \rightarrow -m'$	$+\frac{1}{2}$
$+\frac{3}{2}$	-	75 ± 9	57 ± 8	37 ± 4	$+\frac{1}{2}$	32 ± 3
$-\frac{3}{2}$	-	66 ± 6	52 ± 6	40 ± 8	$-\frac{1}{2}$	33 ± 1
$+\frac{1}{2}$	90 ± 5	-	59 ± 2	73 ± 7		
$-\frac{1}{2}$	82 ± 6	-	61 ± 2	71 ± 5		

Table 22. Comparison of the Zeeman energy transfer cross-sections for nitrogen using the relation $\sigma(J, m \rightarrow J', m) = \sigma(J, -m \rightarrow J', -m)$.

$J, +m \rightarrow J', +m$	$\frac{3}{2}, +\frac{3}{2}$	$\frac{3}{2}, +\frac{1}{2}$	$\frac{3}{2}, -\frac{1}{2}$	$\frac{3}{2}, -\frac{3}{2}$
$J, -m \rightarrow J', -m$	$\frac{3}{2}, -\frac{3}{2}$	$\frac{3}{2}, -\frac{1}{2}$	$\frac{3}{2}, +\frac{1}{2}$	$\frac{3}{2}, +\frac{3}{2}$
$\frac{1}{2}, +\frac{1}{2}$	4.7 ± 0.3	5.0 ± 0.2	5.2 ± 0.1	5.5 ± 0.2
$\frac{1}{2}, -\frac{1}{2}$	4.7 ± 0.2	4.9 ± 0.2	5.1 ± 0.2	5.4 ± 0.2

$J, +m \rightarrow J, +m$	$\frac{1}{2}, +\frac{1}{2}$	$\frac{1}{2}, -\frac{1}{2}$
$J, -m \rightarrow J, -m$	$\frac{1}{2}, -\frac{1}{2}$	$\frac{1}{2}, +\frac{1}{2}$
$\frac{3}{2}, +\frac{1}{2}$	15 ± 2	14 ± 1
$\frac{3}{2}, -\frac{1}{2}$	15 ± 1	13 ± 1

Table 23. Resulting cross-sections after applying the relations.

a	$\sigma(\frac{3}{2}, +\frac{1}{2} \rightarrow \frac{3}{2}, -\frac{1}{2}) = \sigma(\frac{3}{2}, -\frac{1}{2} \rightarrow \frac{3}{2}, +\frac{1}{2})$
b	$\sigma(\frac{3}{2}, +\frac{3}{2} \rightarrow \frac{3}{2}, -\frac{3}{2}) = \sigma(\frac{3}{2}, -\frac{3}{2} \rightarrow \frac{3}{2}, +\frac{3}{2})$
c	$\sigma(\frac{1}{2}, +\frac{1}{2} \rightarrow \frac{1}{2}, -\frac{1}{2}) = \sigma(\frac{1}{2}, -\frac{1}{2} \rightarrow \frac{1}{2}, +\frac{1}{2})$
d	$\sigma(\frac{3}{2}, +\frac{3}{2} \rightarrow \frac{3}{2}, +\frac{1}{2}) = \sigma(\frac{3}{2}, +\frac{1}{2} \rightarrow \frac{3}{2}, +\frac{3}{2}) = \sigma(\frac{3}{2}, -\frac{1}{2} \rightarrow \frac{3}{2}, -\frac{3}{2}) = \sigma(\frac{3}{2}, -\frac{3}{2} \rightarrow \frac{3}{2}, -\frac{1}{2})$
e	$\sigma(\frac{3}{2}, +\frac{3}{2} \rightarrow \frac{3}{2}, -\frac{1}{2}) = \sigma(\frac{3}{2}, -\frac{1}{2} \rightarrow \frac{3}{2}, +\frac{3}{2}) = \sigma(\frac{3}{2}, +\frac{1}{2} \rightarrow \frac{3}{2}, -\frac{3}{2}) = \sigma(\frac{3}{2}, -\frac{3}{2} \rightarrow \frac{3}{2}, +\frac{1}{2})$
f	$\sigma(\frac{1}{2}, -\frac{1}{2} \rightarrow \frac{3}{2}, -\frac{1}{2}) = \sigma(\frac{1}{2}, +\frac{1}{2} \rightarrow \frac{3}{2}, +\frac{1}{2}) \propto \sigma(\frac{3}{2}, +\frac{1}{2} \rightarrow \frac{1}{2}, +\frac{1}{2}) = \sigma(\frac{3}{2}, -\frac{1}{2} \rightarrow \frac{1}{2}, -\frac{1}{2})$ $\sigma(\frac{1}{2}, -\frac{1}{2} \rightarrow \frac{3}{2}, +\frac{1}{2}) = \sigma(\frac{1}{2}, +\frac{1}{2} \rightarrow \frac{3}{2}, -\frac{1}{2}) \propto \sigma(\frac{3}{2}, -\frac{1}{2} \rightarrow \frac{1}{2}, +\frac{1}{2}) = \sigma(\frac{3}{2}, +\frac{1}{2} \rightarrow \frac{1}{2}, -\frac{1}{2})$ $\sigma(\frac{3}{2}, -\frac{3}{2} \rightarrow \frac{1}{2}, -\frac{1}{2}) = \sigma(\frac{3}{2}, +\frac{3}{2} \rightarrow \frac{1}{2}, +\frac{1}{2}) \propto \sigma(\frac{1}{2}, +\frac{1}{2} \rightarrow \frac{3}{2}, +\frac{3}{2}) = \sigma(\frac{1}{2}, -\frac{1}{2} \rightarrow \frac{3}{2}, -\frac{3}{2})$ $\sigma(\frac{3}{2}, +\frac{3}{2} \rightarrow \frac{1}{2}, -\frac{1}{2}) = \sigma(\frac{3}{2}, -\frac{3}{2} \rightarrow \frac{1}{2}, +\frac{1}{2}) \propto \sigma(\frac{1}{2}, +\frac{1}{2} \rightarrow \frac{3}{2}, -\frac{3}{2}) = \sigma(\frac{1}{2}, -\frac{1}{2} \rightarrow \frac{3}{2}, +\frac{3}{2})$

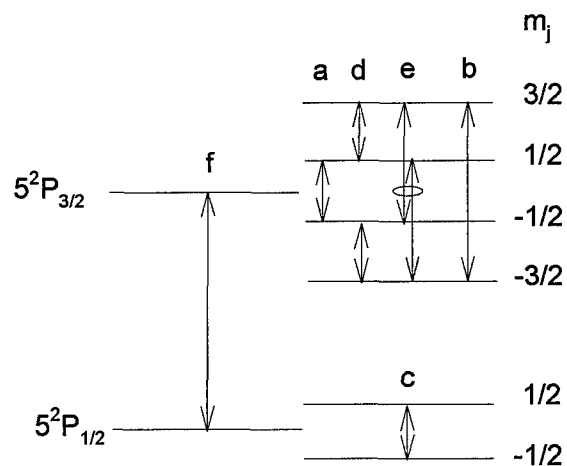


Figure 53. Reduced set of energy transfer cross-sections.

Table 24. Reduced set of cross-sections for each gas.

\AA^2	N_2	He	Ne	Ar	Kr	Xe
a	59 ± 2	34 ± 4	50 ± 3	57 ± 3	109 ± 13	115 ± 14
b	37 ± 4	-	-	-	-	-
c	32 ± 3	16 ± 1	35 ± 8	24 ± 5	34 ± 5	39 ± 4
d	90 ± 5	64 ± 7	139 ± 10	150 ± 26	248 ± 23	224 ± 28
e	73 ± 7	75 ± 9	154 ± 10	131 ± 13	223 ± 29	243 ± 36

Table 25. Excitation transfer cross-sections for the 5^2P Zeeman split levels in Rb induced by collisions with neutral gases.

Designation	This Work \AA^2					
$\sigma(J, m \rightarrow J', m')$	N2	He	Ne	Ar	Kr	Xe
$\sigma(\frac{3}{2}, +\frac{1}{2} \rightarrow \frac{1}{2}, +\frac{1}{2})$	15 ± 2					
$\sigma(\frac{3}{2}, +\frac{1}{2} \rightarrow \frac{1}{2}, -\frac{1}{2})$	14 ± 1					
$\sigma(\frac{3}{2}, +\frac{1}{2} \rightarrow \frac{3}{2}, +\frac{3}{2})$	90 ± 5	64 ± 7	139 ± 10	150 ± 26	248 ± 23	223 ± 28
$\sigma(\frac{3}{2}, +\frac{1}{2} \rightarrow \frac{3}{2}, -\frac{3}{2})$	73 ± 7	75 ± 9	154 ± 10	131 ± 13	223 ± 29	243 ± 36
$\sigma(\frac{3}{2}, +\frac{1}{2} \rightarrow \frac{3}{2}, -\frac{1}{2})$	59 ± 2	34 ± 4	50 ± 3	57 ± 3	109 ± 13	115 ± 14
$\sigma(\frac{3}{2}, +\frac{3}{2} \rightarrow \frac{1}{2}, +\frac{1}{2})$	-					
$\sigma(\frac{3}{2}, +\frac{3}{2} \rightarrow \frac{1}{2}, -\frac{1}{2})$	-					
$\sigma(\frac{3}{2}, +\frac{3}{2} \rightarrow \frac{3}{2}, +\frac{1}{2})$	75 ± 9					
$\sigma(\frac{3}{2}, +\frac{3}{2} \rightarrow \frac{3}{2}, -\frac{3}{2})$	37 ± 4					
$\sigma(\frac{3}{2}, +\frac{3}{2} \rightarrow \frac{3}{2}, -\frac{1}{2})$	57 ± 8					
$\sigma(\frac{3}{2}, -\frac{3}{2} \rightarrow \frac{1}{2}, +\frac{1}{2})$	-					
$\sigma(\frac{3}{2}, -\frac{3}{2} \rightarrow \frac{1}{2}, -\frac{1}{2})$	-					
$\sigma(\frac{3}{2}, -\frac{3}{2} \rightarrow \frac{3}{2}, +\frac{1}{2})$	52 ± 6					
$\sigma(\frac{3}{2}, -\frac{3}{2} \rightarrow \frac{3}{2}, +\frac{3}{2})$	40 ± 8					
$\sigma(\frac{3}{2}, -\frac{3}{2} \rightarrow \frac{3}{2}, -\frac{1}{2})$	66 ± 6					
$\sigma(\frac{3}{2}, -\frac{1}{2} \rightarrow \frac{1}{2}, +\frac{1}{2})$	13 ± 1					
$\sigma(\frac{3}{2}, -\frac{1}{2} \rightarrow \frac{1}{2}, -\frac{1}{2})$	15 ± 1					
$\sigma(\frac{3}{2}, -\frac{1}{2} \rightarrow \frac{3}{2}, +\frac{1}{2})$	61 ± 2					
$\sigma(\frac{3}{2}, -\frac{1}{2} \rightarrow \frac{3}{2}, +\frac{3}{2})$	71 ± 5					
$\sigma(\frac{3}{2}, -\frac{1}{2} \rightarrow \frac{3}{2}, -\frac{3}{2})$	82 ± 6					
$\sigma(\frac{1}{2}, +\frac{1}{2} \rightarrow \frac{1}{2}, -\frac{1}{2})$	32 ± 3	16 ± 1	35 ± 8	24 ± 5	34 ± 5	39 ± 4
$\sigma(\frac{1}{2}, +\frac{1}{2} \rightarrow \frac{3}{2}, +\frac{1}{2})$	$5.0 \pm .2$					
$\sigma(\frac{1}{2}, +\frac{1}{2} \rightarrow \frac{3}{2}, +\frac{3}{2})$	$4.7 \pm .3$					
$\sigma(\frac{1}{2}, +\frac{1}{2} \rightarrow \frac{3}{2}, -\frac{3}{2})$	$5.5 \pm .2$					
$\sigma(\frac{1}{2}, +\frac{1}{2} \rightarrow \frac{3}{2}, -\frac{1}{2})$	$5.2 \pm .1$					
$\sigma(\frac{1}{2}, -\frac{1}{2} \rightarrow \frac{1}{2}, +\frac{1}{2})$	33 ± 1					
$\sigma(\frac{1}{2}, -\frac{1}{2} \rightarrow \frac{3}{2}, +\frac{1}{2})$	$5.1 \pm .2$					
$\sigma(\frac{1}{2}, -\frac{1}{2} \rightarrow \frac{3}{2}, +\frac{3}{2})$	$5.4 \pm .2$					
$\sigma(\frac{1}{2}, -\frac{1}{2} \rightarrow \frac{3}{2}, -\frac{3}{2})$	$4.7 \pm .2$					
$\sigma(\frac{1}{2}, -\frac{1}{2} \rightarrow \frac{3}{2}, -\frac{1}{2})$	$4.9 \pm .2$					

Table 26. Excitation transfer cross-sections for the 6^2P Zeeman split levels in Rb induced by collisions with rare gas atoms.

Designation	Ref	(46)	
$\sigma(J, m \rightarrow J', m')$	He	Ne	Ar
$\sigma(\frac{3}{2}, +\frac{1}{2} \rightarrow \frac{1}{2}, +\frac{1}{2})$	50 ± 13	9 ± 2.5	16 ± 5
$\sigma(\frac{3}{2}, +\frac{1}{2} \rightarrow \frac{1}{2}, -\frac{1}{2})$	45 ± 13	9 ± 3	16 ± 5
$\sigma(\frac{3}{2}, +\frac{1}{2} \rightarrow \frac{3}{2}, +\frac{3}{2})$	483 ± 85	140 ± 30	218 ± 45
$\sigma(\frac{3}{2}, +\frac{1}{2} \rightarrow \frac{3}{2}, -\frac{3}{2})$	521 ± 100	163 ± 30	155 ± 30
$\sigma(\frac{3}{2}, +\frac{1}{2} \rightarrow \frac{3}{2}, -\frac{1}{2})$	334 ± 65	136 ± 30	140 ± 30
$\sigma(\frac{3}{2}, +\frac{3}{2} \rightarrow \frac{1}{2}, +\frac{1}{2})$	76 ± 24	16 ± 5	32 ± 9
$\sigma(\frac{3}{2}, +\frac{3}{2} \rightarrow \frac{1}{2}, -\frac{1}{2})$	-	17 ± 5	32 ± 9
$\sigma(\frac{3}{2}, +\frac{3}{2} \rightarrow \frac{3}{2}, +\frac{1}{2})$	-	-	292 ± 115
$\sigma(\frac{3}{2}, +\frac{3}{2} \rightarrow \frac{3}{2}, -\frac{1}{2})$	-	244 ± 50	272 ± 100
$\sigma(\frac{3}{2}, +\frac{3}{2} \rightarrow \frac{3}{2}, -\frac{3}{2})$	-	296 ± 60	343 ± 120
$\sigma(\frac{3}{2}, -\frac{3}{2} \rightarrow \frac{1}{2}, +\frac{1}{2})$	42.0 ± 20	-	34 ± 15
$\sigma(\frac{3}{2}, -\frac{3}{2} \rightarrow \frac{1}{2}, -\frac{1}{2})$	31 ± 9	-	22 ± 7
$\sigma(\frac{3}{2}, -\frac{3}{2} \rightarrow \frac{3}{2}, +\frac{1}{2})$	378 ± 75	187 ± 35	285 ± 50
$\sigma(\frac{3}{2}, -\frac{3}{2} \rightarrow \frac{3}{2}, +\frac{3}{2})$	283 ± 55	185 ± 35	212 ± 105
$\sigma(\frac{3}{2}, -\frac{3}{2} \rightarrow \frac{3}{2}, -\frac{1}{2})$	425 ± 210	311 ± 90	374 ± 180
$\sigma(\frac{3}{2}, -\frac{1}{2} \rightarrow \frac{1}{2}, +\frac{1}{2})$	49 ± 10	9 ± 2.5	12 ± 3.5
$\sigma(\frac{3}{2}, -\frac{1}{2} \rightarrow \frac{1}{2}, -\frac{1}{2})$	39 ± 10	8 ± 2.5	11 ± 3
$\sigma(\frac{3}{2}, -\frac{1}{2} \rightarrow \frac{3}{2}, +\frac{1}{2})$	287 ± 80	129 ± 25	115 ± 30
$\sigma(\frac{3}{2}, -\frac{1}{2} \rightarrow \frac{3}{2}, +\frac{3}{2})$	341 ± 100	159 ± 30	-
$\sigma(\frac{3}{2}, -\frac{1}{2} \rightarrow \frac{3}{2}, -\frac{3}{2})$	492 ± 50	174 ± 35	-
$\sigma(\frac{1}{2}, +\frac{1}{2} \rightarrow \frac{1}{2}, -\frac{1}{2})$	129 ± 40	27 ± 8	34 ± 10
$\sigma(\frac{1}{2}, +\frac{1}{2} \rightarrow \frac{3}{2}, +\frac{1}{2})$	46 ± 15	7 ± 2	14 ± 4
$\sigma(\frac{1}{2}, +\frac{1}{2} \rightarrow \frac{3}{2}, +\frac{3}{2})$	51 ± 20	6 ± 1	14 ± 3
$\sigma(\frac{1}{2}, +\frac{1}{2} \rightarrow \frac{3}{2}, -\frac{3}{2})$	58 ± 20	8 ± 1.5	22 ± 6
$\sigma(\frac{1}{2}, +\frac{1}{2} \rightarrow \frac{3}{2}, -\frac{1}{2})$	51 ± 10	-	21 ± 5
$\sigma(\frac{1}{2}, -\frac{1}{2} \rightarrow \frac{1}{2}, +\frac{1}{2})$	83 ± 40	28 ± 8	35 ± 10
$\sigma(\frac{1}{2}, -\frac{1}{2} \rightarrow \frac{3}{2}, +\frac{1}{2})$	20 ± 6	9 ± 2.5	20 ± 5
$\sigma(\frac{1}{2}, -\frac{1}{2} \rightarrow \frac{3}{2}, +\frac{3}{2})$	23 ± 5	7 ± 1.5	16 ± 3
$\sigma(\frac{1}{2}, -\frac{1}{2} \rightarrow \frac{3}{2}, -\frac{3}{2})$	25 ± 5	7 ± 2	17 ± 3
$\sigma(\frac{1}{2}, -\frac{1}{2} \rightarrow \frac{3}{2}, -\frac{1}{2})$	25 ± 5	7 ± 1.5	17 ± 5

3.6 Observations

The most fundamental contribution of this work has been the measurement of the Zeeman energy transfer cross-sections for the 5^2P levels in rubidium with the rare gasses and nitrogen as collision partners. These cross-sections have not been previously reported. Additionally, this work has measured the spin-orbit energy transfer cross-section for CF_4 which also has not been previously measured. The spin-orbit energy transfer cross-sections for H_2 , D_2 , N_2 and CH_4 have also been reported.

The work performed measuring the spin-orbit energy transfer cross-sections employed a technique which allowed continuous measurement of the intensity ratio of the pump and satellite levels as a function of pressure. This is the first time a continuous measurement was made for rubidium.

The Zeeman energy transfer cross-section measurements allowed the examination of the validity of the established relationships between cross-sections. These relations are given in equations 61 and 62. These relations have not been tested previously in rubidium and this work has shown that these relations appear to be valid. An interesting feature is the unexpected variation in size of the cross-sections. With such a small energy spacing between the Zeeman split levels ($\ll kT$) expectations were that the cross-sections should be about the same size but, there is clearly a Δm_j dependence on the size of the cross-sections. Another interesting feature was the memory of the initial m_j level after a spin-orbit energy transfer, though this was a weak trend it was surprising to find any memory of the initial m_j level after an energy transfer with an energy gap $\Delta E \approx kT$.

The validation of the relationships given in equations 61 and 62 allows the comparison between the Zeeman energy transfer cross-sections directly measured and the cross-sections obtained using the disorientation and disalignment cross-sections. Table 27 provides a comparison of the cross-sections and Figure 54 displays the cross-sections versus the magnetic field. It appears from Figure 54 that there may

be a magnetic field dependence to the scaling of the cross-sections which causes an increase in the cross-section as the magnetic field is increased. The exception to this trend is the helium cross-section $\sigma(J = \frac{1}{2}, m_j = \frac{1}{2} \leftrightarrow J = \frac{1}{2}, m_j = -\frac{1}{2})$ which has the same value for both 0.11 and 2 Tesla magnetic field. This is consistent with the work done in reference (45) which reported no magnetic field dependence for this cross-section with a magnetic field strength of 1-7 Tesla.

Table 27. A comparison of the Zeeman energy transfer cross-sections by direct and indirect measurement. The cross-sections are reported using the notation $\sigma(J, m_j \leftrightarrow J', m_{j'})$ for the 5^2P levels in rubidium.

Gas	$\sigma (\text{\AA}^2)$ $\frac{1}{2}, \frac{1}{2} \leftrightarrow \frac{1}{2}, -\frac{1}{2}$	$\sigma (\text{\AA}^2)$ $\frac{3}{2}, \frac{1}{2} \leftrightarrow \frac{3}{2}, -\frac{1}{2}$	$\sigma (\text{\AA}^2)$ $\frac{3}{2}, \frac{1}{2} \leftrightarrow \frac{3}{2}, \frac{3}{2}$	$\sigma (\text{\AA}^2)$ $\frac{3}{2}, \frac{1}{2} \leftrightarrow \frac{3}{2}, -\frac{3}{2}$	Magnetic Field Tesla	Ref
He	16	34	64	75	2	This work
	16	29	41	37	0.11	(43)
	9				Earth	(30)
Ne	35	50	139	154	2	This work
	9.4	28	41	37	0.11	(43)
	6	12	28	22	Earth	(30)
Ar	24	57	150	131	2	This work
	16	56	83	74	0.11	(43)
	9.7	28	58	47	Earth	(30)
Kr	34	109	248	223	2	This work
	18	81	107	98	0.11	(43)
	10.6				Earth	(30)
Xe	39	115	224	243	2	This work
	24	91	129	117	0.11	(43)

The relaxation of the sublevels in an excited state of alkali atoms colliding with rare gases has been examined theoretically in reference (60). The model assumes a Van der Waals interaction between the atoms. Additional assumptions for this model are (1) a collision gives rise to a change in only the electron shell and the nucleus does not have time to change and (2) the transfer between the $^2P_{\frac{1}{2}}$ and $^2P_{\frac{3}{2}}$ levels can be neglected. This model predicts a scaling for the disorientation and disalignment cross-sections. This scaling has been mapped into a scaling for the Zeeman energy transfer cross-sections. Table 28 is a comparison of the ratios of the

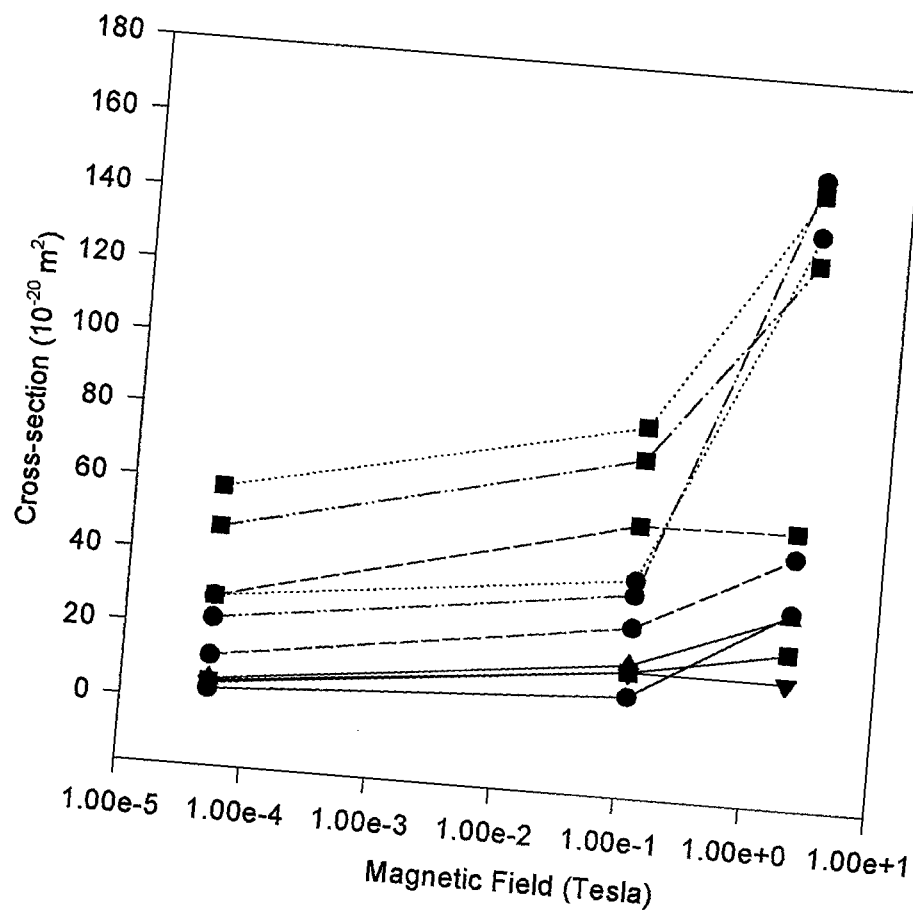


Figure 54. A comparison of the Zeeman cross-sections versus magnetic field with ∇ helium, \circ neon, \square argon, \triangle krypton, — $\sigma(J = \frac{1}{2}, m_j = \frac{1}{2} \leftrightarrow J = \frac{1}{2}, m_j = -\frac{1}{2})$, - - - $\sigma(J = \frac{3}{2}, m_j = \frac{1}{2} \leftrightarrow J = \frac{3}{2}, m_j = -\frac{1}{2})$, $\sigma(J = \frac{3}{2}, m_j = \frac{1}{2} \leftrightarrow J = \frac{3}{2}, m_j = \frac{3}{2})$, - · - · $\sigma(J = \frac{3}{2}, m_j = \frac{1}{2} \leftrightarrow J = \frac{3}{2}, m_j = -\frac{3}{2})$.

predicted scaling and the ratios of the cross-sections from the nitrogen data. The

Table 28. Theoretical scaling ratios compared with experimental values for nitrogen gas.

Cross-Section Ratio	Measured N_2	Theoretical Ref (60)
$\frac{\sigma(J=\frac{3}{2}, m_j=-\frac{1}{2} \leftrightarrow J=\frac{3}{2}, m_j=+\frac{3}{2})}{\sigma(J=\frac{3}{2}, m_j=+\frac{1}{2} \leftrightarrow J=\frac{3}{2}, m_j=+\frac{3}{2})}$	0.91	0.81
$\frac{\sigma(J=\frac{3}{2}, m_j=+\frac{1}{2} \leftrightarrow J=\frac{3}{2}, m_j=-\frac{1}{2})}{\sigma(J=\frac{3}{2}, m_j=+\frac{1}{2} \leftrightarrow J=\frac{3}{2}, m_j=+\frac{3}{2})}$	0.72	0.77
$\frac{\sigma(J=\frac{3}{2}, m_j=+\frac{3}{2} \leftrightarrow J=\frac{3}{2}, m_j=-\frac{3}{2})}{\sigma(J=\frac{3}{2}, m_j=+\frac{1}{2} \leftrightarrow J=\frac{3}{2}, m_j=+\frac{3}{2})}$	0.60	0.49

scaling in Table 28 seems to agree well with the theoretical results. The variation between the theoretical values and the values from the nitrogen data are possibly from the model assumption that there is no spin-orbit energy transfer occurring. Another possibility is the choice of the Van der Waals interaction potential may be in error.

For the case of nitrogen a comparison of the spin-orbit cross-sections measured directly and measured relative to Zeeman split levels is possible. The cross-section for the $5^2P_{\frac{3}{2}} \rightarrow 5^2P_{\frac{1}{2}}$ is $18.4 \pm 2.2 \text{ \AA}^2$ for the direct measurement and $14.3 \pm 2 \text{ \AA}^2$ for the Zeeman transfer measurements. The cross-section for the $5^2P_{\frac{1}{2}} \rightarrow 5^2P_{\frac{3}{2}}$ is $13.2 \pm 1.6 \text{ \AA}^2$ for the direct measurement and $10 \pm 1.4 \text{ \AA}^2$ for the Zeeman transfer measurement. There is good agreement between these cross-section measurements.

The noble gas spin-orbit cross-sections are much smaller than the spin-orbit cross-sections for the molecular gases. This would seem to imply that the spin-orbit cross-sections for the molecular gases seem to depend on an additional degree of freedom other than translation. An examination of the Zeeman cross-sections does not reveal this same trend. The Zeeman cross-sections do not exhibit a strong dependence on the additional degrees of freedom available in a molecular gas.

IV. Conclusion

This work has performed an extensive study of the collisional dynamics of the 5^2P levels in rubidium. The most fundamental contribution of this work has been the measurement of the Zeeman energy transfer cross-sections for the 5^2P levels in rubidium with the rare gasses and nitrogen as collision partners. This work has measured the spin-orbit energy transfer cross-section for CF_4 and this work has measured the pressure broadening and pressure line shift of rubidium with H_2 , D_2 and CF_4 as collision partners. This is the first measurement of the above stated cross-sections. Additionally this work has measured the spin-orbit energy transfer cross-sections for H_2 , D_2 , N_2 and CH_4 and, improved the accuracy of the pressure broadening and line shift cross-sections for the rare gases, N_2 , and CH_4 . The cross-sections measured for pressure broadening, spin-orbit energy transfer and Zeeman energy transfer are given in Table 29. Additionally, this table displays the rare gas spin-orbit energy transfer cross-sections measured by (31) and the quenching cross-sections for H_2 , D_2 , N_2 and CH_4 measured by (41).

The largest cross-sections appear to be the Zeeman energy transfer cross-sections. This is unexpected because a dephasing collision cross-section (pressure broadening) is expected to be smaller than a energy transfer cross-section. A possible explanation is that the Zeeman energy transfer cross-section and the pressure broadening cross-sections are very close to the same size. The apparent difference arises because the pressure broadening cross-sections are really an average across all levels where the Zeeman energy transfer cross-sections are for individual levels. Table 29 provides both the mean Zeeman energy transfer cross-sections and the pressure broadening cross-sections and these values compare very favorably.

The energy transfer cross-sections appear to scale inversely with the energy defect as is seen ranging from the largest (Zeeman) to the smallest (quenching) cross-sections. An exception to this trend is the Zeeman energy transfer cross-sections for

Table 29. Comparison of the cross-sections obtained from the pressure broadening, spin-orbit and Zeeman energy transfer experiments.

\bar{A}^2	D_1			
Collision Partner	Pressure Broadening	Zeeman $\pm \frac{1}{2}$	Spin-orbit	Quenching
He	52	16	0.072 ₍₃₁₎	
Ne	56	35	0.0014 ₍₃₁₎	
Ar	134	24	0.00051 ₍₃₁₎	
Kr	157	34	0.00036 ₍₃₁₎	
Xe	189	39	0.00034 ₍₃₁₎	
H_2	34		10.0	6 ₍₄₁₎
D_2	39		21.4	3 ₍₄₁₎
N_2	106	33	13.2	58 ₍₄₁₎
CH_4	151		29.5	< 1 ₍₄₁₎
CF_4	174		9.5	

\bar{A}^2	D_2				
Collision Partner	Pressure Broadening	Zeeman		Spin-orbit	Quenching
		Mean	$\pm \frac{1}{2}$		
He	55	58	34	0.105 ₍₃₁₎	
Ne	54	114	50	0.0022 ₍₃₁₎	
Ar	130	113	57	0.00073 ₍₃₁₎	
Kr	158	193	109	0.00045 ₍₃₁₎	
Xe	180	194	115	0.00049 ₍₃₁₎	
H_2	52			13.9	3 ₍₄₁₎
D_2	57			29.8	5 ₍₄₁₎
N_2	119	74	59	18.4	43 ₍₄₁₎
CH_4	136			41.0	3 ₍₄₁₎
CF_4	161			13.2	

the $5^2P_{\frac{1}{2}}$ manifold versus the $5^2P_{\frac{3}{2}}$ manifold. The energy gap between the levels is smaller for the $5^2P_{\frac{1}{2}}$ but the cross-sections are larger than those for the $5^2P_{\frac{3}{2}}$ manifold. This is partially resolved by only comparing the cross-sections for the $m_j = +\frac{1}{2} \leftrightarrow m_j = -\frac{1}{2}$ for the two manifolds. The size of the cross-sections are closer in value but the trend associated with the energy defect still does not hold.

The noble gas spin-orbit cross-sections are much smaller than the spin-orbit cross-sections for the molecular gases. This would seem to imply that the spin-orbit cross-sections for the molecular gases depend on an additional degree of freedom other than translation. An examination of the Zeeman and the pressure broadening cross-sections does not reveal this same trend. The Zeeman and pressure broadening cross-sections do not exhibit a strong dependence on the additional degrees of freedom available in a molecular gas.

The pressure broadening and pressure line shift work has resulted in a determination of the interaction potentials of rubidium with the selected gases. Also the pressure broadening data has revealed a dependence between the size of the pressure broadening cross-sections and the polarizability of the perturbing gas. Also a theory predicting the scaling of the Zeeman energy transfer cross-sections has been compared to the Zeeman energy transfer cross-sections using nitrogen gas. The favorable comparison indicates a Van der Waals potential interaction is a good model for the interaction. This is in agreement with the correlation of the pressure broadening data with the polarizability of the perturbing gas.

Additionally it appears that there may be a magnetic field dependence to the scaling of the Zeeman cross-sections which causes an increase in the cross-section as the magnetic field is increased. The exception to this trend is the helium cross-section $\sigma(J = \frac{1}{2}, m_j = \frac{1}{2} \leftrightarrow J = \frac{1}{2}, m_j = -\frac{1}{2})$.

Bibliography

1. C. S. Adams and A. I. Ferguson. "Saturated Spectroscopy and Two-Photon Absorption Spectroscopy in Rubidium Using an Actively Stabilized $Ti : Al_2O_3$ Ring Laser," *Optics Communications*, 75:419-424 (March 1990).
2. Nicole Allard and John Kielkopf. "The effect of neutral nonresonant collisions on atomic spectral lines," *Review of Modern Physics*, 54:1103-1182 (October 1982).
3. Herbert L. Anderson. *A Physicist's Desk Reference*. New York: American Institute of Physics, 1989.
4. Maurice Arditi and Pierre Cerez. "Hyperfine Structure Separation of the Ground State of $87Rb$ Measured With an Optically Pumped Atomic Beam," *IEEE Transactions on Instrumentation and Measurement*, IM-21:391-395 (November 1972).
5. E. Arimondo, M. Inguscio, and P. Violino. "Experimental determinations of the Hyperfine Structure in the Alkali Atoms," *Review of Modern Physics*, 49:31-75 (January 1977).
6. E. Arimondo and M. Krainsha-Miszczak. "Hyperfine Constants in the $5P_{3/2}$ State of $85Rb$," *Journal of Physics B-Atomic Molecular and Atomic Physics*, 8:1613-1616 (1975).
7. G. P. Barwood, P. Gill, and W. R. C. Rowley. "Rb Saturation Spectroscopy with an Optically Narrowed FM Diode Laser," *Optics Communications*, 80:359-364 (January 1991).
8. W. E. Baylis *Journal of Chemical Physics*, 51:2665 (1969).
9. W. E. Baylis, W. Hanle, and H. Kleinpoppen. *Progress in Atomic Spectroscopy B*. New York and London: Plenum Press, 1978.
10. James R. Beacham and Kenneth L. Andrew. "Optical Study of the Hyperfine Structure of the Rubidium Resonance Lines," *Journal of the Optical Society of America*, 61:231-235 (February 1971).
11. T. J. Beahn, W. J. Condell, and H. I. Mandelberg. "Excitation-Transfer Collisions Between Rubidium and Helium Atoms," *Physical Review*, 141:83-87 (January 1966).
12. J. A. Bellisio, P. Davidovits, and P. J. Kindlmann. "Quenching of Rubidium Resonance Radiation by Nitrogen and the Noble Gases*," *Journal of Chemical Physics*, 48:2376-2377 (1968).
13. V. N. Belov. "Application of the magnetic-scanning method to the measurement of the broadening and shift constants of the rubidium D_2 line (780.0 nm) by foreign gases," *Opt. Spektrosk*, 51:43-47 (July 1981).

14. V. N. Belov. "Measurement of the constants for the broadening and shift of the D_2 line of rubidium (780.0 nm) by inert gases," *Opt. Spektrosk*, 51:379-381 (August 1981).
15. R. W. Berends, W. Kedzierski, W. E. Baylis, and L. Krause. "Determination of Cross Sections for Collisionally Induced Multipole Relaxation in Alkali-Metal Atoms from Zeeman Fluorescence Intensities," *Physical Review A*, 39:1526-1529 (February 1989).
16. R. W. Berends, W. Kedzierski, and L. Krause. "Multipole Relaxation in 5^2P Potassium Atoms by Collision with He, Ne, and Ar," *Physical Review A*, 37:68-76 (January 1988).
17. R. W. Berends, P. Skalinski, and L. Krause. "Multipole relaxation in 4^2P potassium atoms by collisions with N_2 and H_2 ," *Journal of Physics B-Atomic Molecular and Atomic Physics*, 17:605-614 (1984).
18. R. Boggy and F. A. Franz. "Cross sections for $J, m_J \rightarrow J', m_{J'}$ transitions within the 4^2P states of potassium induced by collisions with He, Ne, and Kr," *Physical Review A*, 25:1887-1899 (April 1982).
19. C. Brechignac, S. Gerstenkorn, and P. Luc. "Déplacement isotopique dans la raie de résonance D_2 du rubidium inversion des valeurs de $|f^2|$ des isotopes ^{85}Rb et ^{87}Rb ," *Physica*, 82:409-417 (1976).
20. B. Brouillaud and R. Gayet. "Depolarisation of the $5p^2P_{1/2}$ state of rubidium induced by collisions with helium or xenon," *Journal of Physics B-Atomic Molecular and Atomic Physics*, 10:2143-2155 (1977).
21. H. Bucka. "Zum Kernquadrupolmoment von Rb^{87} ," *Zeitschrift für Physik*, 176:45-46 (1963).
22. B. R. Bulos, A. Marshall, and W. Happer. "Light Shifts Due to Real Transitions in Optically Pumped Alkali Atoms," *Physical Review A*, 4:51-59 (July 1971).
23. H. B. G. Casimir. *On the Interaction Between Atomic Nuclei and Electrons*. San Francisco and London: W. H. Freeman and Company, 1963.
24. Ron Catterall and Peter P. Edwards. "Observation of the Rubidium-85, -87 Solid-State Hyperfine Structure Anomaly by Electron Spin Resonance Spectroscopy," *Canadian Journal of Physics*, 32:555-567 (1976).
25. J. Cuvellier, J. M. Mestdagh, M. Ferray, and P. de Pujo. "Influence of the Rotational Energy of the Molecular Perturber on the $\text{Rb}(5P)-H_2, D_2$ Fine Structure Changing Collisions," *Journal of Chemical Physics*, 79:2848-2853 (September 1983).
26. Wolfgang Demtroder. *Laser Spectroscopy Basic Concepts and Instrumentation*. Berlin Heidelberg New York: Springer-Verlag, 1982.
27. T. H. Duong, R. Marrus, and J. Yellin. "Atomic Beam Study of the Rubidium 85, 87 Relative Isotope Shift," *Physics Letters B*, 27:565-566 (September 1968).

28. J. Farley, P. Tsekeris, and R. Gupta. "Hyperfine-Structure Measurements in the Rydberg S and P States of Rubidium and Cesium*," *Physical Review A*, 15:1530-1536 (April 1977).
29. D. Feiertag and G. zu Putlitz. "Hyperfine Structure, g_J Factors and Lifetimes of Excited $^2P_{\frac{1}{2}}$ States of Rb," *Zeitschrift fur Physik*, 261:1-12 (1973).
30. Alan Gallagher. "Collisional Depolarization of the Rb 5P and Cs 6P Doublets," *Physical Review*, 157:68-72 (May 1967).
31. Alan Gallagher. "Rubidium and Cesium Excitation Transfer in Nearly Adiabatic Collisions with Inert Gases*," *Physical Review*, 172:88-96 (1968).
32. Hyatt M. Gibbs and George. C. Churchill. "Laser Spectroscopic Measurement of the ^{87}Rb - ^{85}Rb D_1 -Line Isotope Shift," *Journal of the Optical Society of America*, 62:1130 (1972).
33. M. Glodz and M. Krainska-Miszczak. "Hyperfine Interaction Constants of the 10, 11 and 12 $^2D_{\frac{3}{2}}$ States in ^{87}Rb Measured by the Quantum Beat Method," *Physics Letters A*, 160:85-89 (November 1991).
34. E. P. Gordeyev, E. E. Nikitin, and M. Ya. Ovchinnikova. "Calculation of cross sections for the depolarization of 2P states in alkali atoms," *Canadian Journal of Physics*, 47:1819-1827 (1969).
35. S. Goudsmit and R. F. Bacher. "The Paschen-Back Effect of Hyperfine Structure," *Physical Review*, 34:1499-1500 (1929).
36. R. Granier, J. Granier, and F. Schuller. "Calculations of Impact Broadening and Shift of Spectral Lines for Realistic Interatomic Potentials," *Journal of Quantum Spectroscopic Radiation Transfer*, 16:143-146 (1976).
37. S. Haslam and E. L. Lewis. "Collisional Exchange or Excitation Between Alkali-Metal Atoms," *Journal of Physics B-Atomic Molecular and Atomic Physics*, 22:L469-L473 (1989).
38. A. P. Hickman. "Model for Fine-Structure Transitions in Collisions of $\text{K}(4^2P)$ and $\text{Rb}(5^2P)$ with H_2 and N_2 ," *Journal of Physics B-Atomic Molecular and Atomic Physics*, 14:1009-1018 (1981).
39. W. R. Hindmarsh, A. D. Petford, and G. Smith. "Interpretation of collision broadening and shift in atomic spectra," *Proc. Roy. Soc.*, A297:296-304 (1967).
40. Joseph O. Hirschfelder, Charles F. Curtiss, and R. Byron Bird. *Molecular Theory of Gases and Liquids*. New York: John Wiley and Sons, Inc., 1954.
41. E. S. Hrycyshyn and L. Krause. "Inelastic Collisions Between Excited Alkali Atoms and Molecules. VII. Sensitized Fluorescence and Quenching in Mixtures of Rubidium with H_2 , HD, D_2 , N_2 , CH_4 , CD_4 , C_2H_4 , and C_2H_6 ," *Canadian Journal of Physics*, 48:2761-2768 (1970).

42. S. L. Izotova, A. I. Kantserov, and M. S. Frish. "Constants for broadening and shift of D_1 and D_2 rubidium 87 lines by inert gases," *Opt. Spektrosk*, 51:196-199 (July 1981).
43. B. Kamke. "Disorientation and Disalignment Cross Sections of Excited Rb-Atoms Colliding with Noble Gases," *Zeitschrift fur Physik*, 273:23-28 (1975).
44. S. A. Kazantsev, N. I. Kaliteevskii, and O. M. Rish. "Application of the magnetic scanning technique for measuring the broadening and shift of the D_1 resonance line of rubidium caused by inert gases," *Opt. Spektrosk*, 44:638-643 (April 1978).
45. W. Kedzierski, Ju Gao, W. E. Baylis, and L. Krause. "Magnetic-field dependence of the cross section for m_j mixing in $^2P_{1/2}$ Cs and Rb atoms," *Physical Review A*, 49:4540-4548 (June 1994).
46. W. Kedzierski, R. B. Middleton, and L. Krause. " m_j Mixing and Multipole Relaxation in 6^2P Rubidium Atoms Induced by He, Ne, and Ar Collisions," *Physical Review A*, 43:143-146 (January 1991).
47. Seung-Sub Kim, Sang-Eon Park, Ho-Seong Lee, Cha-Hwan Oh, Jong-Sad Park, and Hyuck Cho. "High-Resolution Spectroscopy of Rubidium Atoms," *Jpn. Journal of Applied Physics*, 32:3291-3295 (1993).
48. Hans Kopfermann. *Nuclear Moments*. New York: Academic Press INC., 1958.
49. L. Krause. "Collisional Excitation Transfer Between the $^2P_{1/2}$ and $^2P_{3/2}$ Levels in Alkali Atoms," *Applied Optics*, 5:1375-1382 (September 1966).
50. V. S. Lebedev. "Inelastic Transitions Between the Fine-Structure Components of Rydberg Atoms in Collisions with Neutral Particles," *Journal of Physics B-Atomic Molecular and Atomic Physics*, 25:L131-L136 (March 1992).
51. Raphael D. Levine and Richard B. Bernstein. *Molecular Reaction Dynamics and Chemical Reactivity*. New York Oxford: Oxford University Press, 1987.
52. P. L. Lijnse, P. J. Th. Zeegers, and C. Th. J. Alkemade. "Cross Sections for Quenching and Doublet Mixing of $Rb(5^2P_{3/2, 1/2})$ Doublet by N_2 , O_2 , H_2 and H_2O ," *Journal of Quantum Spectroscopic Radiation Transfer*, 13:1033-1045 (1973).
53. John K. Link. "Measurement of the Radiative Lifetimes of the First Excited States of Na, K, Rb, and Cs by Means of the Phase-Shift Method," *Journal of the Optical Society of America*, 56:1195-1199 (September 1966).
54. T. R. Mallory, W. Kedziersky, J. B. Atkinson, and L. Krause. " 9^2D Fine-Structure Mixing in Rubidium by Collisions with Ground-State Rb and Noble-Gas Atoms," *Physical Review A*, 38:5917-5921 (December 1988).
55. J. M. Mestdagh, P. de Pujo, J. Cuvellier, A. Binet, P. R. Fournier, and J. Berlande. "Fine-Structure Transitions in $Rb(5P)$ induced by H_2 and

- N_2 Molecules," *Journal of Physics B-Atomic Molecular and Atomic Physics*, 15:663-673 (1982).
56. P. Munster and J. Marek. "Determination of Cross Sections of Excitation Transfer Between the Fine-Structure Components of $Cs(7^2P)$, $Rb(6^2P)$ and $Rb(7^2P)$ Induced by Collisions with Rare-Gas Atoms," *Journal of Physics B-Atomic Molecular and Atomic Physics*, 14:1009-1018 (1981).
 57. S. Nakayama. "Polarization Spectroscopy of Rb and Cs," *Optics Communications*, 50:19-25 (May 1984).
 58. E. E. Nikitin. "Nonadiabatic Transitions between Fine-Structure Components of Alkali Atoms upon Collision with Inert-Gas Atoms," *Journal of Chemical Physics*, 43:744-750 (July 1965).
 59. E. E. Nikitin. "Theory of Nonadiabatic Collision Processes Including Excited Alkali Atoms," *Advances in Chemical Physics*, 28:317-377 (1975).
 60. A. I. Okunevich and V. I. Perel. "Relaxation in the sublevel system of the excited state of alkali metal atoms colliding with noble gas atoms," *Soviet Physics JETP*, 31:356-361 (August 1970).
 61. Ronald E. Olson. "Fine Structure Transition Cross Sections for Several Alkali + Rare Gas Systems," *Chemical Physics Letters*, 33:250-253 (June 1975).
 62. Ch. Ottinger, Richard Scheps, G. W. York, and Alan Gallagher. "Broadening of the Rb resonance lines by noble gases," *Physical Review A*, 11:1815-1828 (June 1975).
 63. J. W. Parker, H. A. Schuessler, Jr. R. H. Hill, and B. J. Zollars. "Fine-Structure-Changing Collision Cross Section Within the Low-Lying n^2D States of Rubidium induced by Ground-State Rubidium Atoms," *Physical Review A*, 29:617-624 (February 1984).
 64. J. Pascale and R. E. Olson. "Total Cross Sections for $Na(3^2P_{\frac{1}{2}} \rightarrow 3^2P_{\frac{3}{2}}) +$ Rare Gas Collisions," *Journal of Chemical Physics*, 64:3538-3543 (May 1976).
 65. J. Pascale, F. Rossi, and W. E. Baylis. "Quantum-Mechanical Study of Nonre-active Collisions Between $Rb(5^P)$ and H_2 or D_2 ($1\Sigma_g^+$, $v = 0$)," *Physical Review A*, 36:4219-4235 (November 1987).
 66. R. A. Phaneuf and L. Krause. " $5^2P_{\frac{1}{2}} \leftrightarrow 5^2P_{\frac{3}{2}}$ Excitation Transfer in Rubidium Induced in Collisions with CH_4 , CH_4D_2 , and CD_4 Molecules," *Canadian Journal of Physics*, 58:1047-1048 (1980).
 67. V. N. Rebane. "Calculation of the broadening and shift of hyperfine components of rubidium and cesium D_1 lines in collisions with atoms of heavy inert gases," *Opt. Spektrosk*, 41:894-896 (November 1976).
 68. V. N. Rebane. "Calculation of the broadening and shift of hyperfine components of rubidium and cesium D_2 lines in collisions with atoms of heavy inert gases," *Opt. Spektrosk*, 44:644-650 (April 1978).

69. R. H. G. Reid. "Transitions Among the $3p^2P$ States of Sodium Induced by Collisions with Helium," *Journal of Physics B-Atomic Molecular and Atomic Physics*, 6:2018-2039 (October 1973).
70. J. H. Sanders and S. Stenholm. *Progress in Quantum Electronics*. New York: Pergamon Press, 1973.
71. Craig J. Sansonetti and K. H. Webber. "High-Precision Measurements of Doppler-Free Two-Photon Transition in Rb: new values for Proposed Dye-Laser Reference Wavelengths," *Journal of the Optical Society of America B*, 2:1385-1391 (September 1985).
72. H. A. Schussler. "Prazisionsmessung der Hyperfeinstruktur des $5^2P_{\frac{3}{2}}$ -Terms und des $6^2P_{\frac{3}{2}}$ -Terms von Rb^{85} und Rb^{87} ," *Zeitschrift fur Physik*, 182:289-305 (1965).
73. B. Senitzky and I. I. Rabi. "Hyperfine Structure of $Rb^{85,87}$ in the 5P State," *Physical Review*, 103:315-321 (July 1956).
74. A. Sieradzan and F. A. Franz. "Quenching, depolarization, and transfer of spin polarization in Rb- N_2 collisions," *Physical Review A*, 25:2985-2995 (June 1982).
75. P. Skalinski and L. Krause. "Collisional m_j mixing and multipole relaxation in 4^2P potassium atoms," *Physical Review A*, 26:3338-3345 (December 1982).
76. David C. Thompson and Gen-Xing Xu. "Optical Measurements of Vapor Pressures of Rb and a Rb-K Mixture," *Canadian Journal of Physics*, 60:1496-1501 (1982).
77. C. Vadla, S. Knezovic, and M. Movre. "Rubidium 5^2P Fine-Structure Transition Induced by Collisions with Potassium and Cesium Atoms," *Journal of Physics B-Atomic Molecular and Atomic Physics*, 25:1337-1345 (March 1992).
78. Mina Vajed-Samii, S. N. Ray, and T. P. Das. "Relativistic Treatment of One and Many-Electron Contributions to Hyperfine Interactions in Excited S States of Rubidium Atoms," *Physical Review A*, 24:1204-1214 (September 1981).
79. W. A. van Wijngaarden and J. Sagle. "Magnetic-Field Decoupling of an Alkali-Metal Excited-State Hyperfine Structure," *Physical Review A*, 43:2171-2178 (March 1991).
80. J. Vanier, R. Kunski, N. Cyr, J. Y. Savard, and M. Tetu. "On Hyperfine Frequency Shifts Caused by Buffer Gases: Application to the Optically Pumped Passive Rubidium Frequency Standard," *Journal of Applied Physics*, 53:5387-5391 (August 1982).
81. Jacques Vanier and Claude Audoin. *The Quantum Physics of Atomic Frequency Standards*. Great Britain: Adam Hilger, Bristol and Philadelphia, 1989.
82. Joseph T. Verdeyen. *Laser Electronics second edition*. New Jersey: Prentice-Hall, Inc., 1981.

83. C. W. White, W. M. Hughes, G. S. Hayne, and H. G. Robinson. "Determination of g-Factor Ratios for Free ^{133}Cs and ^{87}Rb Atoms," *Physical Review A*, 7:1178-1182 (March 1973).
84. Harvey Elliott White. *Introduction to Atomic Spectra*. New York: McGraw-Hill Book Company, Inc., 1934.

Vita

My name is Matthew Don Rotondaro. [REDACTED]

[REDACTED] I grew up in a small town in California named Los Banos, with a population of only 10031. I attended my first two years of college at Merced Junior College, in Merced, Ca., where I received an Associate of Science degree in Engineering. I continued my education at the University of California at Davis, Davis, Ca., where I received a Bachelors of Science in Physics. Upon graduation I enlisted in the United States Air Force and received my commission through the Officers Training School. I moved from there to Chanute AFB, Rantoul, Il, for training as an aircraft maintenance officer. Upon completion of training, I was assigned to the Organizational Maintenance Squadron at Carswell AFB, FortWorth, Tx. The completion of that assignment found me assigned to the Air Force Institute of Technology where I received a Masters Degree in Physics. From there I was assigned to the Avionics Directorate also at Wright Patterson AFB. where I worked for a year and a half before being invited back to AFIT to work on a PhD. in physics. — Future —.

[REDACTED]
Permanent Address [REDACTED]
[REDACTED]

REPORT DOCUMENTATION PAGE			Form Approved OMB No. 0704-0188	
Public reporting burden for this collection of information is estimated to average 1 hour per response, including the time for reviewing instructions, searching existing data sources, gathering and maintaining the data needed, and completing and reviewing the collection of information. Send comments regarding this burden estimate or any other aspect of this collection of information, including suggestions for reducing this burden, to Washington Headquarters Services, Directorate for Information Operations and Reports, 1215 Jefferson Davis Highway, Suite 1204, Arlington, VA 22202-4302, and to the Office of Management and Budget, Paperwork Reduction Project (0704-0188), Washington, DC 20503.				
1. AGENCY USE ONLY (Leave blank)		2. REPORT DATE August 1995		3. REPORT TYPE AND DATES COVERED Doctoral Dissertation
4. TITLE AND SUBTITLE Collisional Dynamics of the Rubidium 5^2P Levels			5. FUNDING NUMBERS	
6. AUTHOR(S) Matthew D. Rotondaro, Captain, USAF				
7. PERFORMING ORGANIZATION NAME(S) AND ADDRESS(ES) Air Force Institute of Technology WPAFB, OH 45433-6583			8. PERFORMING ORGANIZATION REPORT NUMBER AFIT/DS/ENP/95-02	
9. SPONSORING/MONITORING AGENCY NAME(S) AND ADDRESS(ES) AFOSR/NC Bolling AFB Washington DC. 20332-6448 ATTN: Dr. Michael Berman			10. SPONSORING/MONITORING AGENCY REPORT NUMBER	
11. SUPPLEMENTARY NOTES				
12a. DISTRIBUTION / AVAILABILITY STATEMENT Approved for public release; distribution unlimited			12b. DISTRIBUTION CODE	
13. ABSTRACT (Maximum 200 words) The collisional dynamics of the 5^2P levels in rubidium has been examined using steady-state laser absorption and spectrally-resolved laser induced fluorescence techniques. State-to-state cross-sections for energy transfer between Zeeman split levels ranged from 16-248 \AA^2 for collisions with nitrogen and rare gases. These energy transfer cross-sections exhibit a significant dependence on (J, m_J) state and certain symmetry relationships are demonstrated. A sub-Doppler spectrum of the Zeeman split levels indicating the isotopic shift in the D_1 line of 106 ± 35 was obtained using laser saturation spectroscopy. Cross-sections for spin orbit energy transfer between the $5^2P_{1/2}$ and $5^2P_{3/2}$ levels for collisions with H_2 ($\sigma_{P_{1/2} \rightarrow P_{3/2}} = 10.0 \text{ \AA}^2$, $\sigma_{P_{3/2} \rightarrow P_{1/2}} = 13.9 \text{ \AA}^2$), $D_2(21.4, 29.8)$, $N_2(13.2, 18.4)$, $CH_4(29.5, 41.0)$ and $CF_4(9.5, 13.2)$ have been measured. Finally, the pressure broadening and pressure induced line shifts for Rb $5^2P_{1/2} - 5^2S_{1/2}$ and $5^2P_{3/2} - 5^2S_{1/2}$ transitions at low buffer gas pressure were obtained from high resolution laser absorption spectra. The shifts β and broadening γ for H_2 , D_2 , N_2 , CH_4 and CF_4 are in MHz per Torr $\beta(5^2P_{1/2}) = -2.17, -2.22, -7.41, -7.92, -5.41$; $\beta(5^2P_{3/2}) = -3.83, -4.09, -5.79, -7.0, -5.73$; $\gamma(5^2P_{1/2}) = 17.3, 14.1, 16.3, 29.1, 18.7$; $\gamma(5^2P_{3/2}) = 26.4, 20.6, 18.3, 26.2, 17.3$ respectively. These values have been further interpreted using the impact approximation for collisional broadening to obtain the parameters for the Leonard Jones interaction potentials. The rates for pressure broadening are clearly correlated with polarizability of the collision partner.				
14. SUBJECT TERMS Rubidium, Zeeman, Pressure broadening			15. NUMBER OF PAGES 132	
			16. PRICE CODE	
17. SECURITY CLASSIFICATION OF REPORT Unclassified	18. SECURITY CLASSIFICATION OF THIS PAGE Unclassified	19. SECURITY CLASSIFICATION OF ABSTRACT Unclassified	20. LIMITATION OF ABSTRACT UL	